

**NASA**  
**Reference**  
**Publication**  
**1226**

1989

## MARA System Documentation

*Volume I—MARA System  
Requirements Document*

C. L. Parsons, *Editor*  
*Goddard Space Flight Center*  
*Wallops Flight Facility*  
*Wallops Island, Virginia*

**NASA**

National Aeronautics and  
Space Administration  
Office of Management  
Scientific and Technical  
Information Division

# TABLE OF CONTENTS

1.0	INTRODUCTION	1
1.1	<u>Purpose of Documentation</u>	1
1.2	<u>MARA Instrument System Background</u>	2
1.3	<u>Documentation Format</u>	3
2.0	SCIENCE REQUIREMENTS FOR TOPOGRAPHIC MEASUREMENTS	3
2.1	<u>The Oceans</u>	3
2.2	<u>The Land</u>	7
2.3	<u>The Ice Sheets</u>	12
3.0	MARA DEVELOPMENT GOALS	12
3.1	<u>General</u>	12
3.2	<u>The Oceans</u>	14
3.3	<u>The Land</u>	15
3.4	<u>The Ice Sheets</u>	17
4.0	MARA INSTRUMENT DESIGN PARAMETER STUDIES	18
4.1	<u>Design Goal Priorities</u>	18
4.2	<u>Beam-limited Altimetry</u>	18
	4.2.1 Antenna Design	18
	4.2.2 Modes of Operation	20
4.3	<u>Frequency</u>	24
4.4	<u>Mean Waveform Shape</u>	25
	4.4.1 General	25
	4.4.2 Simulations	25
	4.4.3 Analytical Models	32
4.5	<u>The Noisy Waveform</u>	37
4.6	<u>Pulse-Repetition-Frequency</u>	45
4.7	<u>Tracking Precision</u>	46
4.8	<u>Signal-to-Noise Calculations</u>	51
4.9	<u>Coherent Processing</u>	60
5.0	MARA DESIGN CHARACTERISTICS	60
6.0	REFERENCES	61
	APPENDIX A	65
	APPENDIX B	67

PRECEDING PAGE BLANK NOT FILMED

~~SECRET~~ INTENTIONALLY BLANK

## 1.0 INTRODUCTION

### 1.1 Purpose of Documentation

The Multimode Airborne Radar Altimeter (MARA) is a sophisticated, yet flexible research instrument system developed by NASA's Goddard Space Flight Center. It has been developed through the Ocean Advanced Studies RTOP (UPN 161-10-06) administered and funded by the Oceanic Processes Branch at NASA Headquarters. This volume is the first of four documents that describe the MARA system. Each has a specific objective. In Volume I, the scientific justification for the development of the radar system is presented. This is followed by a translation of these geophysical measurement requirements into concrete instrument science measurement goals. Volume II describes the actual design of the MARA to the component level and shows that the design meets the instrument science measurement goals from Volume I. The third volume discusses the performance verification of the MARA. Laboratory and experimental test flights of the instrument on the Wallops Flight Facility (WFF) P-3 research aircraft are described and results shown that prove the instrument science measurement goals are met. Geophysical experimental aircraft missions are described that verify that the earth science measurement requirements can be met with this system. The final document, Volume IV, contains component specifications, circuit diagrams, and other reference materials that may prove useful for the maintenance and operation of the MARA system.

The complete four volume documentation for the Multimode Airborne Radar Altimeter therefore consists of:

- Vol. I. MARA System Requirements Document
- Vol. II. MARA System Implementation Document
- Vol. III. MARA System Performance Document
- Vol. IV. MARA System Component/Parts Document

These reference documents are written by the MARA Instrument Team, which is identified below:

- C. L. Parsons, Principal Investigator, NASA WFF, Code 672
- S. Bailey, NASA WFF, Code 672
- D. E. Hines, NASA WFF, Code 672
- C. R. Piazza, NASA WFF, Code 672
- A. Selser, NASA WFF, Code 822.2
- D. W. Shirk, NASA WFF, Code 672
- E. J. Walsh, NASA WFF, Code 672
- C. W. Wright, NASA WFF, Code 672
- D. C. Young, NASA WFF, Code 831.1
- G. Norcross, Computer Sciences Corporation
- J. Ward, Computer Sciences Corporation

Additionally, this development has greatly benefited from the contributions of Dr. Lee Miller of Applied Science Associates, Inc., Central, South Carolina 29630, and Clemson University. He has been supported by Contract No. NAS5-28926 and by Research Grant No. NAG5-651. Also, much of the analytical support for MARA has resulted from the work of Dr. Gary Brown of the Virginia Polytechnic Institute and State University. His support has come from NASA Research Grant Nos. NAG5-636 and NAG5-648. The contributions of the various team members are not

identified in the MARA System Documents. Instead, these volumes are the joint product of the MARA Instrument Team. For the particular case of Volume I, the contributions of E. J. Walsh for sections 4.2.2, 4.4.2, and 4.7 must be cited. Editing of the material in these volumes has been performed by the Principal Investigator.

## 1.2 MARA Instrument System Background

The Multimode Airborne Radar Altimeter (MARA) culminates a concerted effort over several years to advance the science of radar altimetry. One of the goals of NASA's Ocean Advanced Studies RTOP (UPN 161-10-06) has been to identify new and potentially useful technologies for the further development of satellite altimetric remote sensing. The recommendations have been documented in long range planning publications (Advanced Ocean Sensor Long Range Plan, McGoogan *et al*, April 1982, Wallops Internal Publication WFC-971.0-82-004) which have been updated periodically. Several of the recommendations have been implemented through The Ocean Topography Experiment (TOPEX), a satellite radar altimeter mission scheduled for launch in 1991. That radar will use two channels to enable a correction for the variable delays in propagation due to the ionosphere. For one of the channels a solid-state transmitter will be used as recommended in the Long Range Plan. Most of the other technological advancements recommended involve advanced beam patterns, which of course require observation geometries in off-nadir directions. Various innovative concepts such as the use of a forward-looking beam and adaptive trackers, the push-broom pattern to produce instantaneous wide swath "pictures" of the earth's topography, and the use of new frequencies of operation are examples of Long Range Plan recommendations that have not been tested and evaluated. They must be implemented in a benign environment before their use in space can be proposed. Consequently, a proposal was submitted to the Oceanic Processes Branch of NASA Headquarters in 1985. Entitled "Technology Studies in Support of an Earth Observing Radar," it described a three-year development of an airborne radar system that would have the flexibility and capability to study the innovations recommended in the Long Range Plan plus new and exciting ideas in the future. The proposal was approved effective January 15, 1986. The Multimode Airborne Radar Altimeter is the product of this proposal.

During the development, the commonality of subsystems and components between the original MARA design and the Surface Contour Radar (SCR) was noted. The SCR is a scanning, bistatic airborne radar designed to measure the directional wave spectra of the ocean surface. Sponsored by the NASA Advanced Applications Flight Experiments Program (AAFE), this system was first made operational in 1979 (Kenney and Walsh, 1979). It has supported many oceanographic wave experiments and has been proven to be a reliable and useful measurement tool. The age of many of its components and the antiquated technology used in its development now add risk to its continued use. Studies concluded that the SCR could be incorporated as one mode of operation in the new MARA system. Thus, improvements could be made in the SCR design, new technology could be used to enhance the SCR's performance, and this could be accomplished cost effectively by sharing subsystems with the MARA radar system. Consequently, the MARA is a multiple mode system. Its various modes of operation are described in more detail in section 4.2.2 of this volume. The planned modes include an interferometric antenna system to evaluate that concept, which has been proposed for use with the Land and Ocean Radar Altimeter (LORA), an instrument system proposed for the Earth Observing System (EOS).

The impetus for the advanced beam configuration altimetry, the SCR configuration of the MARA, and the interferometric mode is from the oceanography community. The funding for the MARA system development has been provided by the Headquarters Oceanic Processes Branch. However,

the MARA system has potential applications for land processes and ice sheet mapping projects as well. This was recognized early in the development process and the system design includes the capability to make land and ice topographic measurements of interest to the scientific community.

### 1.3 Documentation Format

In this volume, section 2.0 summarizes the science community's requirements for topographic measurements of the oceans, the land, and the earth's ice surfaces. In the next section, these requirements are translated into instrumentation science goals for the MARA. Some of the science requirements can be translated into geophysical measurement goals for the airborne system; others cannot be measured from the aircraft's altitudes. For these latter cases, technological tests can be conducted using the MARA to demonstrate that conceptual designs for future spacecraft radars are valid and that these future radar systems will be able to produce the needed scientific geophysical measurements.

Section 4.0 contains the results of various studies conducted to define the operating characteristics of the MARA system. The antenna system selected for use is described in 4.2.1. The system modes of operation are discussed in 4.2.2. Sections 4.3 through 4.6 treat the choice of frequency of operation, the expected off-nadir waveform shape and the effect of pulsewidth and noise on that shape, and pulse repetition frequency and its effect on pulse-to-pulse correlation. Section 4.7 gives an assessment of the expected system's tracking performance with and without waveform averaging. Finally, section 4.8 contains signal-to-noise calculations for the various modes of operation of the system.

The last two sections of the volume summarize the MARA operating characteristics and present pertinent references that complement the contents of this volume.

## 2.0 SCIENCE REQUIREMENTS FOR TOPOGRAPHIC MEASUREMENTS

### 2.1 The Oceans

The oceans cover some 70% of the globe. Their importance to man's habitation of the planet can not be overemphasized. In the introduction of "Satellite Altimetric Measurements of the Ocean," the 1981 report of the TOPEX Science Working Group, the following justification for a global ocean monitoring system was given:

"The movement of water in the ocean has an impact upon human life in a variety of ways. On the Earth, climatic contrasts between pole and equator are greatly ameliorated by the presence of the ocean because of its large heat capacity and its contribution to the movement of heat from equator to poles. Much of the weather we experience is spawned over the ocean through complex air-sea transfer processes. The important global fishing grounds are limited to small geographical areas dominated by special oceanic flows, and the movement of chemical tracers and pollutants in the sea is of present and future importance. For example, the rate at which the burning of fossil fuel causes the temperature of the air to rise is determined to a large extent by the rate at which the ocean will be able to absorb the CO<sub>2</sub> and by the rate at which the ocean warms due to increased atmospheric heating...

Many things about the ocean are poorly understood, largely because the ocean is so difficult to observe. It is a global fluid, and like the atmosphere it appears to have both a climate and a weather. But unlike meteorologists, oceanographers have no global observation system, only fragmentary and ephemeral regional observation systems...

The past decade has shown oceanographers that to understand fully the workings of the global ocean, and thus to understand fully its impact on both the problems stated above and others (fisheries, climate, weather, and defense) we require an observation system analogous to that available to meteorologists..."

In a recent report, Walter Munk (1978) stated that

"We may think of the mesoscale fluctuations as the weather in the sea. The 100-kilometer ocean correlation scale compares to 1,000 kilometers in the atmosphere, and the two-month ocean time scale to four days in the atmosphere. Space resolution is very hard to come by, and so the oceanographer is faced with a tougher job than the meteorologist. If we give up on monitoring and charting mesoscale eddies, it is as if the meteorologists had given up on storms and confined themselves to problems of climate. A pilot coming into London Airport would not find it very useful if he were furnished only with the mean September winds. In just the same way a submarine sonar officer does not find season charts very useful, and he has learned to depend instead on his own local observations. A similar situation may hold for deep-sea fishermen. The suggestion is that the past lack of success in describing and predicting biological distributions, air-sea interactions, anti-submarine warfare conditions, etc., is the result of not having taken into account this dominant mesoscale variability..."

Could the technical means be developed for monitoring ocean structure on the mesoscale? A major effort in this direction might well be worthwhile..."

The importance of the higher frequency ocean dynamics features was recently highlighted by the mission of Paul Scully-Power aboard the Space Shuttle Challenger. His assignment was to observe the oceans, and he reported that ocean eddies and subsurface waves are ubiquitous and seem to be interconnected on a global scale. He was quoted by the Associated Press as saying

"for the first time we have seen a whole packet of very long internal waves associated with the north wall of the Gulf Stream. These particular waves were inboard of the north wall, in other words, in the Gulf Stream itself. This combination of spiral eddies outside the Gulf Stream and the long internal waves inside...is a combination that's never been seen before..."

Concrete research interests to oceanographers now include the dynamics of eddies, the specific dynamical behavior of the tropical ocean, and the Antarctic Circumpolar Current. Eddy activity is strongest in the vicinity of the earth's major currents: the Gulf Stream, the Kuroshio, the Brazil-Falkland Confluence, the Agulhas Current, and the Antarctic Circumpolar Current. The Gulf Stream and the Kuroshio are the two strongest northern hemisphere boundary currents and have profound influences on North Atlantic and Pacific Ocean circulation. The Agulhas is the major southern hemisphere boundary current. Eddies generated by this current transport a substantial amount of warm Indian Ocean water into the Atlantic, resulting in important interocean heat

exchange. The Brazil/Falkland Confluence is a complex region characterized by interfacing cold, fresh Antarctic water with warm, salty North Atlantic water. Eddy generation and decay, the interaction of eddies and currents, the interaction between eddies, and the role of near-surface eddy transport in the general circulation must be understood in these regions. The general circulation in the southern ocean is a continuous flow from the west to the east around the continent of Antarctica. This Circumpolar Current is the largest current in the world. It links the circulation in the three great ocean basins. It intervenes between the southern high-latitude deep-water formation regions around Antarctica and the mid-latitude temperate regions. The Circumpolar Current eddies appear to provide the transport mechanism for heat to be removed from temperate regions to the waters of the Antarctic where it is lost to the atmosphere.

A basic tool for measuring the oceanographic topography is the radar altimeter. Satellite altimetry is a mature satellite remote sensing technique with an extensive body of literature describing previous and current instrumentation and the scientific results from the four altimeters that have flown in space. An exhaustive review of this literature is not pertinent in this document, but the reader is referred to Miller and Hammond (1972) and McGoogan et al (1976) for information about the SKYLAB S-193 altimeter; to a special issue of the Journal of Geophysical Research (vol. 84, no. B8, July 30, 1979) for literature about the GEOS-3 instrument and satellite; to Barrick and Swift (1980), Townsend (1980), and two special issues of JGR (vol. 87, no. C5, April 30, 1982, and vol. 88, no. C3, February 28, 1983) for papers dealing with the SEASAT altimeter; and to a special issue of the Johns Hopkins University Applied Physics Laboratory Technical Digest (vol. 8, no. 2, April-June, 1987) for GEOSAT information. Simple in concept, the altimetry technique consists of transmitting a narrow pulse of radio frequency energy to earth from an orbiting satellite platform and measuring the elapsed time required for the nadir-directed signal to return to the satellite instrument receiver. Accurate knowledge of the satellite's orbit from other means allows then the determination of the shape of the earth's topography along the narrow illuminated swath beneath the satellite.

The ocean's mesoscale energy is difficult to map with such conventional radar altimeters because of the narrow illuminated swath, regardless of the orbital configuration. To resolve mesoscale eddies adequately requires observations with a space-time resolution of at least 50 km and 20 days. The choice of orbit for nadir-pointing altimeters forces tradeoffs between spatial and temporal resolution. Orbits that provide adequate spatial sampling will not revisit a ground track very often, while repeat orbital configurations providing temporal resolution along a given ground-track will have widely separated ground tracks. There are two space-time variability domains in the dynamics of the oceans. One contains the large-scale annual fluctuations and the other the short space and time scales of the mesoscale eddy fields. GEOSAT and soon TOPEX are adequate for sampling large space and time scales but all nadir-pointing conventional altimeters fail to resolve the second, smaller scale variability domain (Bernstein et al, 1979). TOPEX will have a limited potential for characterizing the small scale (50-300 km) variability (Born, Lame, and Mitchell, 1984) but this is not satisfactory.

Two solutions are available. Multiple satellites bearing identical TOPEX-class altimeters could map the mesoscale ocean features if their orbits were all accurately known. However, funding multiple payload launches given the very limited launch vehicle inventory in the U.S. is not likely. The other recourse is to develop altimeters with multiple-beam illumination patterns. This concept is not new. Perhaps the first reference to such an instrument was by Brown (1972). McGoogan and Walsh (1978) presented a look at the future of altimetry and a multibeam altimeter definition study with The Johns Hopkins University Applied Physics Laboratory was initiated by NASA

Headquarters in July 1978. From this investigation, numerous internal reports were produced (McArthur, 1979; Bush et al, 1980) and a summary report by Bush et al (1984) was subsequently published in the open literature. The scientific community is not unaware of the potential of this sensor. Mooers et al (1984) claim that

"a modest incremental investment in a clever modification would produce a wealth of additional information with multibeam altimeters..."

The Altimetry and Precision Orbit Determination Panel for the Earth Observing System (EOS) concluded (Volume III, Altimetric System Panel Report) that

"in principle, multibeam altimetry allows the generation of a finite swath (about 100 km) of altimetry observations along the ground trace, thereby mapping mesoscale eddies. As part of the EOS altimetry program, the development of this new multibeam concept should be fostered..."

Because the scientific measurements of interest for the multibeam altimeter of the future center on the ocean eddy, it is necessary to characterize the topographic measurement requirements. If the hydrodynamic flow features a balance between the Coriolis and pressure gradient forces, then the flow is geostrophic and can be mathematically expressed as

$$\vec{\nabla}_{HP} = -\rho f \hat{k} \times \vec{V}_g \quad (1)$$

where  $p$  is pressure,  $\rho$  is density,  $f$  is the Coriolis parameter,  $\hat{k}$  is a unit vector in the vertical direction, and  $\vec{V}_g$  is the geostrophic current velocity. The gradient is referred to the Cartesian frame of reference. In the earth's gravity field, the ocean surface is an equipotential surface so it is convenient to express (1) in isobaric coordinates. Then, after solving for  $\vec{V}_g$ ,

$$\vec{V}_g = \frac{g}{f} \hat{k} \times \vec{\nabla}_{pz} \quad (2)$$

Thus, the velocity field is directly related to the tilting or slope of the surface. Future altimeters must be able to measure the amount of this tilt so that the velocity of mesoscale eddies can be computed. Figure 1 shows a typical topographic record from a satellite altimeter. The insert contains a map of the groundtrack of GEOS-3 as it passed from east to west across the Gulf Stream on September 20, 1975. In the main figure, time is actually increasing from right to left but the plot is presented as a function of distance from the land-sea boundary. The Gulf Stream's western wall is easily recognized at a distance of 250 km from the coast. A 1 m elevation rise is evident between the western wall and the eastern wall. The mean equipotential surface shape, the marine geoid, has been extracted so that the elevation record is due only to dynamics. For eddies, Ousbourn (1982) found that on the average, eddies in the North Atlantic have radii of 30 km, amplitudes of 45 cm, and translational velocities of 2.5 km/day. A synopsis of an optimized sampling strategy for mesoscale eddies was written by Hurlbert (1984). The conclusion called for measurements to be made at spatial intervals of 25-30 km on a daily basis. The required elevation accuracy is 5 cm. Therefore, the altimeter's measurement precision must be better than this number. TOPEX will make topographic measurements with a precision of 2-3 cm. Therefore,

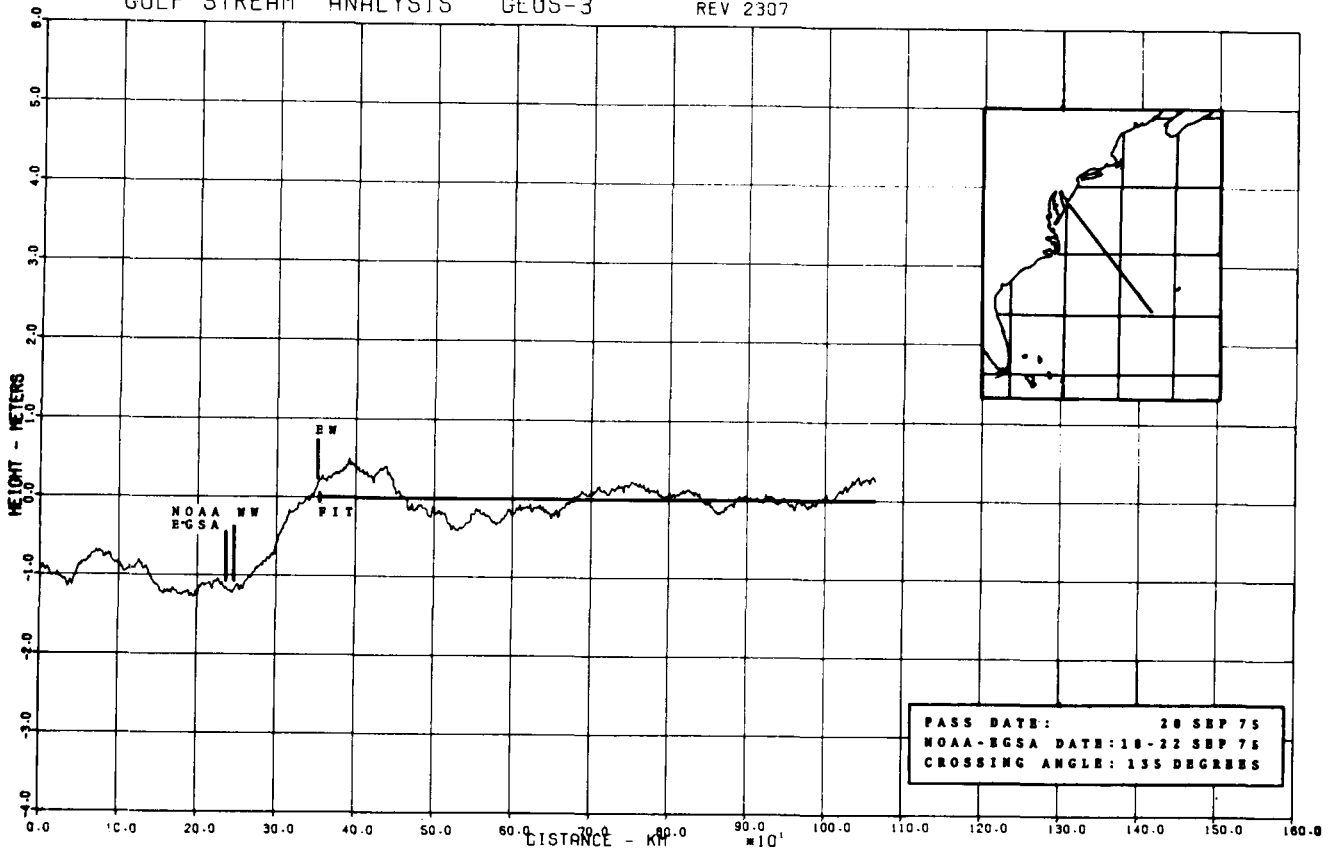


Figure. 1. Single GEOS-3 topographic profile indicating the Gulf Stream's eastern (EW) and western (WW) boundaries as estimated by Leitao *et al* (1978) and the western boundary as estimated by NOAA-EGSA.

TOPEX quality elevation measurements are needed for future altimeters across a swath of at least 100 km width with samples every 25-30 km across the swath.

If this data were available, then the surface curvature could be measured as well as the slope. Lee and Parsons (1986) have shown that the curvature, when given as the Laplacian of the surface topography, is related to the vorticity of the surface geostrophic current. Vorticity is an extremely useful parameter for describing large-scale geostrophic flows but it is virtually impossible to measure by conventional methods. The typical mid-ocean eddy may have a velocity scale of 20 cm/s varying over about 100 km, which corresponds to a vorticity of  $2/1,000,000 \text{ s}^{-1}$ . Sufficiently accurate multibeam altimetry would thus create an entirely new capability, the ability to measure the vorticity of the mesoscale field directly.

## 2.2 The Land

The earth's land surface, in contrast to the oceans' surface, is familiar to us. It is where we live. We can see its topography, and we can detect the importance of topography in our lives. In the

mountains, we physically feel the effect of reduced atmospheric pressure. We become winded from exertion that is routine at mean sea level. The high relief in mountainous regions impacts the construction of homes and buildings, and our choice of occupation depends on our geographic location. Farming, for example, is difficult on the slopes of hills and mountains. Instead, farming requires the level ground and good soil of plains and large valleys. The availability of water for crops and homes depends in large part on the topography. Highly populated regions, especially in the western portion of the United States, have grown dependent upon the runoff from melting snow fields high in the mountains many hundreds of miles distant. The amount of runoff is obviously a function of the snowfall, which depends upon meteorology. The availability of the runoff to a certain geographic region depends upon the topography. In other areas, the inability of the terrain to absorb or disperse water is a hazard. Near the banks of major rivers and streams and near the coastal areas, local flooding from storm systems can threaten homes, property, and lives. The susceptibility of a given area to flooding can impact insurance rates and real estate sales.

In addition to these very utilitarian examples of the importance of land topography, there are many additional scientific reasons to know the earth's topography. A recent report entitled "Report of the Topographic Science Working Group" summarizes the scientific requirements for global topographic data. These are discussed under the separate headings of 1.) Hydrology, Vegetation, and Ecology, 2.) Continental Geophysics, 3.) Geology and Geomorphology, and 4.) Polar Science. The latter discussion is referenced in section 2.3 of this volume. The reader is referred to the Topographic Science Working Group's report for further information about scientific applications for topographic data. In section 3 of this volume, more detail is included about particular applications of high resolution topographic data that can be provided by the MARA. The following paragraphs are a summary of the working group's discussion of scientific applications for land topography data.

The disciplines of hydrology, vegetation, and ecology can be lumped under the single title of ecosystem studies. Under this broad heading, topography affects climate and vegetation in three basic ways. Mountains cause the cooling of air masses as they pass overhead. Cooler temperatures affect plant physiology and contribute to changes in soil/plant water budgets. The movement of air masses over mountain ranges also causes forced lifting on the windward side and subsidence on the leeward side. The adiabatic cooling from the former produces condensation and precipitation; the adiabatic warming from the latter suppresses precipitation. Both of these effects are important to weather forecasting. Also important is the friction introduced by rough terrain. This affects the atmospheric energy budget and creates standing atmospheric waves that must be accounted for in atmospheric circulation modeling. Another subdiscipline within ecosystem studies is biogeochemistry, which deals with the movement of nutrients within the ecosystem. Ecological cycles include all components of the biosphere, including the soil, the water bodies, and the atmosphere. Leaching and runoff are affected by the topography. Plants and animals tend to inhabit selected areas of the ecosystem, depending upon their abilities to adapt to differing climates and terrain. Biogeography includes the identification of the habitats of various plants and animals and the study of the effects of man on these. Therefore, it is important to measure the canopy heights of various plant species, the vegetation density (which is directly applicable to deforestation studies), seasonal foliation, plant health, and the underlying surface roughness. The study of radiation balance and microclimate requires topographic knowledge because relief controls the incident solar radiation, thermal reradiation, and reflection and emission. The radiation balance in turn affects snowmelt, the wind, and soil moisture. Topographic data is essential for modeling drainage basin structure and runoff and stream channel location. Snowmelt is affected

by the absorption of surface radiation, which is affected by topography. The amount of snow pileup at a location also depends on topography with little accumulation occurring on steep slopes. And, the redistribution of snow pileup by avalanches is a function of topography.

Under the discipline heading of continental geophysics are studies of plate motions, plate boundary interactions, and earthquake occurrence. Variations in the earth's topography directly reflect both vertical and horizontal forces at work in the lithosphere. Topographic data are essential for gravity field investigations and magnetic anomaly studies.

Within geology and geomorphology are numerous structural and tectonic applications. The earth's surface relief shows evidence of the processes leading to the formation and subsequent evolution of surface features. Topography therefore reflects the interplay between the tectonic and volcanic processes of formation and erosional destruction. The extent to which these processes are in equilibrium is critical in understanding many terrestrial geologic problems.

As noted in the referenced report, there is a serious lack of adequate topographic data. At present, data is available in the form of contour maps interpolated from spot elevation measurements and in digital form. The latter data sets are at present merely digitized from existing contour maps. Much of the world is totally unmapped. For the rest, the available maps are of different scales and the measurements used in the mapping are of variable quality. The relative accuracy of elevation measurements is important when topographic measurements from adjacent areas are to be merged into a larger data set. Absolute accuracy is important when changes in topography over time are to be monitored. And, the currency of the measurements is important in regions where surface topography does change with time. The ability to monitor topographic details must be exercised periodically if elevation changes are to be properly monitored.

The "Report of the Topographic Science Working Group" does recommend the development of a monitoring capability for collecting a global topographic data set.

"Three scales of observations are required. A global data set of moderate resolution (defined loosely as 1000 m horizontal resolution, and 10-100 m vertical resolution) is a first requirement. This should be supplemented by a higher resolution (100 m horizontal, 1-10 m vertical) regional-scale data set. The ability to acquire this data set anywhere on the globe is critical, although initially global coverage may not be required. In selected local areas, very high resolution topographic data are required for special studies..."

Table I summarizes the requirements for topographic data at these various scales for each of the disciplines and subdisciplines described above. The resolution is noted, the repeat interval for the required measurements is listed when applicable, and the technology capable of making the measurements is indicated. The only competing techniques listed are for space platforms. Obviously, some approaches benefit certain applications while others have advantages for different applications. The strongest recommendation of the Topographic Working Group is for a narrow-beam, scanning radar altimeter to produce the high resolution global data set (100 m horizontal and 1-10 m vertical resolution) required for the majority of these applications.

Table I. Land Topographic Mapping Scientific Application Requirements.

Discipline: Hydrology, Vegetation, Ecology

Application	Topo Scale	Repeat Interval	Technology				
			SO	AL	ARNS	ARW	I
Global vegetation/ climate	G	-	?		X		
Biogeochemistry	G	-			X		
Biogeochemistry	R	-	X				X
Radiation and microclimate	R	-	X	X	X		X
Radiation and microclimate	L	5-10 yrs?					X
Hydrology	R	-	X	X	X		X
Hydrology	L	yearly?		X			
Seasonal snow cover	R	yearly?	X		X		X
Seasonal snow cover	L	yearly?	X	X			

Discipline: Geophysics

Application	Topo Scale	Repeat Interval	Technology				
			SO	AL	ARNS	ARW	I
Crustal structure							
Gravity	G	1			X		
Magnetics	G	1			X		
Continental flexure	G	1		X	X		
Long-wavelength isostasy	G	1			X		
Plate boundary interactions	G	1		X	X		

Topographic Scales: G - Global - 1 km horizontal, 10-100 m vertical; R - Regional - 100 m horizontal, 1-10 m vertical; L - Local - 10 m horizontal, 0.1-1 m vertical.

SO - Stereo Optical; A - Altimetry; AL - Laser; ARNS - Radar, Narrow beam, Scanning; ARW - Radar, Wide beam; I - Interferometry.

Table I. (continued)

## Discipline: Geology and Geophysics

Application	Topo Scale	Repeat Interval	Technology				
			SO	AL	ARNS	ARW	I
Active faulting and folding (high resolution techniques)	R	5-10 yrs.	X	X	X		X
Hypsometry for planetary comparisons	G	-			X		
Hypsometry for process studies	G R	-			X		X
Global geomorphic province mapping	G	-			X		
Largest landforms (deltas, valleys, piedmonts)	G	-			X		
Mid-sized landforms (fans, moraines, small valleys)	R	-		X	X		X
Small landforms (terraces, large sand dunes)	R L	5-10 yrs.		X			X
Small process-oriented units (stream channels, hillslopes)	L	5-10 yrs.			X		
Impact craters	R	-			X		
Tectonic landforms (inactive mountain belts)	G	-			X		
Volcanic landforms							
Volcanoes	G R	5-10 yrs.		X	X		
Lava flows	L			X			X
Landforms of active volcanism	R L	5-10 yrs.		X			X
Planation surfaces	G R	-			X		
Drainage density	G R L	-		X	X		
River flood	L	yearly			X		
Major alpine landslide	R	5-10 yrs.		X			X
Small alpine landslide	L	yearly		X			X

Topographic Scales: G - Global - 1 km horizontal, 10-100 m vertical; R - Regional - 100 m horizontal, 1-10 m vertical; L - Local - 10 m horizontal, 0.1-1 m vertical.

SO - Stereo Optical; A - Altimetry; AL - Laser; ARNS - Radar, Narrow beam, Scanning; ARW - Radar, Wide beam; I - Interferometry.

## 2.3 The Ice Sheets

Topographic measurements of the earth's polar ice sheets may be considered as land measurements and, as such, should be discussed in section 2.2. However, the unique applications of such measurements in polar science constitute a strong justification for a separate discussion. The ice sheets are largely uninhabited. Thus, the utilitarian applications for polar topographic measurements that were cited for land measurements are lacking. The scientific importance of polar topography information, however, cannot be overstated. 80 to 90% of the globe's fresh water is contained in the polar ice sheets. Changes in the volume of these sheets would have direct and serious consequences to mean sea level and climate. Are the ice sheets stable, growing, or shrinking? Global warming due to the carbon dioxide-induced greenhouse effect may cause the ice sheet volume to be reduced. This would have catastrophic implications for the large populations of people living in coastal regions. The stability of the West Antarctic ice sheet is of particular concern. Warming could cause its disintegration within a few hundred years. It is particularly vulnerable because it is grounded below mean sea level. Early signs of its disintegration include ice thinning, increased calving from the shelves, and an inland migration of the line marking the joining of the ice shelf to its subsurface base. Currently, it is thought that sea level is increasing at a rate of 1 mm per year; the disintegration of the West Antarctic ice sheet would increase sea level by 3.5 m.

In addition to these obviously important requirements for the monitoring of ice sheet volume, there are significant scientific needs for other ice sheet measurements. The location and identification of ice domes, ice divides, drainage basins, ice streams, ice rises, ice shelves, grounding lines, and coastlines is important for strictly mapping purposes. Detailed and repeated measurements of topography in certain regions could help assess the ice accumulation rate, the transportation rate of ice from the center of a sheet to its edge, and ice ablation due to calving and thinning.

Table II contains a summary of the scientific requirements of the polar ice community for topographic data of varying resolution. The capability of various measurement techniques is also listed. Radar systems have the obvious and significant advantage that they are not susceptible to atmospheric attenuation due to clouds and precipitation.

## 3.0 MARA DEVELOPMENT GOALS

### 3.1 General

The many scientific applications for topographic data summarized in section 2.0 cover a broad range of disciplines with a variety of spatial and temporal resolution requirements. The Multi-mode Airborne Radar Altimeter (MARA) development was commissioned by the Oceanic Processes Branch of NASA Headquarters for the expressed purpose of supporting advanced ocean altimetry development studies. Future satellite altimeters following the deployment of TOPEX in 1991 are certain to have enhanced capabilities, including possibly wide swath mapping, adaptive tracking, coherent processing, and the use of multiple frequencies. These new techniques require development and the MARA has as its primary mission the study of these new approaches. The scientific requirements for ocean advanced altimetry were discussed in section 2.1. In the following section, 3.2, these requirements are translated into ocean application development goals for MARA, given the limited flight altitudes possible with available aircraft. Similarly, sections

Table II. Polar Ice Topographic Mapping Scientific Application Requirements.

Requirements for basic inventory of polar ice cap topography.

Feature	Resolution		Repeat Interval (years)	Technology				
	Vertical (m)	Spatial (m)		SO	AL	ARNS	ARW	I
Large-scale features	10	500	5-10	X		X	X	X
Ice domes								
Ice divides								
Drainage basins								
Ice streams								
Ice rises								
Ice shelves								
margins								
grounding lines								
Coastline								
Medium-scale features	1	100-500	5-10		X	X		X
Undulations								
Rifts								
Crevasses								
Flow lines								

SO - Stereo Optical; A - Altimetry; AL - Laser; ARNS - Radar, Narrow beam, Scanning; ARW - Radar, Wide beam; I - Interferometry.

Requirements for mass balance and ice dynamics.

Feature	Resolution		Repeat Interval (years)	Technology				
	Vertical (m)	Spatial (m)		SO	AL	ARNS	ARW	I
Ice volume change	0.10	500	5		X			
Ice dynamics	0.10-0.50	100-500	1-5		X			
Gradients								
Flow features								
Ablation	0.10-0.50	100-500	1-5		X			
Grounding lines								
Ice shelf margins								
Ice rise margins								
Rifts								
Crevasse fields								
Icebergs								

SO - Stereo Optical; A - Altimetry; AL - Laser; ARNS - Radar, Narrow beam, Scanning; ARW - Radar, Wide beam; I - Interferometry.

3.3 and 3.4 contain reasonable development goals for MARA for land and ice sheet applications based upon the scientific community's expressed requirements for topographic data presented in sections 2.2 and 2.3, respectively.

### 3.2 The Oceans

It is clear that the next plateau to strive for in oceanographic altimetry science is to perfect wide swath coverage with no loss in tracking precision. The scientific needs in section 2.1 center on the measurement of mesoscale oceanic features, which in turn requires a wide swath altimetry coverage. The goal from space would be to measure the topographic shape of a mesoscale eddy over an area 100 km wide with a precision of 2-3 cm, the TOPEX height measurement precision.

NASA's ER-2 research aircraft has a cruising altitude of 20 km. To achieve a swath width extending 50 km to either side of the vehicle's groundtrack would require a maximum off-nadir angle of 68 degrees. To make precise surface elevation measurements at this off-nadir angle is impossible. Among other difficulties, at that angle, the backscattering from the ocean is governed by the so-called "Bragg scattering" physics. Whereas, the conventional nadir altimetry return is dominated by specular reflections adequately described by physical optics. The off-nadir backscattering at angles greater than about 15 degrees is not adequately supported by theory. The boundary perturbation theory used at those angles is modified in an ad hoc fashion by the local tilting of the mean flat surface by the large energy-containing waves. The backscattering cross section at the large off-nadir angles is some 40-50 dB below the levels at nadir according to these theories and some limited radar measurements. Therefore, it is not possible or even desirable to attempt to use backscattered returns from nadir and 68 degrees off-nadir in the same instrument and for the same application. Instead, we seek to limit our operation to within 15 degrees of nadir. In that way, the MARA will measure solely in the physical optics scattering regime with backscattered signal levels within 10 dB of the peak nadir return (Brown, 1977).

With this off-nadir angle constraint, we are limited to a maximum swath width of 10 km even using the ER-2 aircraft as our platform. This is not a sufficient width to map the three-dimensional shape of oceanographic features such as mesoscale eddies or boundary currents. Therefore, we are forced to abandon any attempt to develop the capability of operational mapping of these features. This must be left to future satellite altimeters. Instead, we concentrate in our development on proof-of-concept demonstrations using MARA. In particular, our major goal is to determine the degradation of tracking precision with off-nadir angle. This is of fundamental importance to future altimetry and techniques for minimizing this degradation must be developed if future advanced satellite altimetry is to become a reality. Since the altitude of the MARA platform is no longer of central importance, we choose the NASA P-3 research aircraft (NASA 428) as our platform. As a cruising altitude, we now use 10,000 ft., which is a comfortable altitude for that vehicle.

There are several secondary development goals that we will also address using the MARA. The concept of using a forward-looking beam to provide advanced "warning" that a change in the surface topography is imminent can be tested with MARA. The configuration of beams selected will include the capability of implementing a forward-looking beam. The information from that beam will be used in an adaptive-tracking algorithm to optimize range tracker performance. Suitable algorithms will be developed to reduce the tracking precision from levels achieved in the absence of the forward beam. This new technology should be especially useful at boundaries between land and sea or between any two surfaces of differing backscattering properties.

The other development goals stemming from the oceanographic community's scientific requirements for advanced altimetry involve the maintenance of measurement capabilities that have already been proven and accepted with conventional nadir altimeters. Satellite altimetry can quantitatively measure the significant wave height of the ocean and the wind speed along the satellite's groundtrack. And, a scanning aircraft altimeter, the Surface Contour Radar, has been used to make definitive measurements of the ocean's directional wave spectrum. The MARA will be used to determine if it is possible to extend these geophysical measurements to the off-nadir angles contained in an advanced altimeter's swath of coverage. The SCR mode of the MARA system will continue the directional wave spectra measurements of its ancestor. These are lower priority goals than the evaluation of tracking precision degradation off-nadir but important nonetheless. A nadir beam will be required in the MARA's beam configuration to offer a standard of comparison for the tracker performance studies and for the significant wave height, wind speed, and directional wave spectrum studies.

The proposed EOS Land and Ocean Radar Altimeter (LORA) will use an interferometric antenna to produce illumination footprints at 25 km intervals on each side of the satellite's groundtrack. Seven beams in total have been proposed. The interferometric mode of the MARA will be used strictly as an engineering demonstration of this design. Therefore, this mode will not be expected to produce scientifically usable data but to pave the way for the extremely powerful LORA radar system.

### 3.3 The Land

Many of the advanced altimetry measurements required for various land applications can, of course, be made from satellite altitudes. In section 2.2, three scales of resolution were cited. The global scale has a horizontal resolution of 1 km. From the P-3, the total swath width for a maximum off-nadir observation angle of 15 degrees is 1.64 km. The total swath width then could be used to generate a single topographic sample, or pixel, in a globally useful topographic map. At the regional and local resolution scales called for, a horizontal resolution of 100 m is needed. If the MARA antenna has a large enough aperture, a beamwidth of 1.88 degrees would produce a groundspot, or pixel, with 100 m diameter. Clearly then, the MARA has the potential to produce topographic measurements at all three scales of roughness important to land processes studies. Any measurements at the global scale would undoubtedly be made in support of satellite measurements. But, the potential high resolution in the horizontal makes the MARA an attractive and unique data source for a number of the applications discussed in section 2.2. Furthermore, the extremely high vertical resolution that is required of the system to satisfy the ocean community's requirements will be impossible to match through any other means.

The oceanographic applications have the highest priority in the design of MARA. Therefore, system design is based on the oceanographic requirements. But, the MARA system should be an invaluable tool for the land and ice science communities. In the remainder of this section, specific land applications are discussed. Because of the uniqueness of this instrument for the medium and high resolution applications, the discussion centers on them.

Any altimeter signal contains two distinct categories of information. The ranging information is derived from the delay in time between the transmission of a radar-frequency pulse and its reception back at the receiver. The backscattering information is contained in the amplitude of the received waveform and the waveform's shape. This latter category of information is particularly important for biogeography applications. Plant and animal species occupy areas of the land

surface that have the proper environment for them to thrive and prosper. To understand what these optimum habitats are for particular species, it is important to be able to monitor such characteristics as a habitat's vegetation density, the height of plant canopies, the seasonal variation in foliage, the health of a plant cover, and the roughness of the underlying land surface. The vegetation density is of increasing importance now with the deforestation of huge portions of the earth's rain forests in the tropics. Accurate surveying of the loss of vegetation cover will be important to assessments of the impact of deforestation on global climate. The height of the plant canopy can be determined if there are multiple peaks in the backscattered waveform shape. Some preliminary work in this area was conducted by Brooks and Norcross (1983) using satellite altimetry data from GEOS-3. They were able to measure the height of the trees and sawgrass above the surface in the Florida Everglades. The amount of penetration of the altimeter signal to the surface will vary with the amount of foliage. There is no known experience to date with radar signals over land, but lidar ranging systems have been used to measure penetration through tree canopies (W. Krabill, personal communications, 1988). Similar success at microwave frequencies should be achievable. With penetration, it may be possible to measure the plant canopy heights and the topography of the underlying surface. This total package of capabilities should be very valuable for biogeographers.

There are a number of topographic applications for aircraft altimetric measurements of land surfaces. Mainly, they are the same as those mentioned in section 2.2 for the satellite case but with the sacrifice of large spatial coverage for high horizontal and vertical resolution. Figure 2 shows a generalized surface with a significant amount of relief. For the satellite case, the picture is applicable if the x and y axes scales are in tens of kilometers and the z scale is perhaps in tens of meters. For an aircraft altimeter, the x and y scales would be in meters and the z scale in centimeters or meters. For selected regions, the topography can be mapped from the aircraft altimeter thereby providing data to aid investigations of radiation balance and microclimate. The incident solar radiation, the thermal reradiation, the amount of snowmelt, windspeed, and soil moisture are all affected on the microscale by the local topography. Within such a regional or local study area, analyses of the drainage from the area would be possible thus aiding in hydrological studies. It would be possible to monitor snowmelt and snow pileup and to watch for likely occurrences of avalanches. For the geologists and geomorphologists, on this scale it would be possible to study the formational and destructional processes at work on particular landforms. Naturally, hypsometry, the study of the frequency distribution of topography, would be easily accomplished with aircraft altimetry data. Topical studies of individual landforms, such as terraces, large sand dunes, volcanos, lava flows, flood plains, and alpine landslides, would be possible as well.

There is little published information about altimetry over land. Of the satellite instruments, only GEOS-3 was operated for a significant amount of time over land. None of the altimeters were designed to optimally collect such data. The paper by Miller (1979) is one good reference for land applications of satellite altimetry data. The aircraft altimeters that have been built were designed to provide validation for the satellite instruments. Consequently, they are not suitable for the applications discussed in this section. The MARA is the first aircraft altimeter with land application requirements included in the design. This makes the MARA an extremely attractive and valuable resource for the EOS LORA instrument. LORA will have the capability to produce global topographic maps. MARA should be able to provide validation for the LORA land mode in selected geographic areas. This role for the MARA has been proposed as part of the LORA effort.

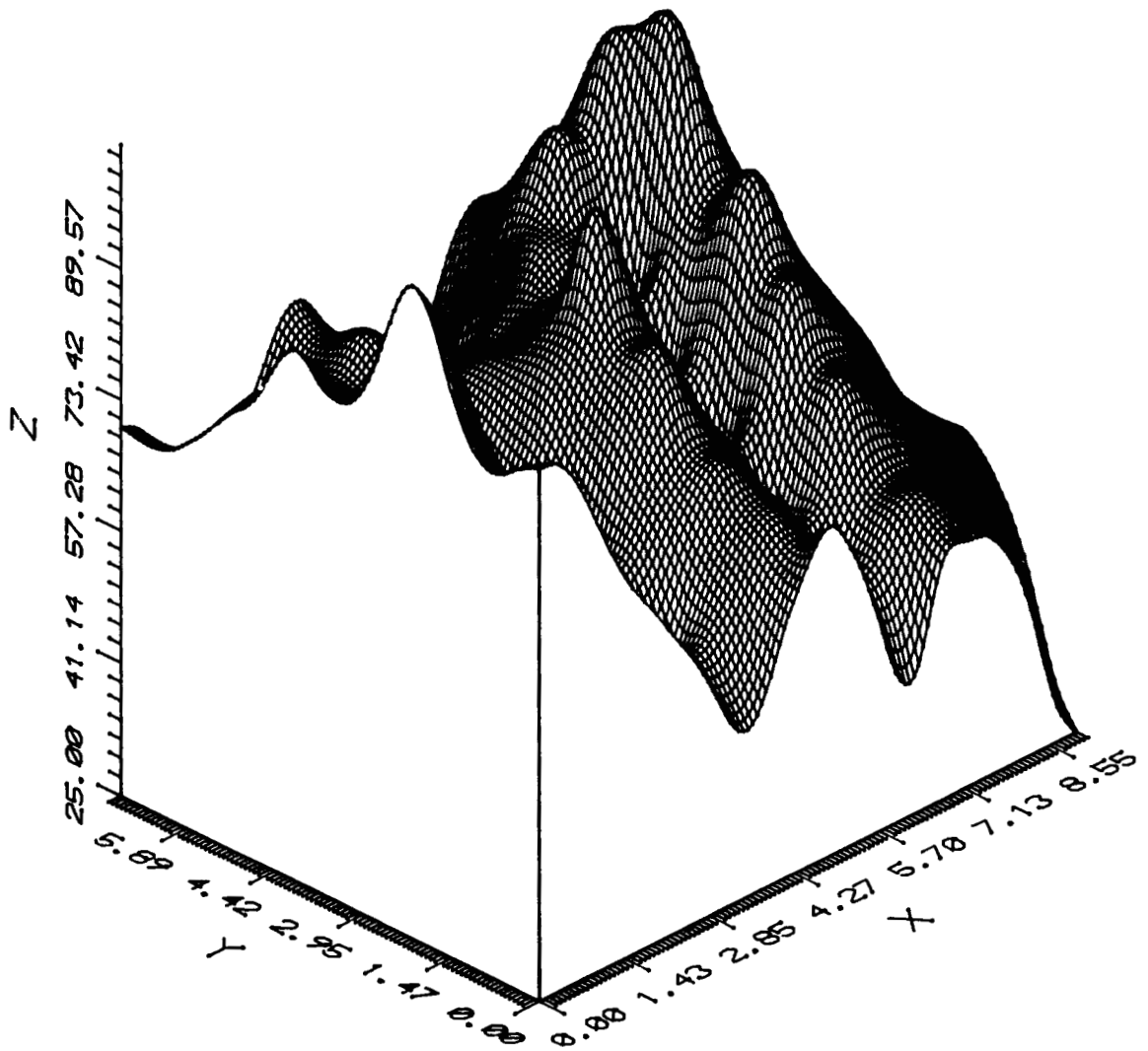


Figure 2. Generalized surface with high relief.

### 3.4 The Ice Sheets

On regional and local scales, an aircraft altimeter is a potentially valuable tool for polar science. At very high horizontal and vertical resolution, topographic data can be gathered that will aid in studies of ice accumulation, ice gradients, flow features, and ablation. In particular, it should be possible to study in detail such features as grounding lines, ice shelf margins, ice rise margins, rifts, crevasse fields, and icebergs.

In contrast to the land applications, there is some published material about the use of satellite altimeter data for polar science. Following the first published use of altimeter data by Brooks et al (1978), other papers by Brooks (1979), Zwally et al (1983), Martin et al (1983), and Brenner et

al (1983) have extended the use of data from GEOS-3 through SEASAT. Current work is underway by several groups using GEOSAT data. As for land applications, the MARA should be able to produce invaluable validation data for LORA investigators in the ice science community.

## 4.0 MARA INSTRUMENT DESIGN PARAMETER STUDIES

### 4.1 Design Goal Priorities

There are many design tradeoffs involved in the development of a complex remote sensing instrument system, especially if it is being designed to support applications in a wide variety of scientific disciplines. This is the case with MARA. The scientific requirements have been discussed in earlier sections. In this section, the requirements will be prioritized and studies are discussed which translate these science requirements into instrument design goals. The design parameters that will be discussed include the antenna system beam configuration, the maximum off-nadir beam angle, the beamwidth, the radar frequency, the transmitted pulse width, the pulse repetition frequency, and signal-to-noise ratio (S/N). The selected system parameters are used in section 4.7 to estimate the tracking precision of the resultant system using a statistical model.

The priorities are assigned in the following manner. To truly simulate the performance of a satellite wide swath altimeter, the aircraft instrument must also function over a reasonable swath width. As discussed in section 3.2, the swath width for MARA is set by the cruising altitude of the flight vehicle, the Wallops P-3, and the desire to stay within the specular backscattering regime over the ocean. Therefore, the ocean applications define the swath width for MARA. The requirement to study the degradation of tracking precision with off-nadir viewing angle over the ocean defines the horizontal and vertical resolution of the system. At an off-nadir angle of 15 degrees, the illuminated area on the surface is elongated strictly from the geometry. In section 4.2, it will be shown that this geometrical factor necessitates the use of a beam-limited altimeter. That is, the beamwidth must be made as narrow as possible so that the backscattered waveform is limited in temporal extent. Only with a narrowed waveform can acceptable tracking precision be attained. Therefore, the ocean applications impose requirements on the beamwidth which set the horizontal and vertical resolution for MARA. It will be shown that the resulting design parameters for swath coverage and horizontal and vertical resolution do not impose any limitations on the usefulness of the system for land and ice sheet applications. On the contrary, the system's capabilities are attractive for these purposes. The only impact of the land and ice sheet science requirements on the MARA design is on transmitter power. It will be shown that a significantly higher power is needed for land and ice mapping because of the very low backscattering cross-sections for many land surfaces and the variable slopes for terrain with high relief.

### 4.2 Beam-limited Altimetry

#### 4.2.1 Antenna Design

The swath width of the P-3 based MARA system is set by the aircraft cruising altitude and the need to stay within the specular reflection regime over the ocean. This defines the maximum off-nadir angle to be no greater than 15 degrees. In Figure 3, the viewing geometry for a finite off-nadir angle is shown. Conceptually, it is easy to see that the temporal extent of the waveform will greatly exceed the extent of the waveform from the same radar oriented to illuminate the nadir. In contrast to the nadir situation where the time duration of the footprint's illumination is

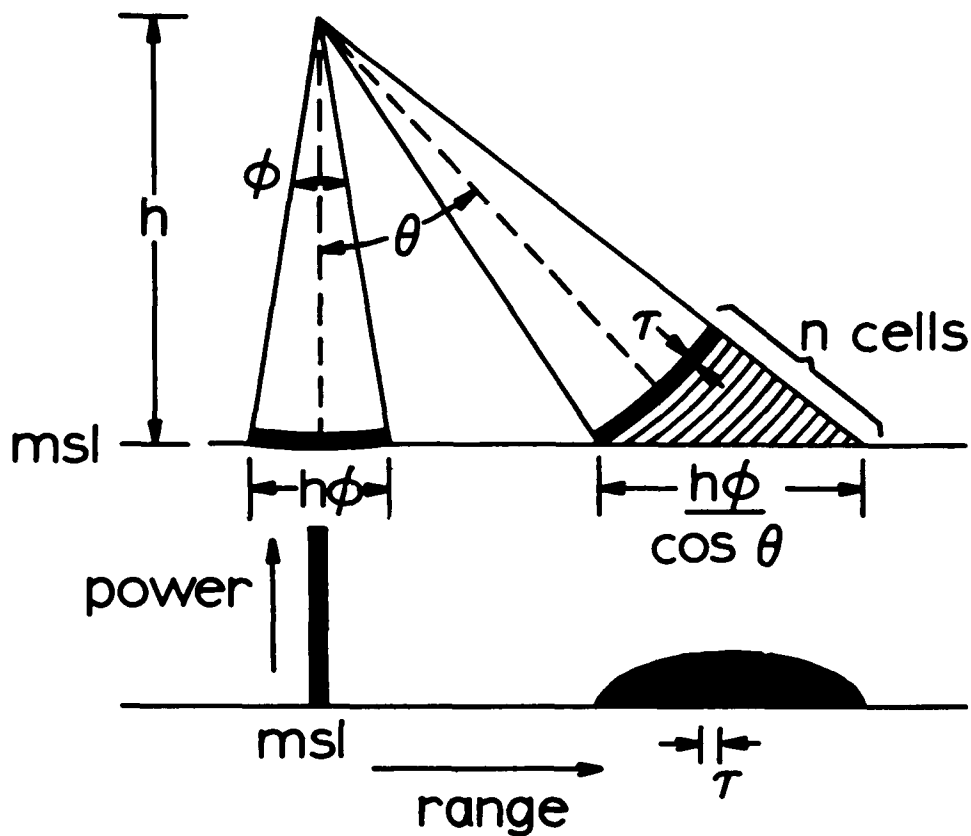


Figure 3. An illustration of the effect of off-nadir viewing angles on backscattered waveform shape.

essentially one pulsewidth long, the off-nadir footprint's illumination period lasts many pulsewidths. To a good approximation, the number of pulsewidths is given by

$$n = h\phi \tan\theta / \tau \quad (3)$$

where  $h$  is the altimeter's altitude,  $\phi$  is its full beamwidth,  $\tau$  is the pulsewidth, and  $\theta$  is the incidence angle. To do high precision range tracking, a sharp backscattered pulse waveform is needed. Figure 3 shows simplistically that this is not possible for a conventional altimeter looking off-nadir because of the smeared backscattered waveform. Narrowing the width of the backscattered waveform, or alternatively decreasing the footprint's size, can be achieved by using a beam-limited rather than a pulse-limited altimeter. For a target which fills the beam, a radar is considered to be beam-limited if the transmitted signal duration is long enough that the entire target is illuminated simultaneously. That is, in terms of the above equation, for a beam-limited radar the beam must be narrowed until only one pulsewidth is needed to illuminate the entire footprint. Beam-limited altimetry is not a developed technology; all altimeters to date have been pulse-limited. Simulations and analytical models to quantify the shape and size of the beam-

limited altimeter backscattered waveform are described in section 4.4. One analytical expression for the waveform shape was given by Barrick (1972) in the early days of radar altimetry. Basically, the shape is Gaussian. This is borne out by the simulation and model results in 4.4.

To narrow the waveform and thereby improve tracking precision at off-nadir angles, a narrow beamwidth is required and the beam pattern must be of good quality for incidence angles out to 15 degrees, the furthest extent of the swath. To accomplish this purpose, a dielectric lens antenna was selected for the MARA design. Because its performance is key to the system development, it was designed and fabricated as the initial step. This work was accomplished and the lens performance has been found acceptable (Parsons and Miller, 1988). The following summary of its characteristics is included for completeness in this volume. Its directive gain is 47.4 dB and the full 3-dB beamwidth is .625 degrees. Off-nadir, the performance degrades at angles approaching 15 degrees. In particular, astigmatism in the cross-scan direction of the lens becomes a significant problem at 15 degrees. For this reason, the maximum MARA off-nadir scan angle is reduced to 12 degrees. At that angle, the gain is reduced by 1.5 dB and the beamwidth in the direction perpendicular to the scan angle is increased to .95 degrees.

#### 4.2.2 Modes of Operation

The beam-limited Multibeam Mode antenna configuration is shown schematically in Figure 4. The nominal operating altitude is 3048 m. The lens is illuminated by five feed horns. One is positioned on the lens axis and the others are on two orthogonal arms. The location of the feed horns along the arms sets the off-nadir viewing angle. This nadir and diamond shaped beam configuration pattern was adopted because of its flexibility. With the diamond oriented with one forward-looking beam, one aft-beam, and two cross-track beams, the system can be used to address the look-ahead beam and adaptive tracking studies of interest for future altimetry. If the assembly is rotated by 26.6 degrees with respect to the flight direction, the five beams will produce groundtracks that are equally spaced. This will result in a "push-broom" pattern that will simulate the beam pattern proposed for the Land and Ocean Radar Altimeter (LORA) on the Earth Observing System (EOS).

The Surface Contour Radar Mode (SCR) will be possible through the use of an additional feed horn and a removable rotating mirror to scan the beam continuously in the cross-track direction. This mode is possible because the focal points for the lens for rays coming from -12 degrees through +12 degrees off the lens axis fall near a circle whose radius is 38 cm and whose center is on the lens axis and 76 cm behind the lens. Figure 5 indicates schematically how the rays would be collected for signals from nadir and 12 degrees off-nadir. The tick marks in the figure are at one inch intervals. Rays are shown coming from the effective diameter of the dielectric lens described in Parsons and Miller (1988). They are reflected by the mirror into the feed horn, which is on the lens axis and occupies the mirror position of the focal point. The right side of Figure 5 demonstrates that the mirror can always be rotated into a position which reflects the rays from off-nadir into the feed horn. The reason is that the focal point and the feed horn lie on the same circle, so the line joining them will always be a chord of the circle. To reflect the rays into the horn, the mirror must be the perpendicular bisector of the line joining the focal point and feed horn. But, that will always be a radius of the circle. The rate of scan of the mirror and the use of both sides of the mirror as reflecting surfaces directly affect the data rate and the resolution of the mapping of the surface using this mode. These issues are discussed in section 4.6. The MARA design includes the ability to incorporate this scanning mirror and single feed horn module as needed. Thus, the instrument system will be able to produce five fixed beams or a single

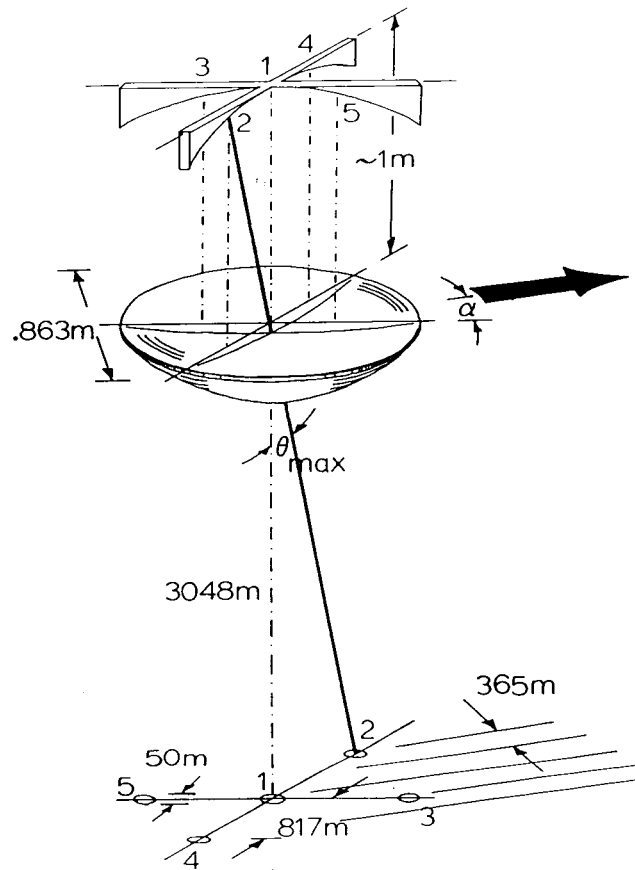


Figure 4. A schematic illustration of the lens and feed horn assembly for the Multibeam Mode.

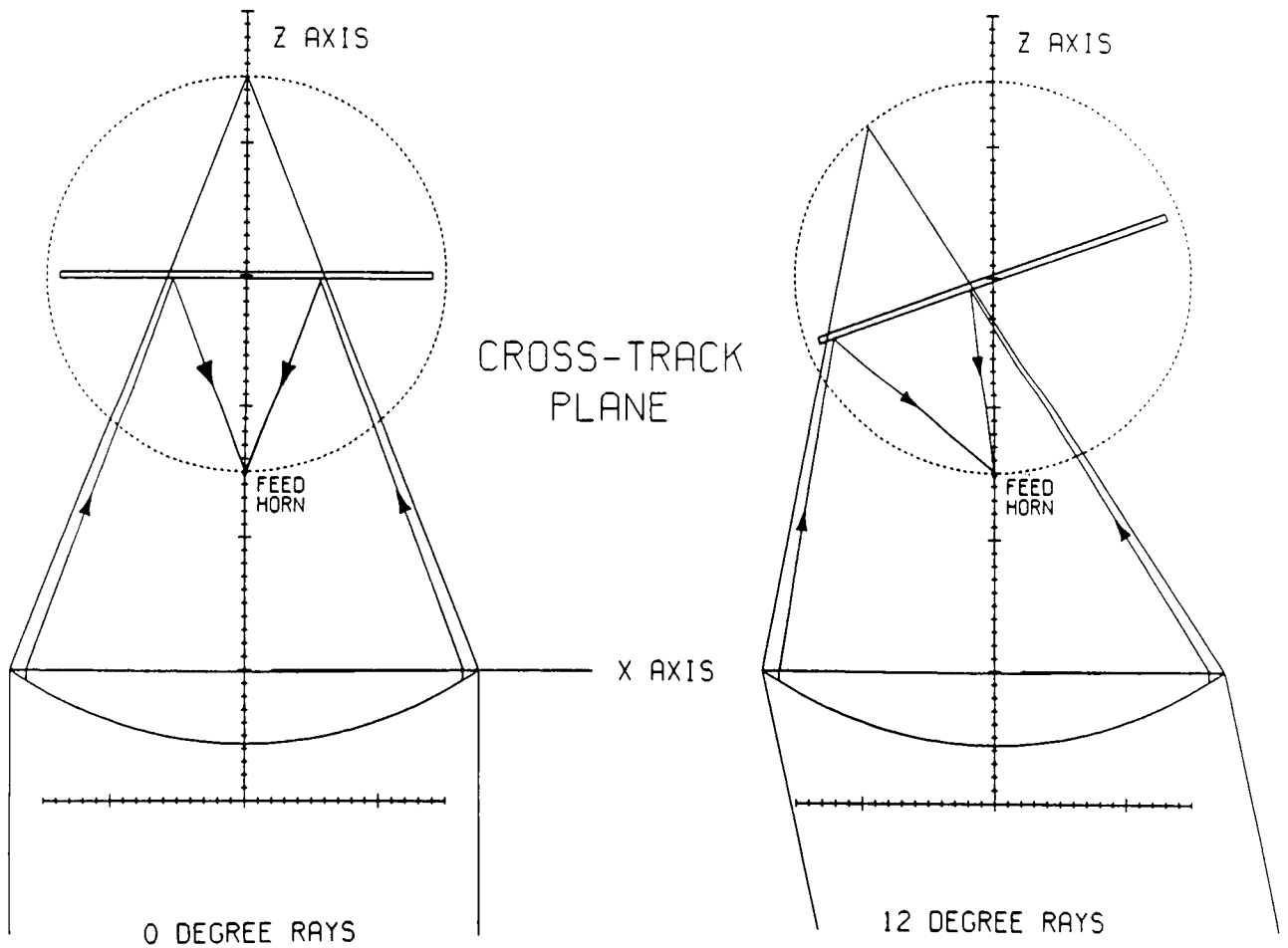


Figure 5. A schematic illustration of the lens and scanning mirror for the Surface Contour Radar Mode.

scanning beam as required.

The last mode of operation, the Interferometer Mode, is included in the MARA design because it is likely that future satellite altimeters will be interferometers to reduce the off-nadir footprint size (Parsons and Walsh, 1989). The LORA proposal is based on a two-dish interferometer concept first described by Bush *et al* (1984). In this mode, the dielectric lens is removed and the feed horns are replaced by a pair of small paraboloidal dishes oriented in the aircraft's cross-track direction. These will be boresighted to the same off-nadir footprint thereby simulating the two-dish interferometer. Appendix A contains a derivation of an equation that describes the antenna pattern from any two-dish interferometer. Using two 15 cm diameter dishes separated by 39 cm in this equation produces the antenna pattern shown in Figure 6. These results assume that the effective off-nadir viewing angle is 12 degrees, the same as the maximum viewing angle for the other two modes. The lobes of this pattern are of approximately the same width as the main beam generated by the lens in the Multibeam and SCR Modes. This antenna configuration will be used to determine the relative tracking precision capabilities of the Multibeam and Interferometer Modes. These studies will constitute a proof-of-concept demonstration for the satellite interferometric approach being proposed for future spaceflight missions.

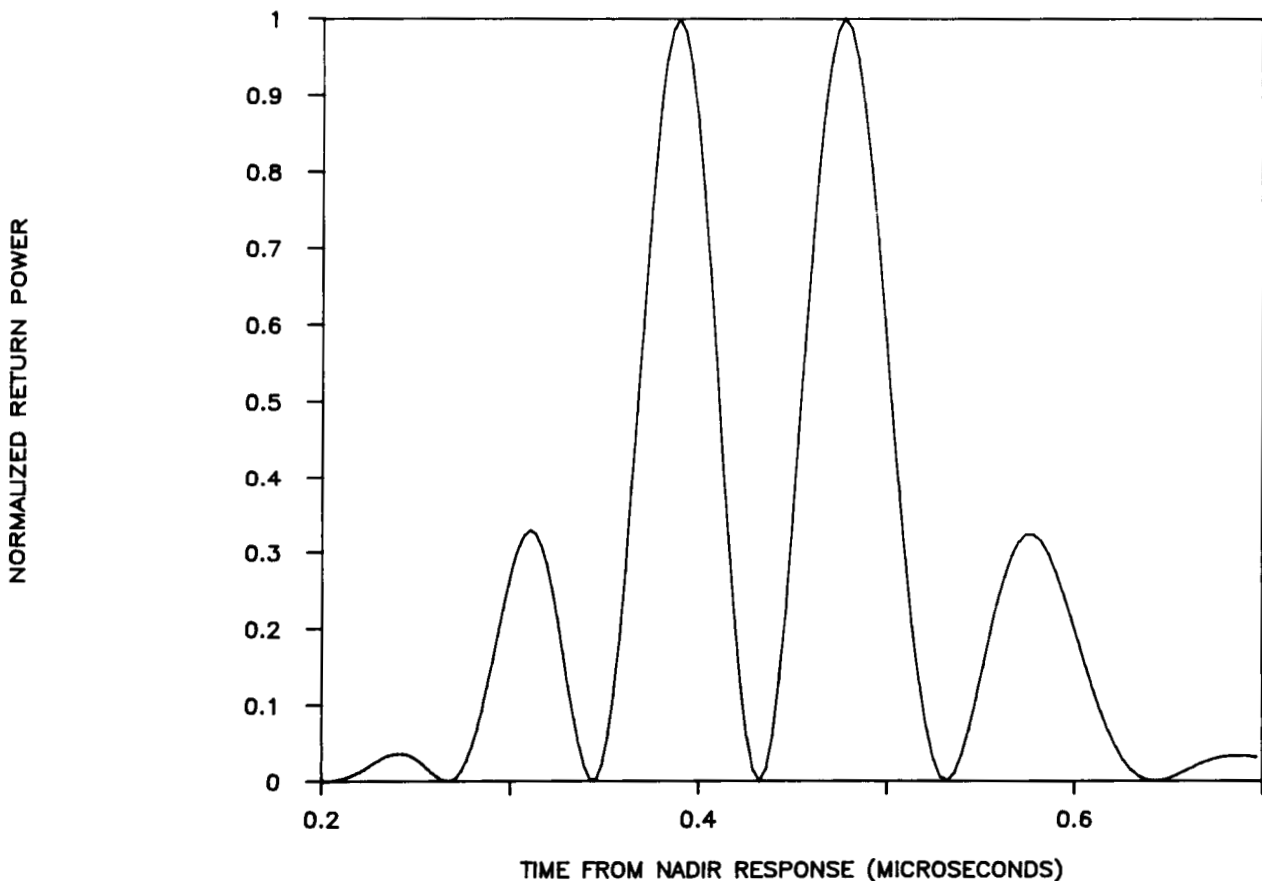


Figure 6. Expected Interferometric Mode waveform shape assuming that two 15 cm diameter reflectors separated by a baseline of 39 cm are boresighted to a footprint 12 degrees off-nadir from an altitude of 10,000 ft.

### 4.3 Frequency

There are several compelling reasons for the choice of frequency for MARA. The initial justification involves backscattering physics. From satellite altitudes, very small angles off-nadir will be adequate to produce the 100-200 km swath widths required for mapping oceanographic mesoscale features and boundary currents. For the EOS altitude of 824 km, only a 3.47 degree off-nadir angle is necessary to illuminate a spot 50 km to the side of the nadir groundtrack. For any frequency higher than C-band, the scattering from the roughened ocean at these angles will be governed by physical optics theory. Therefore, the MARA is designed to operate within this same scattering regime. Physical optics is mainly defined by the validity of the "tangent plane" approximation, which states that the electromagnetic field at any point on the surface is the sum of the incident field and the field that would be reflected by a plane surface tangent to the actual surface at the point of interest. This boundary condition is obviously a very good approximation for surfaces that are composed of irregularities with small curvatures. From elementary geometrical considerations, Brekhovskikh (1952) found that this is satisfied for

$$4\pi r_c \cos\theta \gg \lambda \quad (4)$$

where  $r_c$  is the radius of curvature at a point of interest and  $\theta$  is the local angle of incidence. For the aircraft instrument, the local angle of incidence will include the off-nadir viewing angle of the altimeter. That is, the local angles of incidence will be increased by as much as 12 degrees. To insure that the above inequality is still met, the only recourse is to increase the radar frequency. For radar altimetry, all satellite instruments have operated at frequencies close to 13.5 GHz. Obviously, there is good rationale for operating MARA at these same frequencies. But, because of the interest in off-nadir angles with MARA, the scattering physics argument forces us to consider higher frequencies. The next frequency band within an atmospheric window (i.e., a frequency band where there is little atmospheric attenuation) is around 36 GHz. There is considerable component development work being done at these frequencies so that the hardware needed for MARA is available.

The other equally compelling reason to operate at 36 GHz deals with the size required for an antenna aperture to produce footprints of a given dimension. Future wide swath satellite altimeters must be beam-limited as discussed previously. To reduce the size of the illuminated footprint (i. e., to be beam-limited) requires that the aperture dimension be increased at a given frequency. To keep the aperture fixed in size requires the use of a higher frequency. This is easily demonstrated with the use of the Airy pattern. Originally derived by G. B. Airy in 1835 to describe Fraunhofer diffraction at a circular aperture (Born and Wolf, 1964), the mathematical formula is also valid as a description of the power density distribution for a microwave signal transmitted through a circular aperture with uniform illumination. The normalized radiation pattern is given by

$$I(d) = \left\{ 2 J_1 \left( \frac{k\ell d}{4h} \right) / \left( \frac{k\ell d}{4h} \right) \right\}^2 \quad (5)$$

where  $J_1(\ )$  is the Bessel function of the first kind for order one,  $k$  is the electromagnetic wavenumber,  $\ell$  is the diameter of the illuminated footprint,  $d$  is the diameter of the antenna

aperture, and  $h$  is the altitude of the sensor platform. The first null in the pattern occurs when the argument of the Bessel function has the value  $1.22 \pi$ , or 3.833. That is,

$$\frac{k \ell d}{4h} = 1.22\pi \quad (6)$$

Solving for  $\ell$ ,

$$\ell = 2.44h\lambda/d \quad (7)$$

Alternate expressions for  $\ell$  based on the 3-dB width of the central lobe instead of the width between first nulls, for example, are also useful. The above equation can be solved to find the aperture diameter that is required to produce a 1 km diameter footprint on the surface as a function of altitude and radar frequency. From 824 km, an aperture 44.7 m in diameter is required at 13.5 GHz. At 36 GHz, the aperture dimension is reduced to 16.8 m. Obviously, it will be much less expensive to construct the smaller antenna in space. This fact has led to the adoption of 36 GHz as the frequency of choice for the LORA proposal for EOS. The use of the same frequency for MARA is obviously desirable as well. As part of the LORA proposal, it is planned to use the MARA to collect 36 GHz backscattering cross-section measurements of selected land surfaces for use in the design of LORA. To develop the land mode of the satellite instrument, the expected signal levels from various surface types must be known and the MARA will be the only mapping instrument available at this frequency.

#### 4.4 Mean Waveform Shape

##### 4.4.1 General

To design the data processing system for MARA, it is important to know the shape of the backscattered waveform. With the antenna design fixed (see section 4.2.1), it is possible to study this shape. Two main approaches to this task have been pursued. In the following two subsections, the results of simulations and analytical models are presented.

##### 4.4.2 Simulations

Figure 7 shows two plan views of the intercepts of the five Multibeam Mode beams with the sea surface. In the orientation shown at the top, the off-nadir beams are in the cross-track and along-track planes. This configuration produces only three along-track profiles since the fore and aft beams lie on the same ground track as the nadir beam. In the plan view at the bottom of the figure, the antenna assembly has been rotated azimuthally so that there are five non-overlapping profiles uniformly spaced across the swath. In the simulations described in this section, only the first configuration is dealt with because the effect of aircraft pitch and roll on the resultant altimeter waveforms is much easier to compute for this case.

Figure 8 is drawn to scale and shows the MARA geometry for the dielectric lens 3-dB beamwidth and an altitude of 3048 m. The sea state is represented by a 5.2 m peak-to-trough sinusoid of 202 m wavelength which is traveling from left to right. This wave height and wavelength are typical of the fully-developed sea state for a 15 m/s wind. Figures 9 and 10 are also drawn in proper proportion and show blowups of the nadir and right-hand beams in Figure 8. The abscissa

Figure 7. Backscattering vectors showing the illumination geometries for the two orientations of the Multibeam Mode antenna assembly.

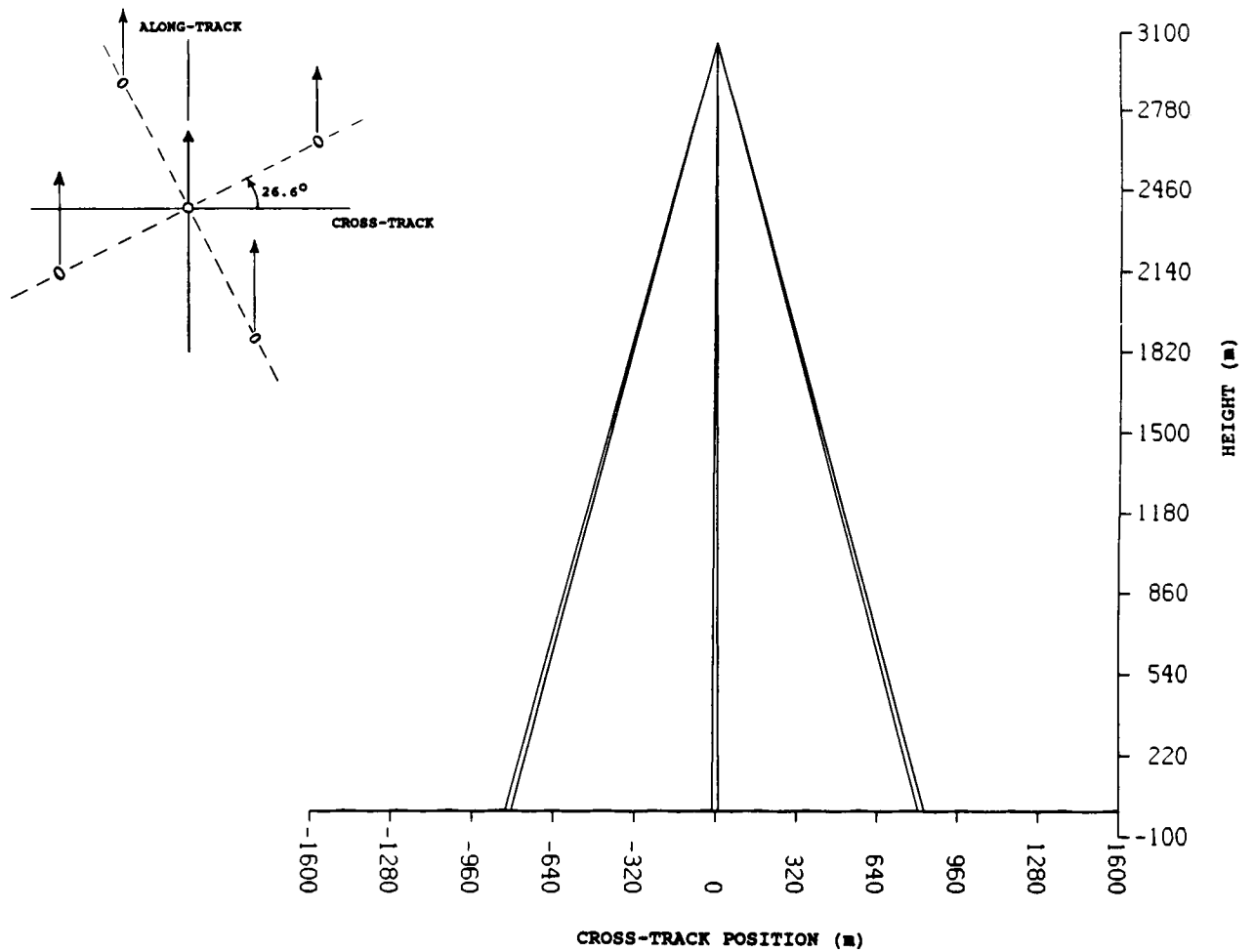
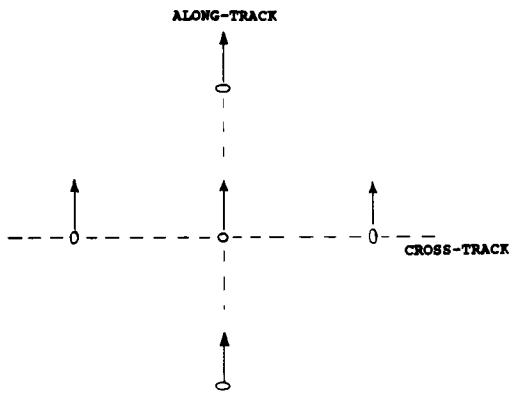


Figure 8. Scaled illustration of the nadir and two 15 degree off-nadir Multibeam Mode beams from a platform at 10,000 ft altitude.

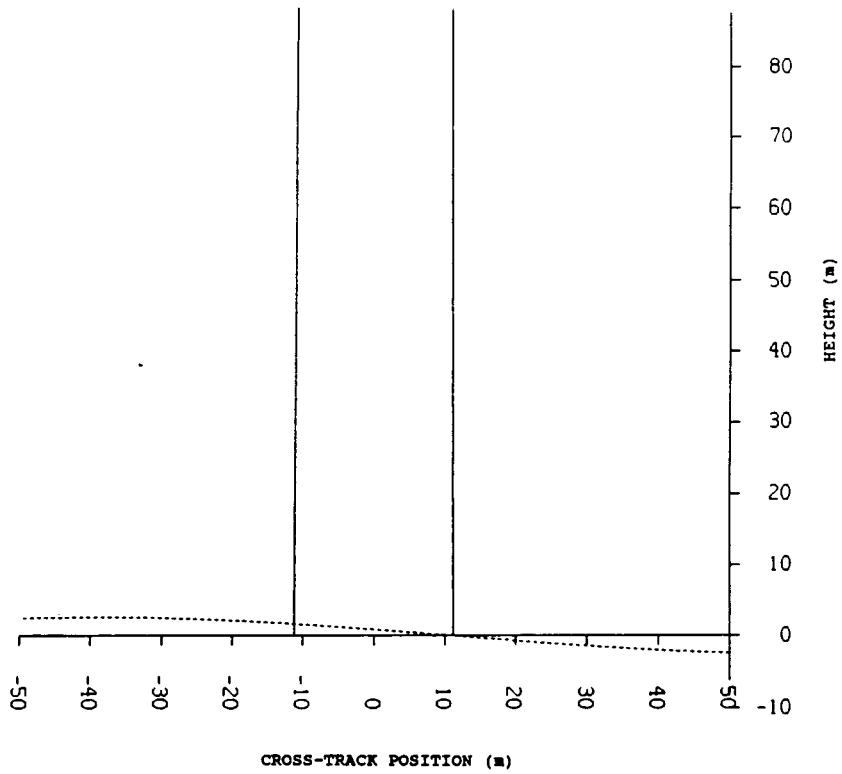


Figure 9. Illumination geometry for the nadir beam and a fully developed sea resulting from a 15 m/s wind field.

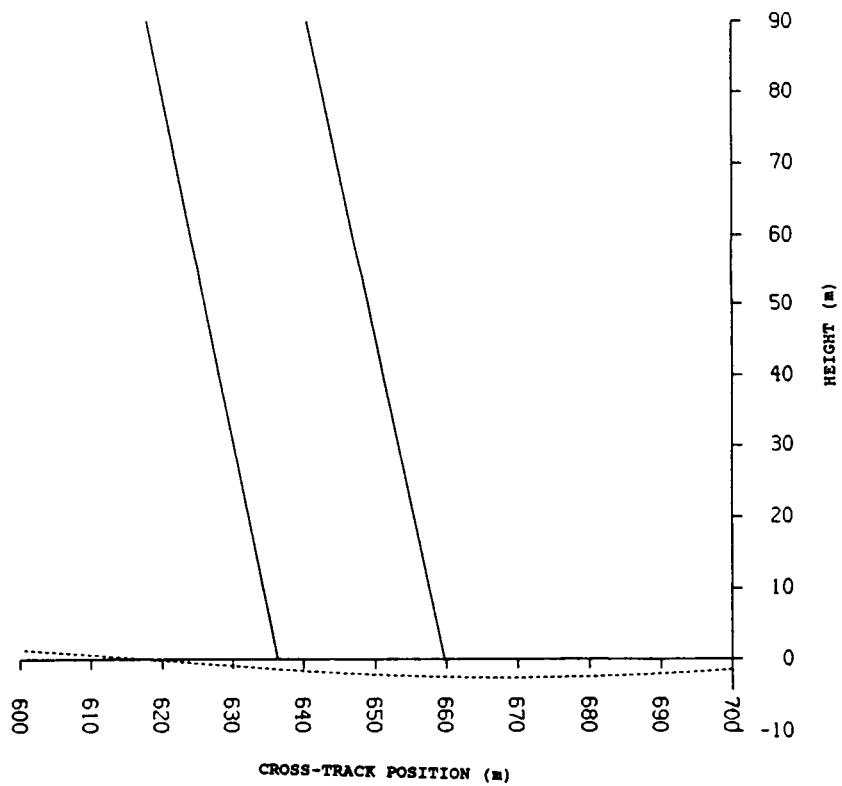


Figure 10. Illumination geometry for the 12 degree off-nadir beam and a fully developed sea resulting from a 15 m/s wind field.

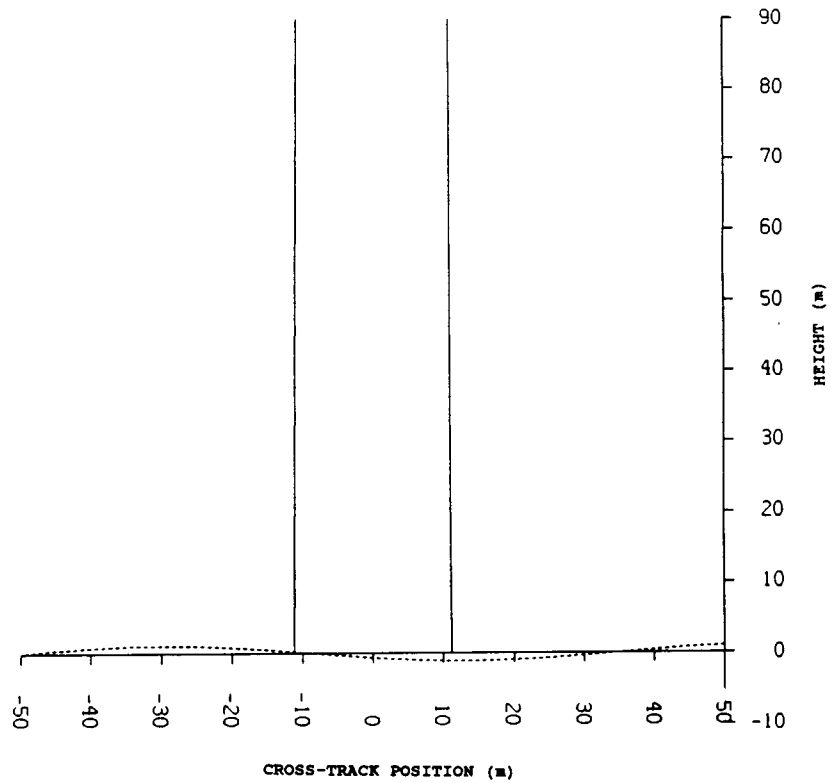


Figure 11. Illumination geometry for the nadir beam and a fully developed sea resulting from a 10 m/s wind field.

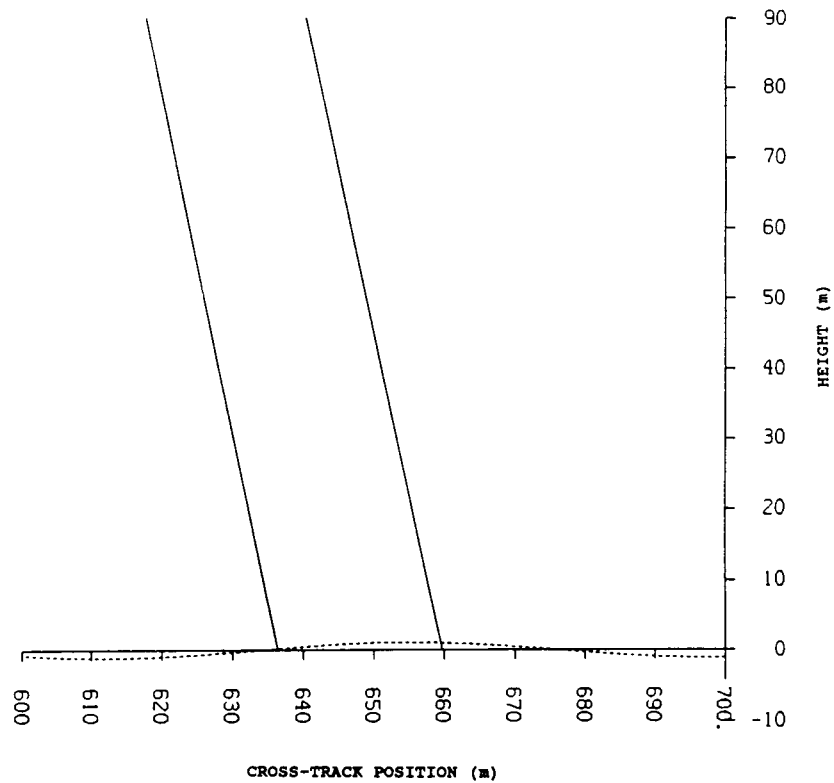


Figure 12. Illumination geometry for the 12 degree off-nadir beam and a fully developed sea resulting from a 10 m/s wind field.

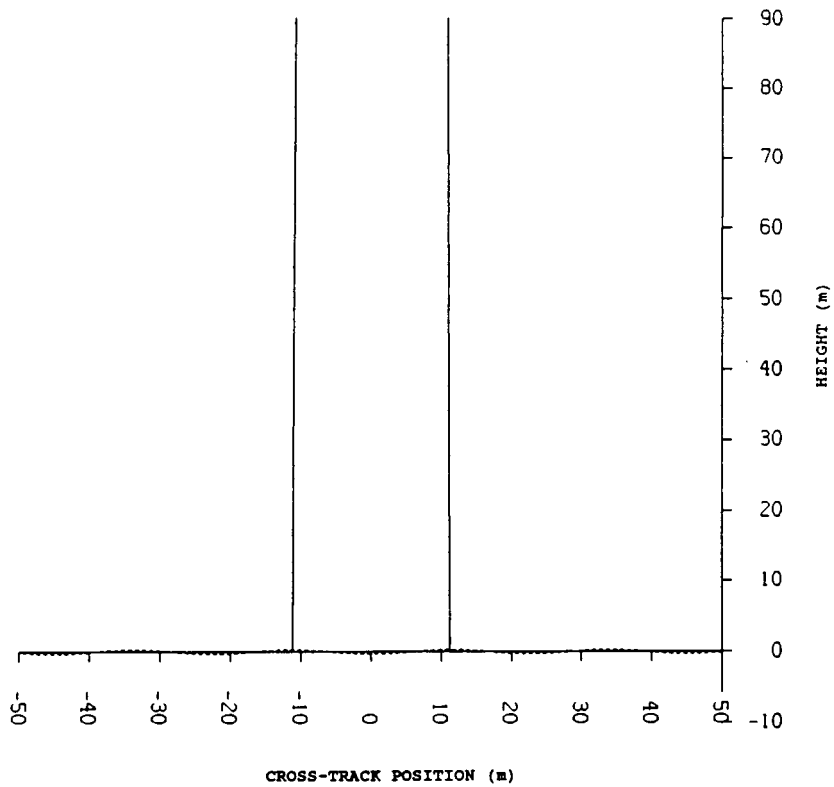


Figure 13. Illumination geometry for the nadir beam and a fully developed sea resulting from a 5 m/s wind field.

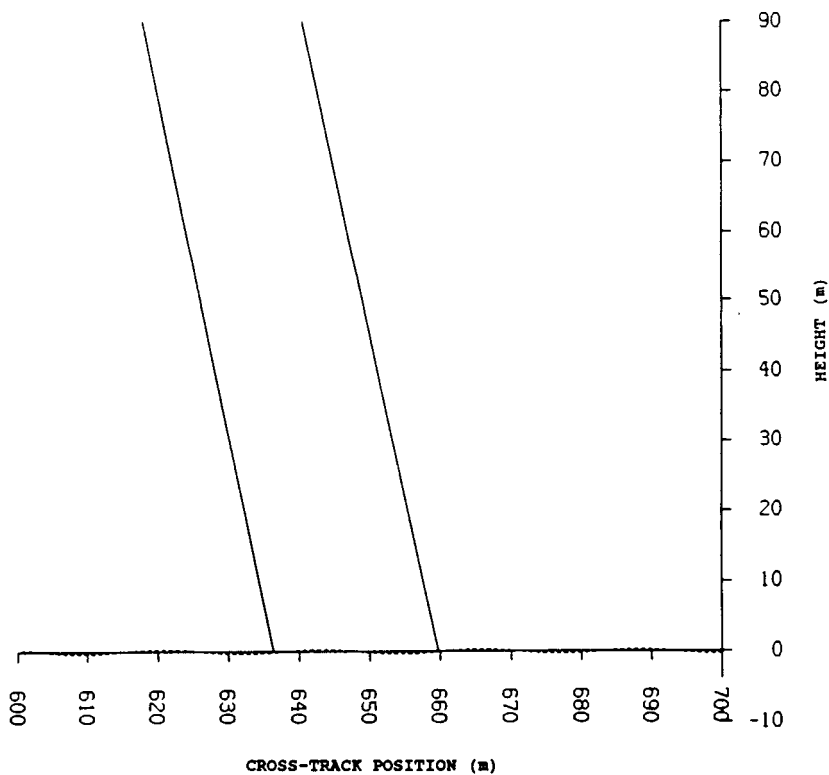


Figure 14. Illumination geometry for the 12 degree off-nadir beam and a fully developed sea resulting from a 5 m/s wind field.

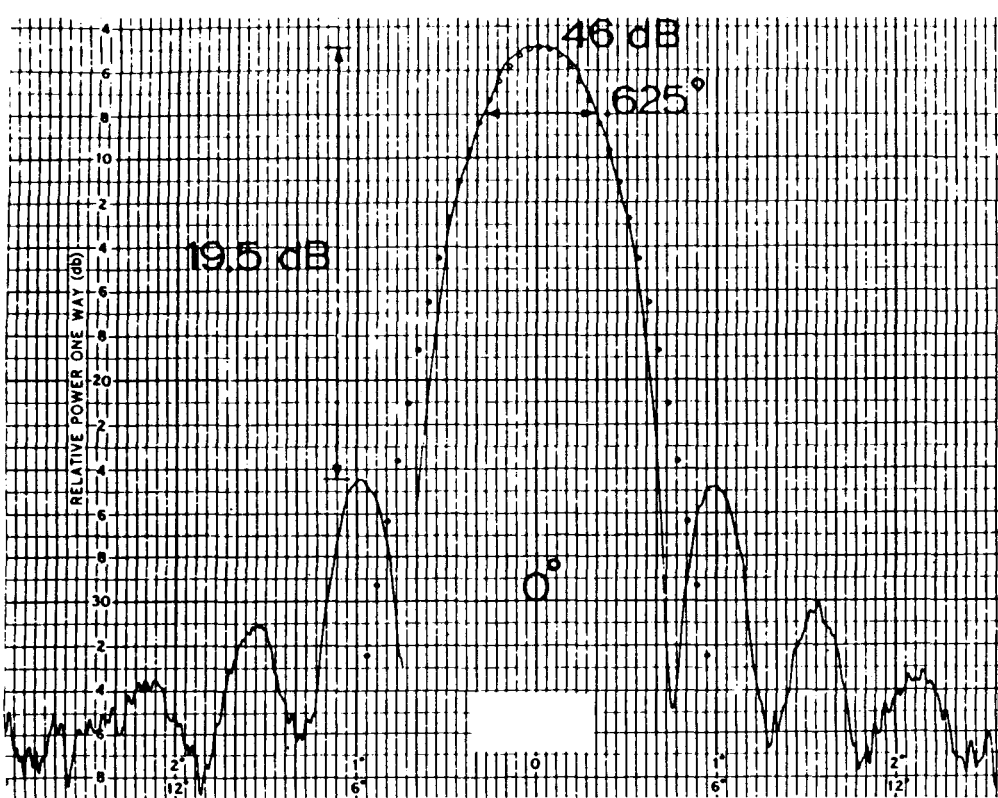


Figure 15. Measured (solid) and fitted Gaussian (dotted) MARA lens antenna patterns for the nadir beam.

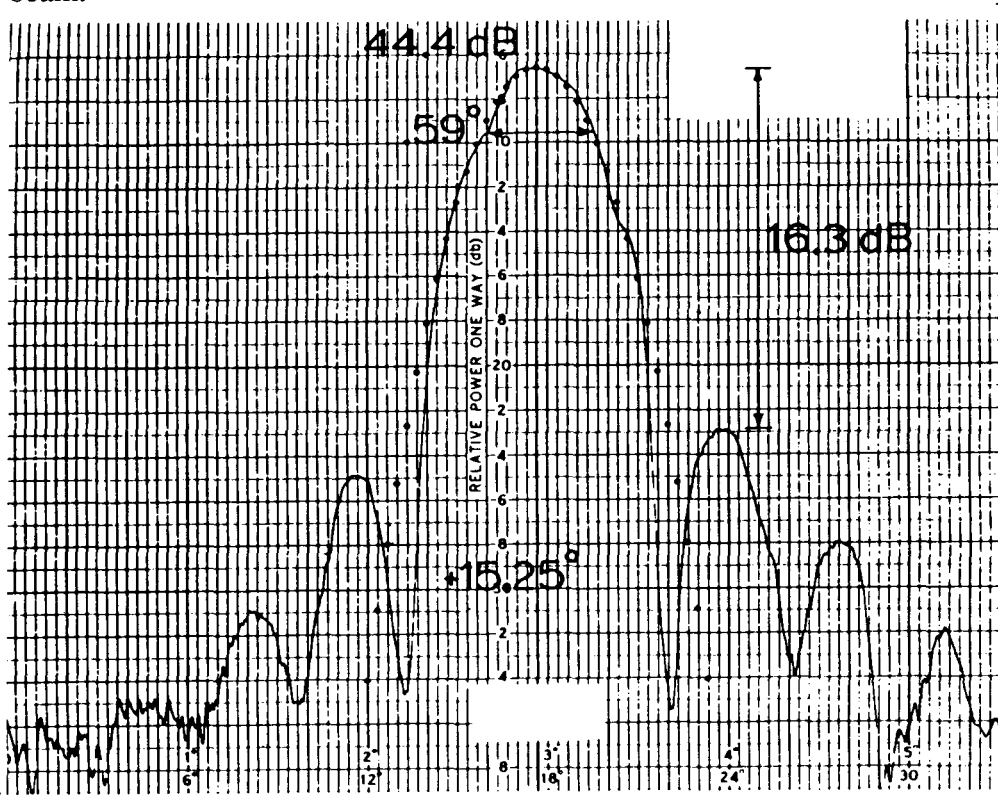


Figure 16. Measured (solid) and fitted Gaussian (dotted) MARA lens antenna patterns for 12 degrees off-nadir.

is mean sea level (MSL) and the instantaneous position of the sea surface is indicated by the dashed line. It is apparent that the sea surface within the footprint could be approximated by a tilted plane whose mean elevation can deviate from MSL. Figures 11 and 12 show the same regions as Figures 9 and 10 but for a 2.2 m crest-to-trough sinusoid whose wavelength is 86 m. This corresponds to the fully-developed sea state for a 10 m/s wind. Even here the flat plane approximation is not too bad. The fully-developed sea state associated with a 5 m/s wind would have a dominant wavelength of only 23 m and the MARA footprint would always contain both crest and trough, as indicated in Figures 13 and 14. For wavelengths this size or shorter, there is virtually no deviation of the average surface within a footprint.

In Figures 15 and 16 the measured antenna patterns (solid curves, from Parsons and Miller, 1988) for nadir and 15 degrees off-nadir, respectively, are compared with a .625 degree 3-dB width Gaussian model (circles). This model was used to approximate the antenna pattern for the following discussion. The agreement is excellent down to 9 dB below the peak. Beyond that, the Gaussian model is somewhat broader than the main lobe of the measured pattern, and it of course does not exhibit the sidelobe structure of the actual pattern.

Using this Gaussian model, it is easy to compute the variation in the gain of the antenna pattern with range as it intercepts the sea surface. This simple approach should give a reasonable estimate of the range extent of the waveform. Figure 17 shows the returned waveforms for a flat sea and off-nadir incidence angles of 9 degrees through 15 degrees. For a maximum off-nadir angle of 12 degrees, this range of angles represents the variation that would result from a -3 to +3 degree variation in aircraft roll angle. The returns have been normalized to their peak values and range is measured relative to the range to the peak. The width varies nearly linearly with the incidence angle. The dashed reference line at the -16 dB level indicates the highest level of the sidelobes of the measured antenna patterns. Figure 18 shows that this range of roll angle includes the normal excursions from level flight encountered for the Wallops P-3. These data were taken by the aircraft's Inertial Navigation System during past experiments.

It is also of interest to determine the effects of typical sea surface slopes on the waveform shape. Consider a sinusoidal wave of amplitude  $A$  and wavelength  $\lambda$ . If  $z$  is the vertical coordinate and  $x$  is the horizontal, then the instantaneous surface height variation is given by

$$z = A \sin(2\pi x/\lambda) \quad (8)$$

and the sea surface slope by

$$\frac{dz}{dx} = \frac{2\pi A}{\lambda} \cos(2\pi x/\lambda) \quad (9)$$

The maximum slope is  $2A\pi/\lambda$ . If  $2A$  is the significant wave height (SWH) and  $\Gamma$  is defined as the ratio of the dominant wavelength to the SWH, then the typical maximum slope can be represented as  $\pi/\Gamma$ . Figure 19 is a plot (from Walsh *et al.*, 1987) of SWH and  $\Gamma$  versus fetch for various windspeeds and durations. It indicates that  $\Gamma$  will not be less than 30 if one considers windspeeds less than or equal to 15 m/s and durations greater than 2 hours. If  $\Gamma$  is 30, the maximum slope is 6 degrees. Since Figures 9 through 12 indicated that the longer ocean wavelengths appear as tilting planes within the beam, the tangent plane approximation will be used to examine the effect of waves on the waveform shape. The value of  $\Gamma$  is more likely to be

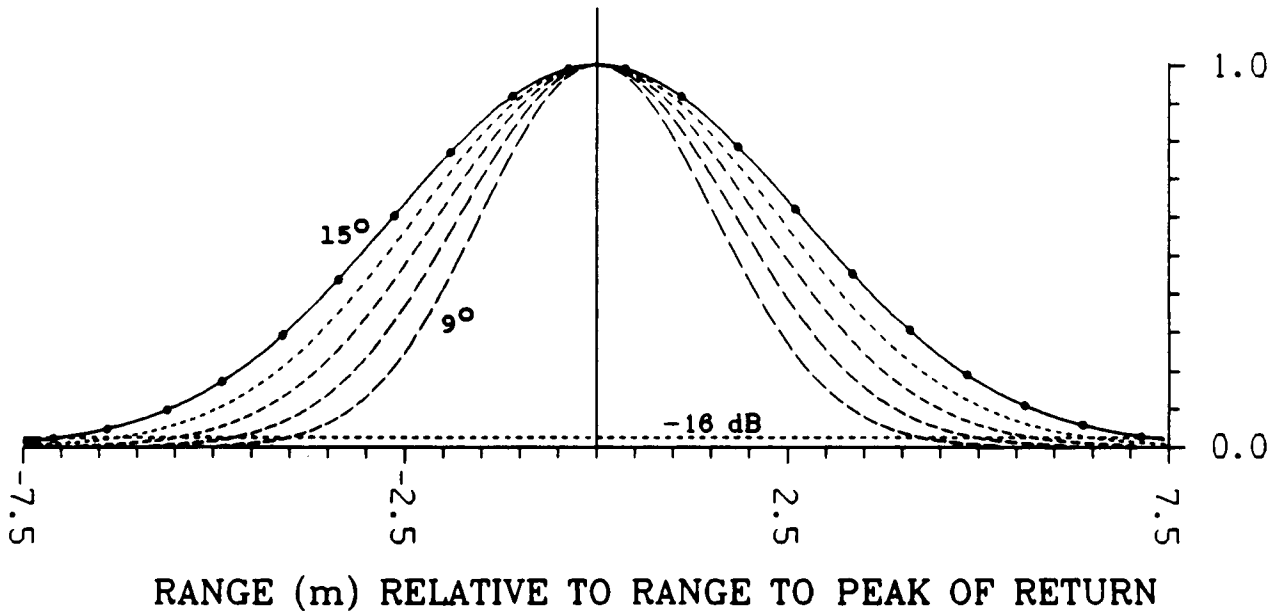


Figure 17. Simulated backscattered waveforms for the 12 degree off-nadir beam and platform roll angles of -3 to +3 degrees.

60 or 100 than 30. Therefore, the MARA will more typically be encountering slopes in the  $\pm 3$  degree range than  $\pm 6$  degrees. Figure 20 shows the waveforms for cross-track sea surface slopes between -3 and +3 degrees for the beam which is 12 degrees off-nadir to the right. One should note that these shapes are virtually identical to those of Figure 17. This is because the shape is basically determined by the angle between the beam and the surface. It does not matter whether that angle is the result of aircraft roll or surface slope or some combination of the two effects.

Figure 21 indicates the variation of the antenna pattern with range for the MARA nadir beam for the same five surface slopes as in Figure 20. Although curves for five slopes were computed and plotted, only three are seen because the effect of positive and negative slopes is the same at nadir. The curve for zero sea surface slope in Figure 21 is only a fraction of a ns in width. This is because the curves are not truly returned waveforms. They do not include the finite width of the transmitted pulse. The requirement to convolve the antenna gain shapes in this section with the transmitted pulseshape is discussed in the next section and the convolution is implemented in 4.5.

#### 4.4.3 Analytical Models

As discussed by Hayne (1980), the general square-law detected waveform  $W(t)$  is given analytically by the convolution

$$W(t) = P_{FS}(t) * q_s(t) * s_r(t) \quad (10)$$

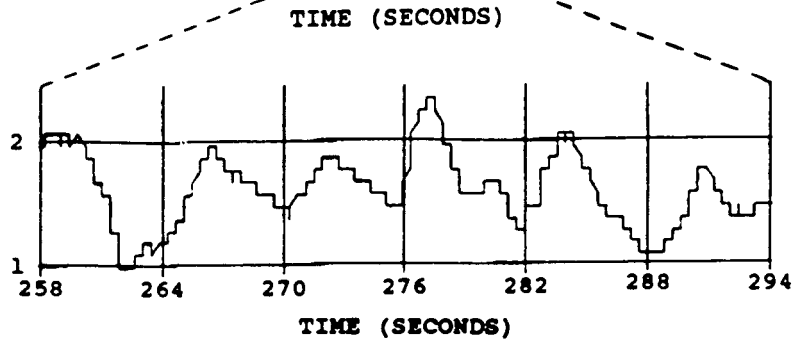
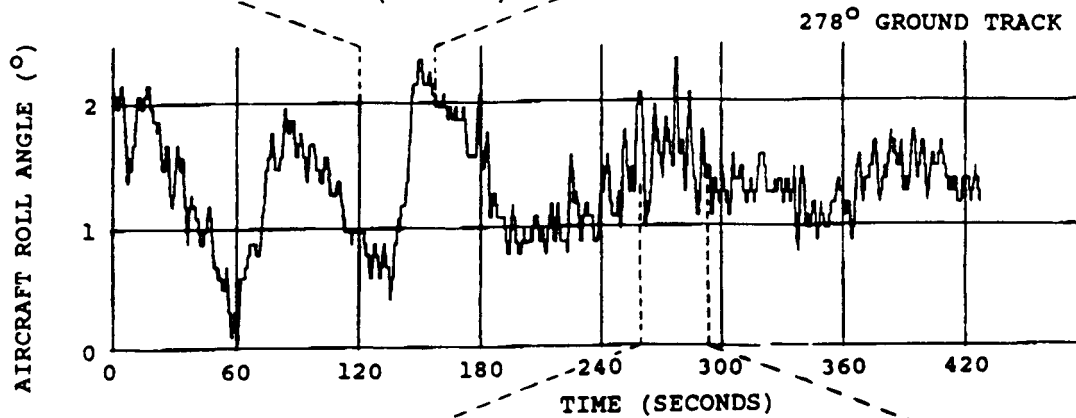
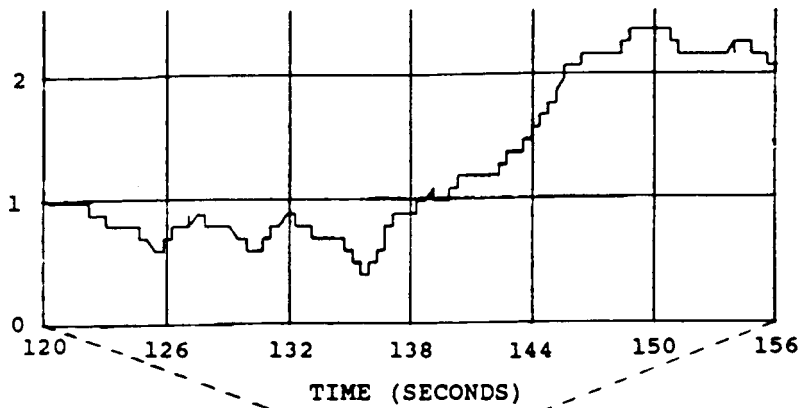
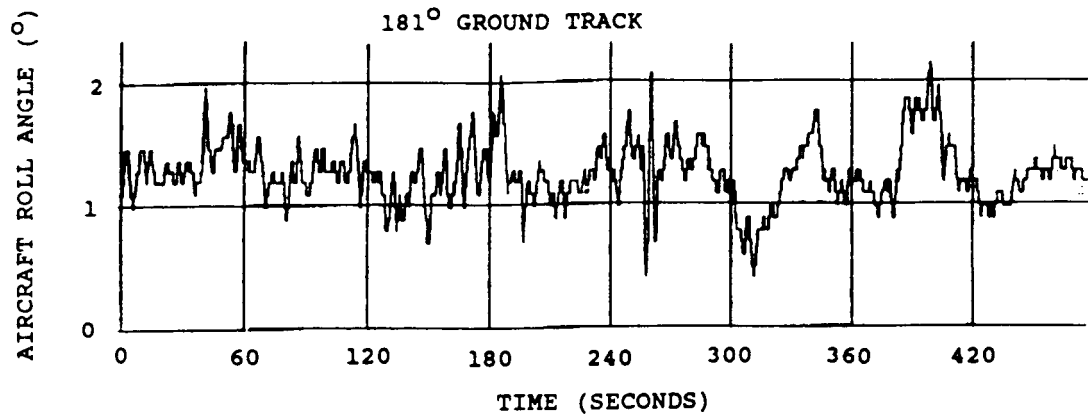


Figure 18. Aircraft roll angle data from NASA P-3 research aircraft flights along south and west groundtracks. Two expanded sections of the records for the latter show that even rapidly changing roll angle is slowly varying when sampled at a 20/s rate.

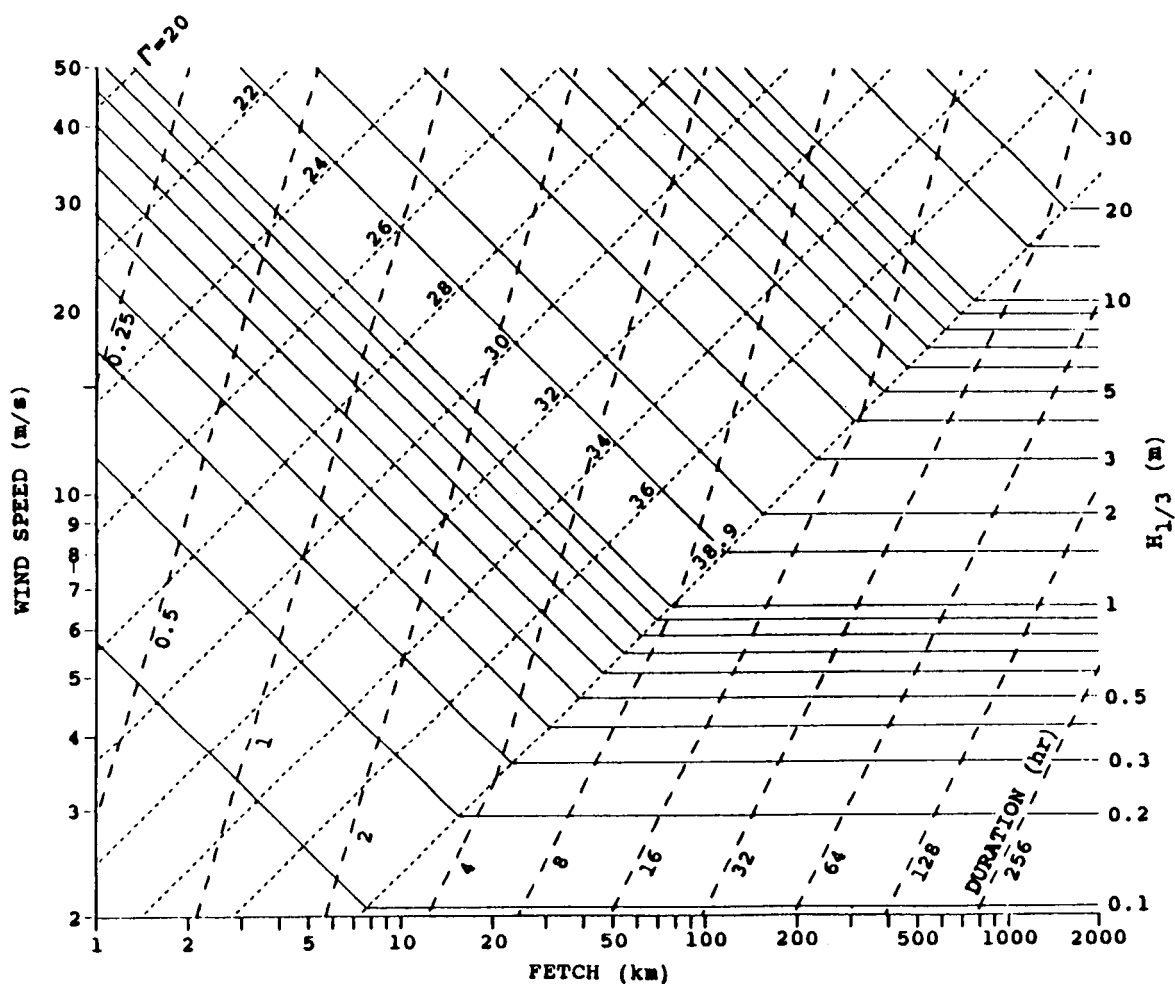


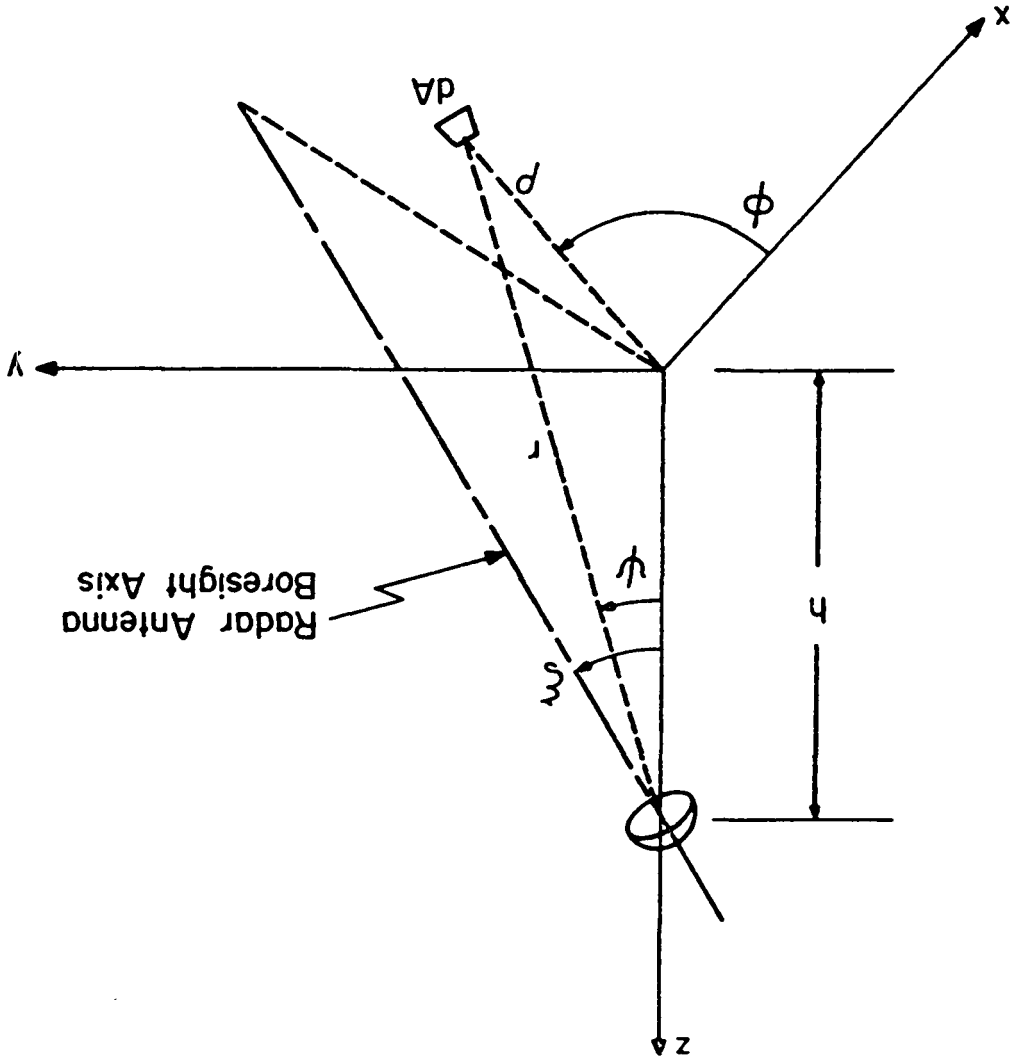
Figure 19. Nominal variation of significant wave height and the wave slope parameter,  $\Gamma$ , versus fetch at various wind speeds and durations (from Walsh et al, 1987).

where  $P_{FS}(t)$  is the average flat surface impulse response,  $q_s(t)$  is related to the surface elevation probability density of scattering facets, and  $s_r(t)$  is the radar system point-target response. In general, the first term accounts for the backscattering cross-section per unit area of the target,  $\sigma_o$ , the antenna gain pattern,  $G(\theta)$ , the radar wavelength,  $\lambda$ , atmospheric losses,  $L$ , the pointing angle relative to nadir,  $\xi$ , and the range from the radar to the surface. The surface elevation probability density incorporates the rough surface scattering properties of the surface, and the point-target response models the finite pulsewidth of the transmitted pulse. Mathematical formulas for  $P_{FS}(t)$  were developed by Brown (1977). The full expression was found to be

$$P_{FS}(\tau) = \frac{G_o^2 \lambda^2 c \sigma_o(\psi)}{4(4\pi)^2 L h^3} \exp\left\{-\frac{4}{\gamma} \sin^2 \xi - \frac{4c\tau}{\gamma h} \cos 2\xi\right\} \quad (11)$$

$$* \sum_{n=0}^{\infty} \left\{ \frac{(-1)^n \Gamma(n+0.5)}{\sqrt{\pi} \Gamma(n+1)} \right\} \left( \sqrt{\frac{c\tau}{h}} \tan \xi \right)^n I_n \left( \frac{4}{\gamma} \sqrt{\frac{c\tau}{h}} \sin 2\xi \right)$$

Figure 22. Radar viewing geometry (from Brown, 1988).



so that  $G_0$  is the boresight gain and  $\gamma$  determines the beamwidth. The  $\Gamma(\ )$  are gamma functions and the  $I_n(\ )$  are modified Bessel functions of order  $n$ . For conventional spaceborne short pulse radar altimeters, Brown (1977) shows that the above expression can be reduced in complexity by retaining only the  $n=0$  term. Using this simplified expression, Hayne (1980) performs the convolution of the flat surface impulse response with near-Gaussian models of  $q_r(t)$  and  $s_r(t)$ . Hayne represents the non-Gaussian aspects of these two functions with both 2 and 4 term expansions of a general Gram-Charlier series. The resulting waveforms display the expected shape of the waveform as shown in Figure 23.

$$G(\theta) = G_0 \exp \left( -\frac{\gamma}{2} \sin^2 \theta \right) \quad (12)$$

where the geometrical parameters are defined in Figure 22.  $G_0$  and  $\gamma$  are related to the antenna pattern by

Figure 21. Simulated backscattered waveforms for the nadir beam and sea surface slopes of -3 to +3 degrees.

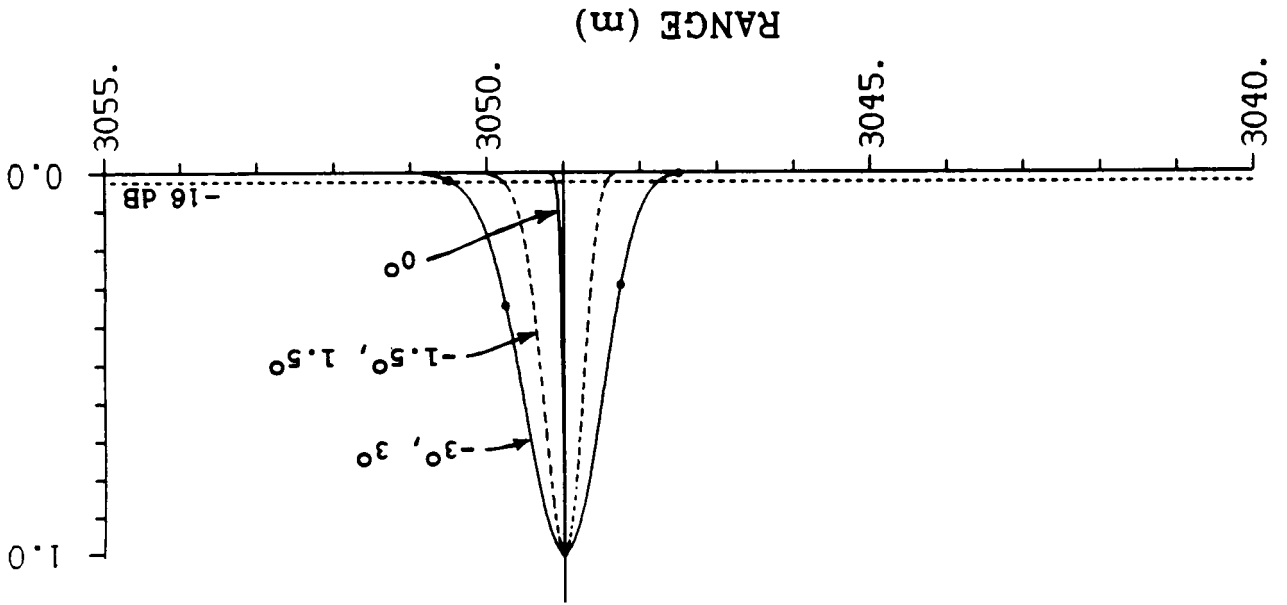
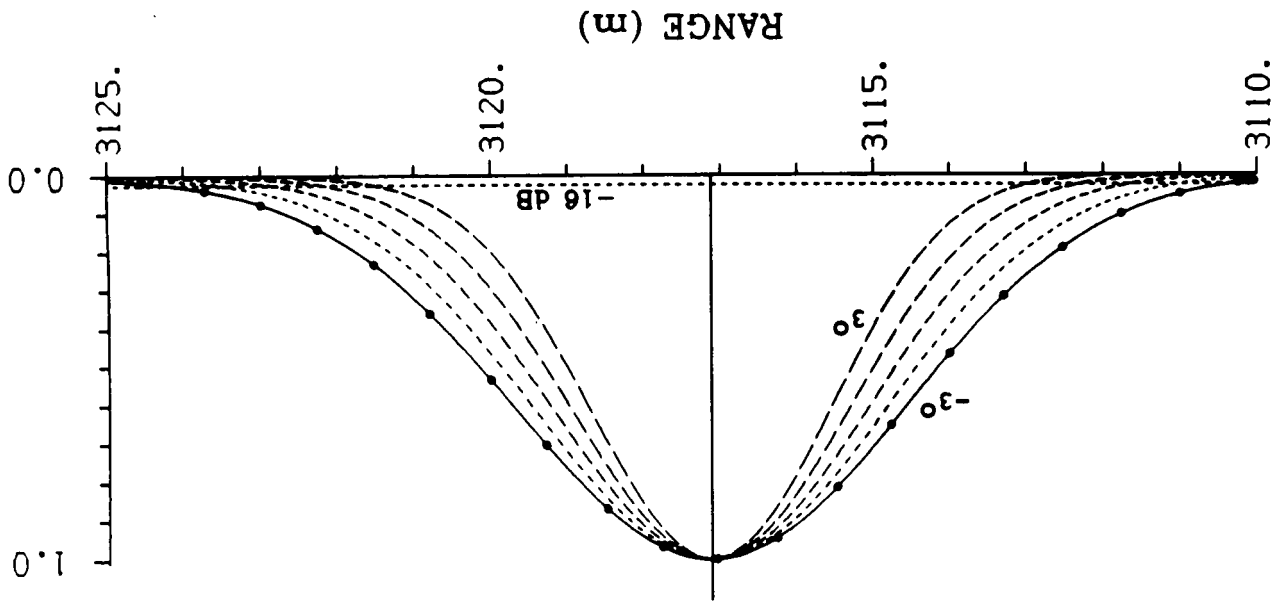


Figure 20. Simulated backscattered waveforms for the 12 degree off-nadir beam and sea surface slopes of -3 to +3 degrees.



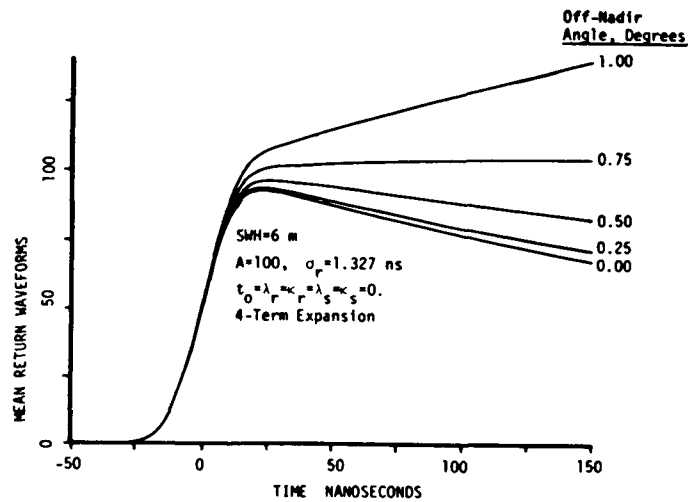


Figure 23. Modeled SEASAT radar altimeter waveforms showing the effects of attitude angle on pulse-limited altimeter performance (from Hayne, 1980).

For the wide swath altimetry being addressed in this document, the inclusion of only the  $n=0$  term is not appropriate. For small beamwidths,  $\gamma$  becomes small while  $\xi$  may be as large as 12 degrees. Then, the arguments of the Bessel functions in the equation for  $P_{FS}(t)$  become very large. The computational difficulties created therein are discussed by Brown (1989). Alternate computational techniques are briefly described by Brown (1989); work is continuing through NASA Grant NAG5-648 with the Virginia Polytechnic Institute and State University to refine the techniques for computing  $P_{FS}(t)$ . When ready, it will be possible to extend the work of Hayne to off-nadir, beam-limited radars. In essence, for the off-nadir geometry the flat surface impulse response should take on the shape of a Gaussian function because of the geometrical broadening of the antenna pattern; the large width of the off-nadir  $P_{FS}(t)$  function should then predominate over the point-target response and the scattering probability density function resulting in the near Gaussian simulation results in the preceding section. The use of an analytical model for the waveform is required to complete the studies leading to the selection of the MARA operating parameters which are described in this document. It will be important to verify the selection of the system pulsewidth, transmitted power, and waveform sampling strategy as determined through simulations. The completed analytical model should have the capability to determine the effects of platform attitude uncertainties on system performance. And, the waveform model may be helpful in analytical estimates of the system's tracking performance using various tracking algorithms.

#### 4.5 The Noisy Waveform

In this section, the shape of the returned waveform will be simulated more accurately by incorporating the effects of Rayleigh fading and by convolving the transmitted pulse with the average flat surface impulse response and the surface scattering facets probability density. That is, the noise of the scattering process will be added to the simulated flat surface impulse response characteristics such as shown in Figure 20 and the resultant will be convolved with a projected transmitted pulse shape.

To simulate the noise of the scattering process, we use Rayleigh fading statistics. There has been a large volume of literature dedicated to the statistical properties of the randomly-rough sea surface. Barrick and Peak (1968) and Skolnik (1970) are good references that characterize the surface as a collection of incoherent, discrete scatterers. The scattering statistical properties are generally assumed to be Rayleigh and that is the assumption invoked here. Pierson and Mehr (1972), Miller and Hayne (1972), Berger (1972), and Barrick (1972) have used this premise to study the performance of previous conventional radar altimeter systems. The properties of the Rayleigh distribution are readily found in Papoulis (1965). The scattering process will be modeled in the following way. The radar's signal is scattered by many discrete reflective facets having the proper orientation within the instrument's field-of-view. Representing each facet's effect on the total signal return as a phasor as shown in Figure 24, the signal due to the  $i$ th scatterer is

$$V_i = V_i e^{j(\omega t_i + \theta_i)} \triangleq V_i e^{j\phi_i} \quad (13)$$

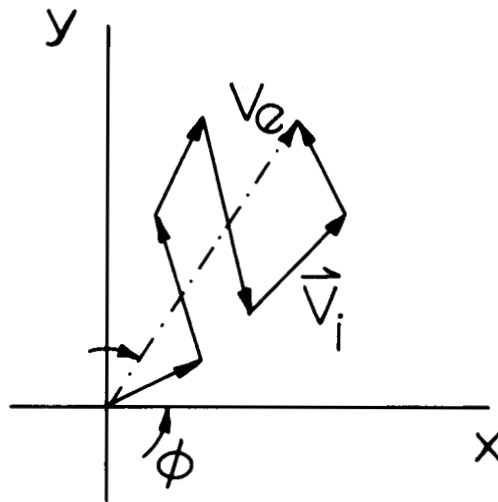


Figure 24. Phasor addition for a random-walk process.

Then the instantaneous signal from all illuminated scatterers is

$$\vec{V} = \sum_{i=1}^{N_s} V_i e^{j\phi_i} \quad (14)$$

which can be expressed as

$$\vec{V} = V_e e^{j\phi} \quad (15)$$

From the figure, it is clear that

$$V_x = V_e \cos\phi = \sum_{i=1}^{N_s} V_i \cos\phi_i$$

$$V_y = V_e \sin\phi = \sum_{i=1}^{N_s} V_i \sin\phi_i$$

If  $N_s$  is large enough, then we can assume that  $V_x$  and  $V_y$  are normally distributed (using the Central Limit Theorem) and their means are given by

$$\langle V_x \rangle = \sum_{i=1}^{N_s} \langle V_i \cos\phi_i \rangle$$

$$\langle V_y \rangle = \sum_{i=1}^{N_s} \langle V_i \sin\phi_i \rangle$$

Also, assume that  $V_i$  and  $\phi_i$  are independent random variables and that the  $\phi_i$  are uniformly distributed over  $[0, 2\pi]$ . Then,

$$\langle V_x \rangle = \sum_{i=1}^{N_s} \left\{ \langle V_i \rangle * \frac{1}{2\pi} \int_0^{2\pi} \cos\phi_i d\phi \right\} = 0$$

$$\langle V_y \rangle = 0$$

$$\langle V_x V_y \rangle = 0$$

Therefore,  $V_x$  and  $V_y$  are decorrelated which implies independence for normally distributed variables. For normally distributed variables that are independent, their probability distribution can be described by a jointly normal probability density function (pdf). Thus,

$$p(V_x, V_y) = \frac{1}{2\pi\sigma^2} e^{-(V_x^2 + V_y^2)/2\sigma^2}$$

where  $\sigma$  is the standard deviation of  $V_x$  and  $V_y$ . This density function can also be expressed in terms of the envelope signal,  $V_e$ . Converting to polar coordinates,

$$V_e^2 = V_x^2 + V_y^2$$

$$\phi = \tan^{-1}(V_x/V_y)$$

$$p(V_e, \phi) = \frac{V_e}{2\pi\sigma^2} e^{-V_e^2/2\sigma^2}$$

This can also be expressed as

$$p(\phi) = \int_0^{\infty} p(V_e, \phi) dV_e = \frac{1}{2\pi}$$

$$p(V_e) = \int_0^{2\pi} p(V_e, \phi) d\phi = \frac{V_e}{\sigma^2} e^{-V_e^2/2\sigma^2} = \text{Rayleigh distribution}$$

From Papoulis (1965),

$$E \{V_e\} = \bar{V}_e = \sigma \sqrt{\frac{\pi}{2}} \quad (22)$$

$$E \{V_e^2\} = \bar{V}_e^2 = 2\sigma^2$$

Most radars use square-law detectors, so the distribution of interest is the power density given by

$$P = V_e^2 \quad (23)$$

$$p(P) = \frac{1}{2\sigma^2} e^{-P/2\sigma^2} dP$$

This is an exponential distribution which has the property that

$$\bar{P} = 2\sigma^2 \quad (24)$$

$$p(P) = \frac{1}{\bar{P}} e^{-P/\bar{P}}$$

This distribution describes the fluctuations in the return waveform from pulse-to-pulse at a given mean power level. It has the characteristic that its change with power level is set entirely by the standard deviation,  $\sigma$ , which is the standard deviation of the  $V_x$  and  $V_y$  Gaussian random variables. By adjusting  $\sigma$ , it is possible to change the mean power to a particular value, such as the level at a particular range for one of the curves in Figure 20. Figures 25 and 26 demonstrate the model. In the first figure, a Gaussian random variable's distribution is shown along with the Gaussian curve that best fits the simulation results. The average is .002636 which is close to the expected zero mean, and the standard deviation is .09313. From the  $\chi^2$  test, the value of  $\chi^2$  is 19.8275 with 21 degrees of freedom for a significance level of .5322. Using the model above, the Gaussian distribution is used to model  $V_x$  and  $V_y$  from which the envelope signal  $V_e$  is formed. Then the power is obtained by squaring this signal. Figure 26 shows the resultant exponential distribution for 1000 power values. An exponential distribution model has been fitted to the simulation results. The standard deviation of the Gaussian random variables has been adjusted so that the mean of the exponential distribution is 1. The computed mean is actually 1.0061 and the standard deviation of the pdf is .9618. From Papoulis (1965) it is known that the mean and standard deviation of an exponential pdf are identical. The  $\chi$  value is 14.4186 with 15 degrees of freedom, for a significance level of .494.

This model was used in a three-dimensional numerical integration of the antenna pattern over the illuminated footprint. First, the sea surface was broken down into areas identified by subdividing the antenna pattern into .003 degree increments along one axis by .003 degree increments in the orthogonal direction. This subdivision identified a 401 by 401 grid of points on the sea surface spaced approximately .167 m by .167 m. The range to each point on the surface was computed and the appropriate bin identified in a return waveform histogram. The histogram had 151 bins from about 3108 m range to 3126 m in .12 m increments. The power in the appropriate bin was incremented by the corresponding two-way antenna pattern gain at that angle. In that way, the return waveform was built up by adding all the individual contributions from the grid of surface

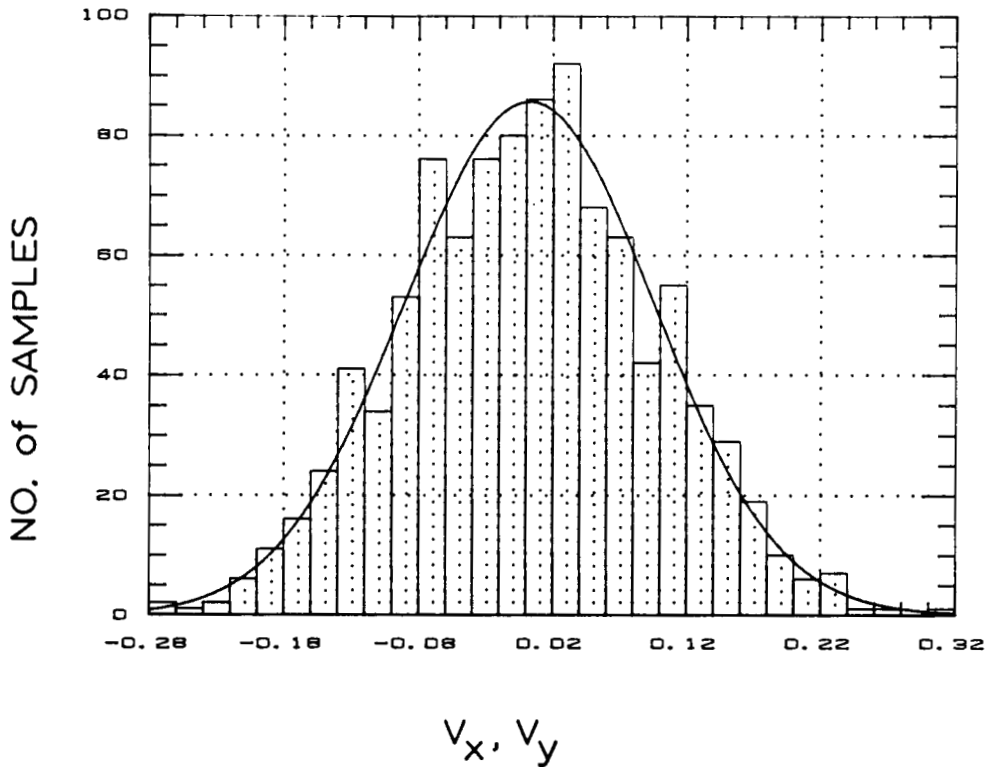


Figure 25. The distribution of 1000 averaged values, each the result of 1000 random variables uniformly occurring in the range between  $-.5$  and  $+.5$ .

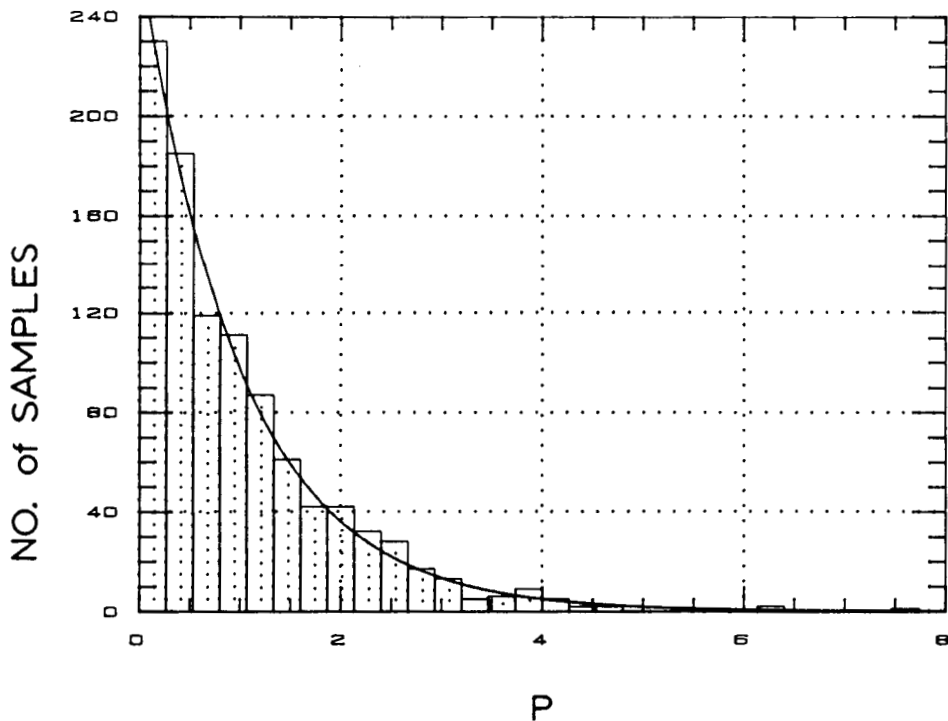


Figure 26. The distribution of 1000 values of  $P$ , each computed using (20a) and (23a) and pairs of zero mean Gaussian distributed variables as  $V_x$  and  $V_y$ . Using (24), the standard deviation of the Gaussian variable distributions has been adjusted so that the mean of this exponential distribution is 1.

areas. The results for the right-hand cross-track footprint in the Multibeam Mode are shown in Figure 27 and they are almost identical to the one-dimensional model results in Figure 20. The ripple is the result of the finite number of points in the numerical integration. The nominal transmitted pulse shape is taken to be the trapezoid shown in Figure 28, and this shape has been convolved with the three-dimensional model results before being shown in Figure 27. The half-power width is assumed to be 5 ns and this is responsible for the slight broadening of the waveforms in Figure 27 as compared to 20. The results for the cross-track footprint and sea surface slopes (or equivalently aircraft pitch angles) in the along-track direction are shown in Figure 29. As is apparent, there is virtually no deviation of the return waveforms from that for a horizontal surface. Figure 30 contains the nadir waveforms. For this case, the return waveform for the 0 degree slope case essentially reproduces the pulse shape, and there is very little difference between the shapes for slopes between + and - 1.5 degrees.

The Rayleigh fading noise was then added to the model and these results are plotted in Figure 31. For a nominal 12 degree off-nadir viewing angle, the actual slopes that could be illuminated from a combination of aircraft roll and sea surface slopes could range from a minimum of 3 degrees to a maximum of 21 degrees. The mean return from the model for these angles and the averaged fluctuating return are plotted for 7 different incidence angles in the figure. The abscissa is range. These waveforms have a great range extent. To track the surface with precision will require that the location of this waveform in range be known extremely well. The centroid, or some other statistical descriptor of the shape, may be useful in monitoring the change in location of the waveform. To know the centroid as well as possible, all of the information contained in the waveform must be used to advantage. That means that the number of independent samples used to measure the waveform shape must be maximized. Rayleigh fading is correlated over a distance equal to the pulse extent. Therefore, sampling more often than the range extent of the pulse width does not add information. To maximize the information content, the pulse width must be narrowed.

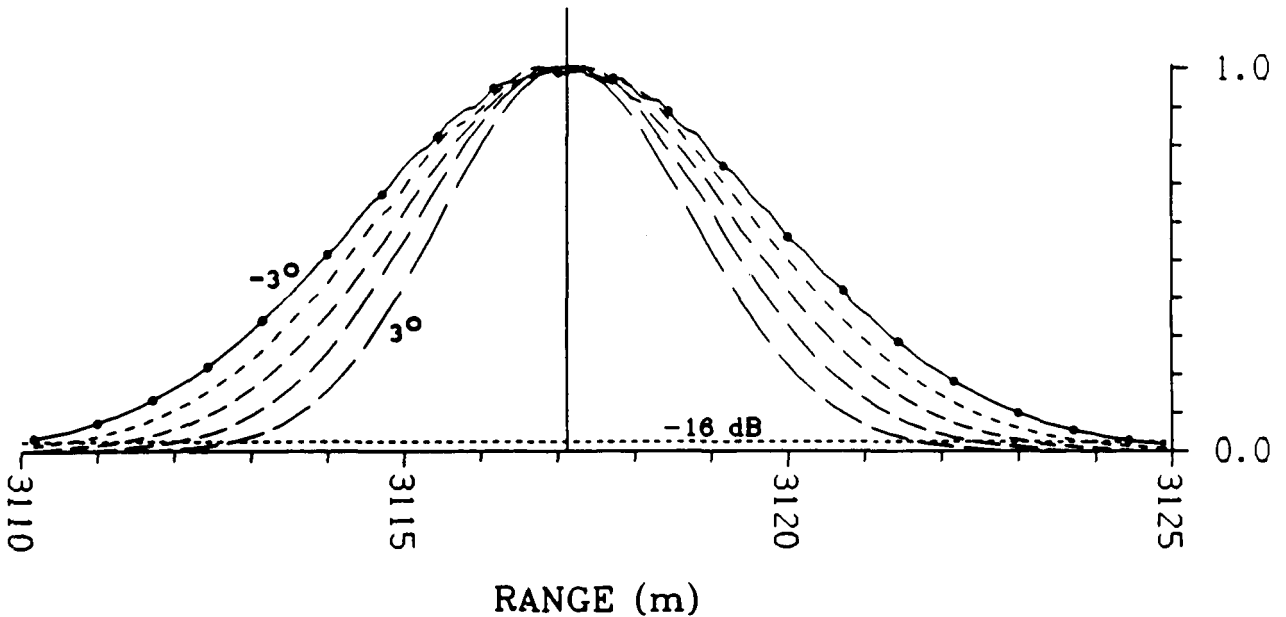


Figure 27. Simulated backscattered waveforms for the 12 degree off-nadir beam and combined roll and sea surface slope effects between -3 and +3 degrees. The effects of the 5 ns transmitted pulse shape are included.

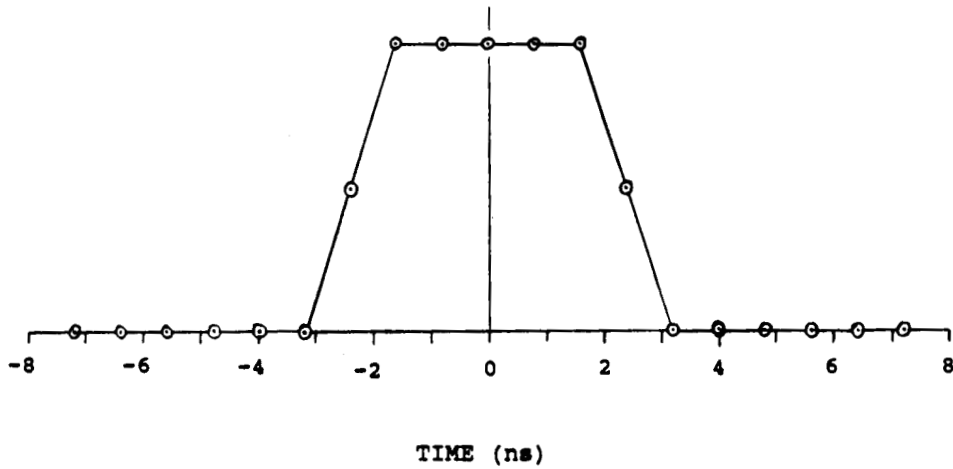


Figure 28. The assumed shape of the 5 ns transmitted pulse.

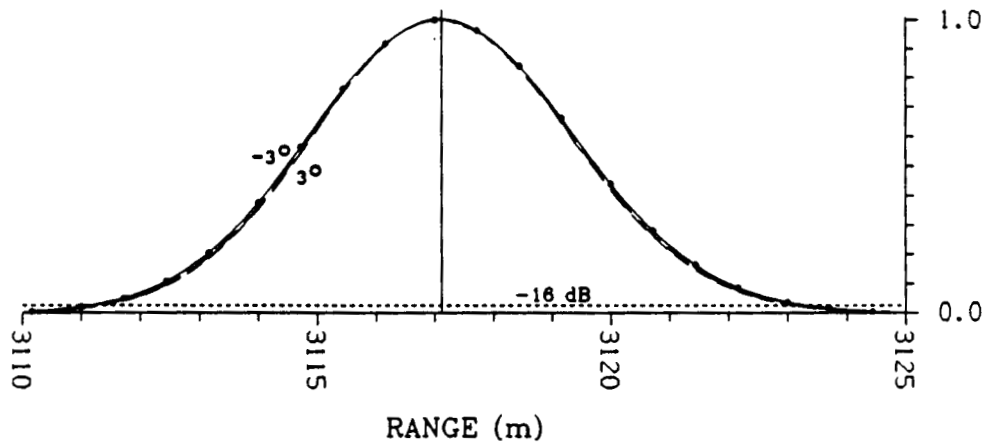


Figure 29. Simulated waveform shapes for the 12 degree cross-track footprint and combined aircraft pitch and sea surface along-track slope effects. The transmitted pulse shape effect is included.

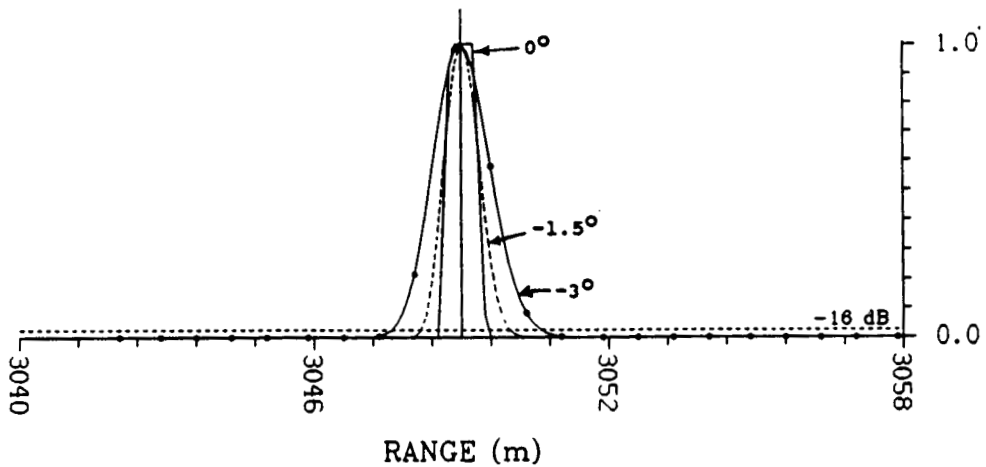


Figure 30. Simulated waveform shapes for the nadir beam and slopes between -1.5 and +1.5 degrees. The shapes are similar to that of the transmitted pulse.

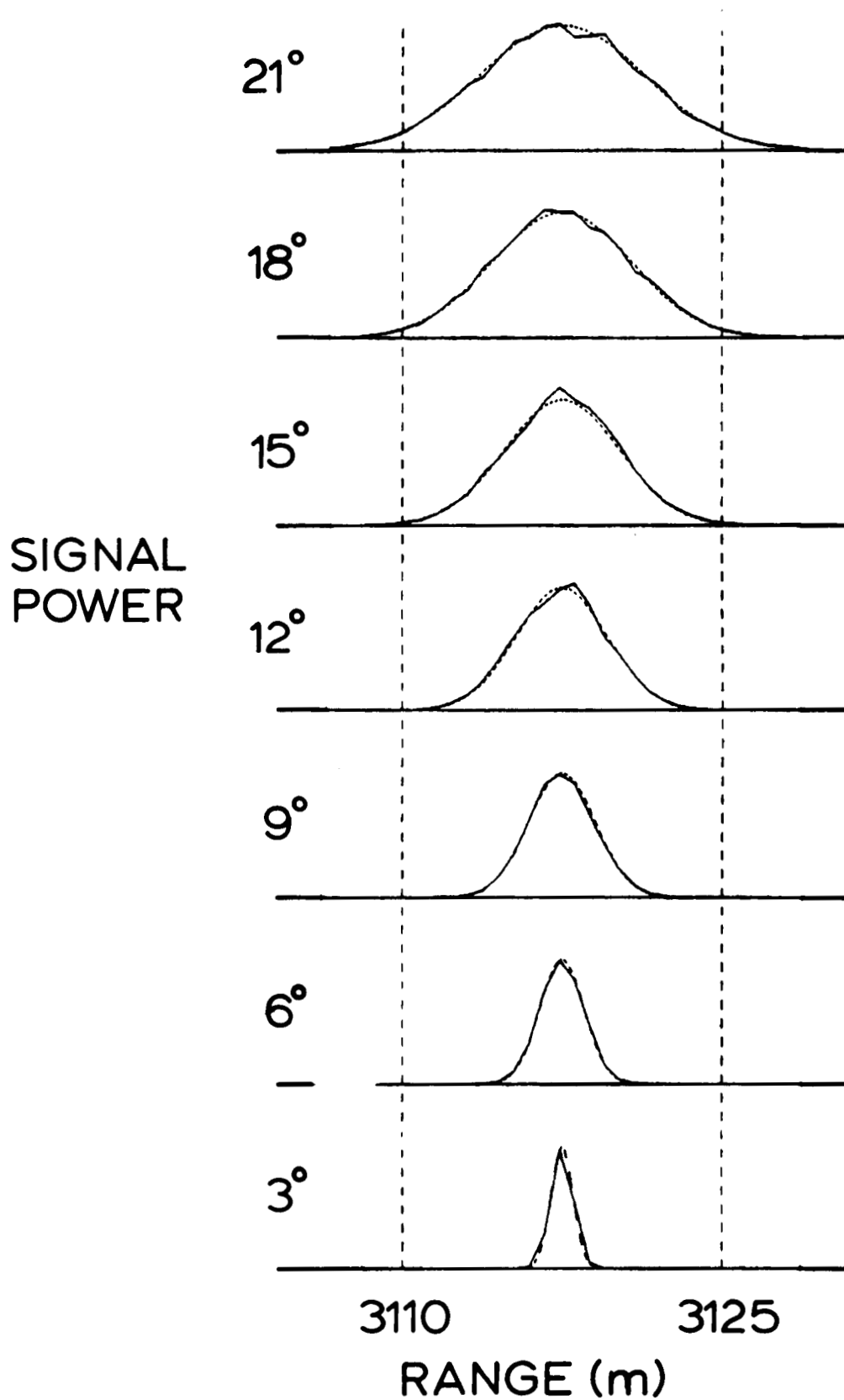


Figure 31. Simulated waveform shapes for total incidence angles ranging from 3 to 21 degrees. The expected return (dotted) and the average of 500 pulses (solid) are shown versus measured range.

For the MARA, a nominal pulse width of 5 ns has been adopted as a design goal. This should be achievable without requiring the use of pulse compression techniques (Walsh, 1974). And, this gives a reasonable number of independent samples for the simulated waveforms described in this section. For this pulsewidth, it can be argued that the system RF bandwidth must be at least 200 MHz. This requirement must be placed on the key RF components, especially the transmitter.

#### 4.6 Pulse-Repetition-Frequency

In the last section, there was a discussion of the temporal decorrelation within a backscattered waveform due to Rayleigh fading. The returned signal can be considered correlated within the temporal extent of the transmitted pulse. In this section, the spatial decorrelation caused by the movement of the sea surface and the aircraft platform is discussed. The Pulse-Repetition-Frequency (PRF) is the rate at which the transmitted pulse is generated and radiated by the radar transmitter. If the pulses are transmitted so rapidly that the backscattered waveforms are correlated with the preceding and succeeding waveforms, then it can be argued that the PRF is overly high. That is, there is no new information to be gained from the correlated returns. Therefore, determining the maximum decorrelated PRF is an important design exercise.

Walsh (1974) is an authoritative source for information about spatial decorrelation of aircraft radar returns. That analysis was based upon the van Cittert-Zernike theorem (Born and Wolf, 1964). This theorem states that if the linear dimensions of a source and the distance between a fixed point  $P_1$  and a variable point in space  $P_2$  are small compared with the distance of these points from the source, then the degree of coherency is equal to the absolute value of the normalized Fourier transform of the intensity function of the source. Given that the source is uniform and circular, the transform can be evaluated to reveal that the degree of coherency is proportional to a Bessel function of the first kind and of order one. This is the same function found in the Airy pattern. The first nulls of the function can be used to represent complete incoherence. This occurs when  $P_1$  and  $P_2$  are separated by the distance

$$P_1 P_2 = .61 R \lambda / \rho \quad (25)$$

where  $R$  is the distance between the source and the illuminated points,  $\rho$  is the radius of the source aperture, and  $\lambda$  is the electromagnetic wavelength. Walsh divided the above formula by two to account for the two-way illumination path for an airborne radar system. Using simple geometry, it can be found that the diameter of the half-power width of the two-way antenna pattern (.42 degrees) at 12 degrees off-nadir is 23.35 m. Hence,  $\rho$  is 11.7 m. The wavelength is .008333 m and  $R$  is approximately 3116.1 m. For this geometry, the decorrelation distance is .677 m. Assuming an aircraft velocity of 100 m/s, the maximum decorrelated PRF is found to be 147.7 Hz.

Other factors are also of importance in the determination of the PRF. The value computed above is based upon the difference in phase of the received signal across the illuminated footprint, which is primarily the result of geometry. For operation over the sea surface, the illuminated spot is a random surface, with Rayleigh fading from the wave field and its movement affecting the returned signal. Random fluctuations can be reduced by increasing the PRF. The more waveforms that can be averaged, the less important is the fluctuating component of the signal. The random variations would be reduced by the reciprocal of the square root of the number of averaged

waveforms. Hence, there is a rationale for increasing the PRF much higher than the van Cittert-Zernike result.

The last factor taken into consideration in this section is the demands placed upon the MARA data system by high values of the PRF. With five channels to process in the Multibeam Mode, the nominal design goal PRF was set at 200 Hz for each channel. If and when the data system is able to operate effectively at higher values, the system PRF will be increased. At 200 Hz., the van Cittert-Zernike limit is roughly matched so that the returns should be essentially decorrelated.

For the SCR Mode, the PRF requirements will be significantly different. The main difference in system characteristics between this mode and the Multibeam Mode will be the PRF. For the SCR Mode, the rotating mirror will have a scanning rate of M revolutions per minute (rpm). Because we intend to use both sides of the mirror as reflecting surfaces, the effective cross-track scan rate will be 2M. Given that the P-3 average groundspeed is V (nominally 100 m/s), the pixel dimension in the along-track direction can be computed from

$$\Delta r = 30V/M \quad (26)$$

In the across-track direction, we want 64 contiguous footprints between the  $\pm 12$  degree observation limits of the lens antenna. Given that the altitude of the aircraft is h, the cross-track dimension of the instantaneous pixel can be computed using

$$\Delta s = h \tan 12^\circ / 64 \quad (27)$$

Both of these relationships are plotted in Figure 32. At the nominal Multibeam Mode cruising altitude of 3048 m, the cross-track dimension is 10.12 m. To have a matching dimension in the along-track direction will require a mirror rotation rate of 295.3 rpm. By dropping in altitude by half, the cross-track dimension is reduced to 5.06 m requiring a mirror rate of 592.9 rpm for a square pixel.

The 24 degree angular width of the swath constitutes 13.33% of a half mirror rotation. Within that width, the 64 samples will require a burst PRF of 4800 pulses per second for the 10 m \* 10 m pixel and 9600 pulses per second for the 5 m \* 5 m pixel. The average PRF for this mode is 640/s for the larger pixel and 1280/s for the smaller. The requirement for the Multibeam Mode is for 200/s from each of five channels. Hence, the average PRF requirement for the SCR Mode is about the same as the total requirement for the Multibeam Mode. The pulses will have to be transmitted, however, in a burst mode during the proper part of the mirror's scan.

#### 4.7 Tracking Precision

To estimate the tracking precision that would result for the MARA radar using the design parameters derived in this report, the Monte Carlo simulation discussed earlier was used. Using the Gaussian mean return shapes such as those shown in Figure 27, the exponentially distributed random number generator was used to produce an instantaneous sample value of the Rayleigh fluctuating signal from the value at each point of these mean return shapes. Figure 31 shows the

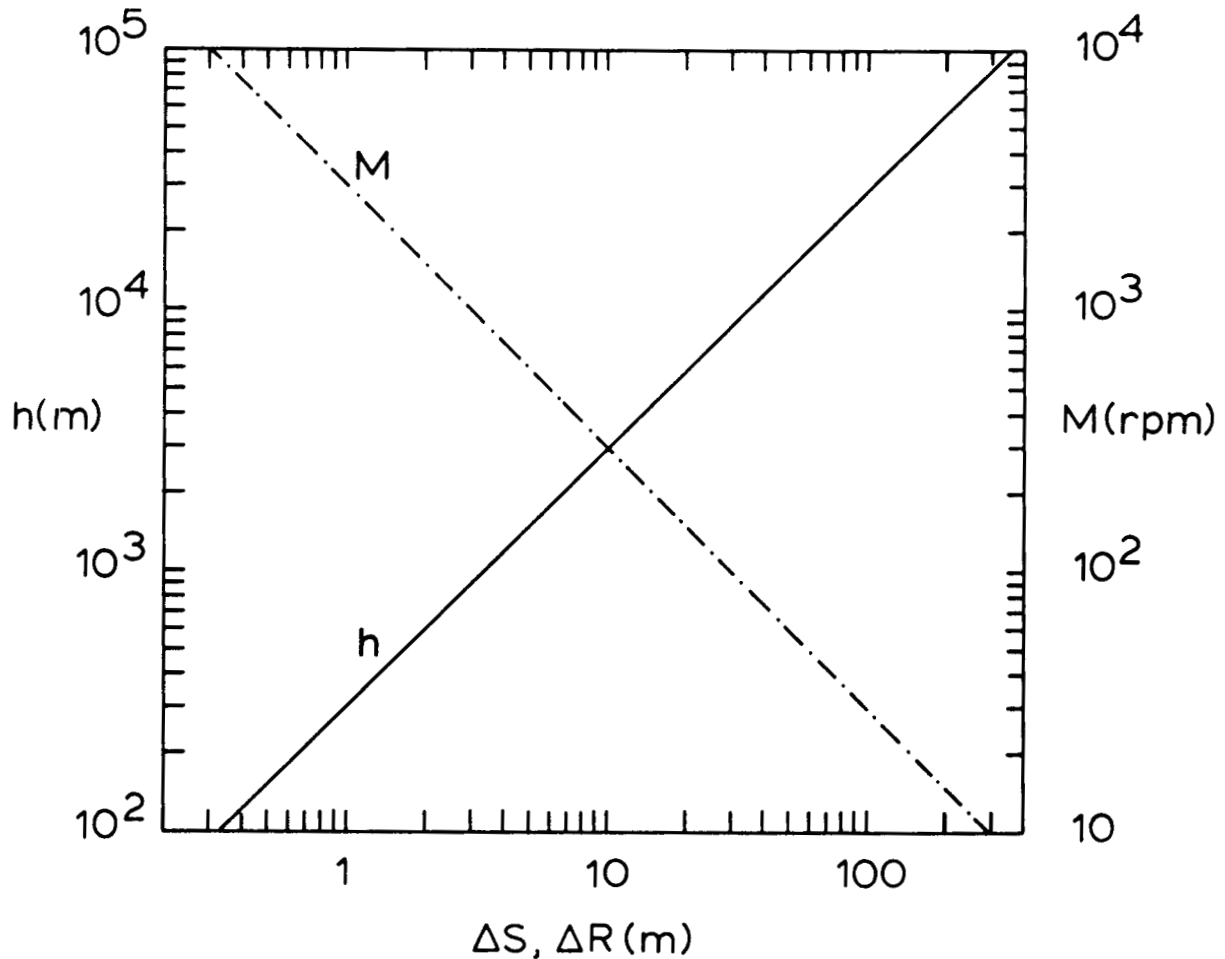


Figure 32. Pixel dimension in the cross-track direction,  $\Delta S$ , as a function of aircraft altitude,  $h$ . Pixel dimension in the along-track direction,  $\Delta R$ , as a function of scan motor speed,  $M$ .

resultant waveform obtained by averaging 500 of these Rayleigh fading waveforms. The fluctuating values were then used to compute the following descriptors of the noisy waveforms. The total power in the return signal was defined to be

$$\text{Power} = \sum_{i=1}^N P_i \quad (28)$$

where  $P_i$  is the amplitude of the noisy waveform at sample  $i$ .  $N$  is the total number of samples in the waveform, and the sample spacing is 5 ns, the assumed width of the transmitted pulse. The centroid of the noisy return is used to determine the range variation, and it is defined as

$$\text{Centroid} = \frac{\sum_{i=1}^N P_i * i}{\sum_{i=1}^N P_i} \quad (29)$$

Finally, the width of the waveform is found using the formula

$$\text{Width} = \left\{ \left( \frac{\sum_{i=1}^N P_i * i^2}{\sum_{i=1}^N P_i} \right) - \left( \frac{\sum_{i=1}^N P_i * i}{\sum_{i=1}^N P_i} \right)^2 \right\}^{1/2} \quad (30)$$

For each width of the mean return, 2000 trials of the Monte Carlo simulation were run so that standard deviations of the three noisy waveform descriptors could be computed. The circles in Figure 33 show the standard deviation of the range estimate as a function of the half-power width of the mean return waveform. The simulation assumes that the sea surface within the beam can be represented by a plane, so that this half-power width can be uniquely related to the local incidence angle of the beam as indicated by the second axis at the bottom of Figure 33. The deviation from the nominal 12 degree incidence angle could be the result of either sea surface slopes or aircraft attitude.

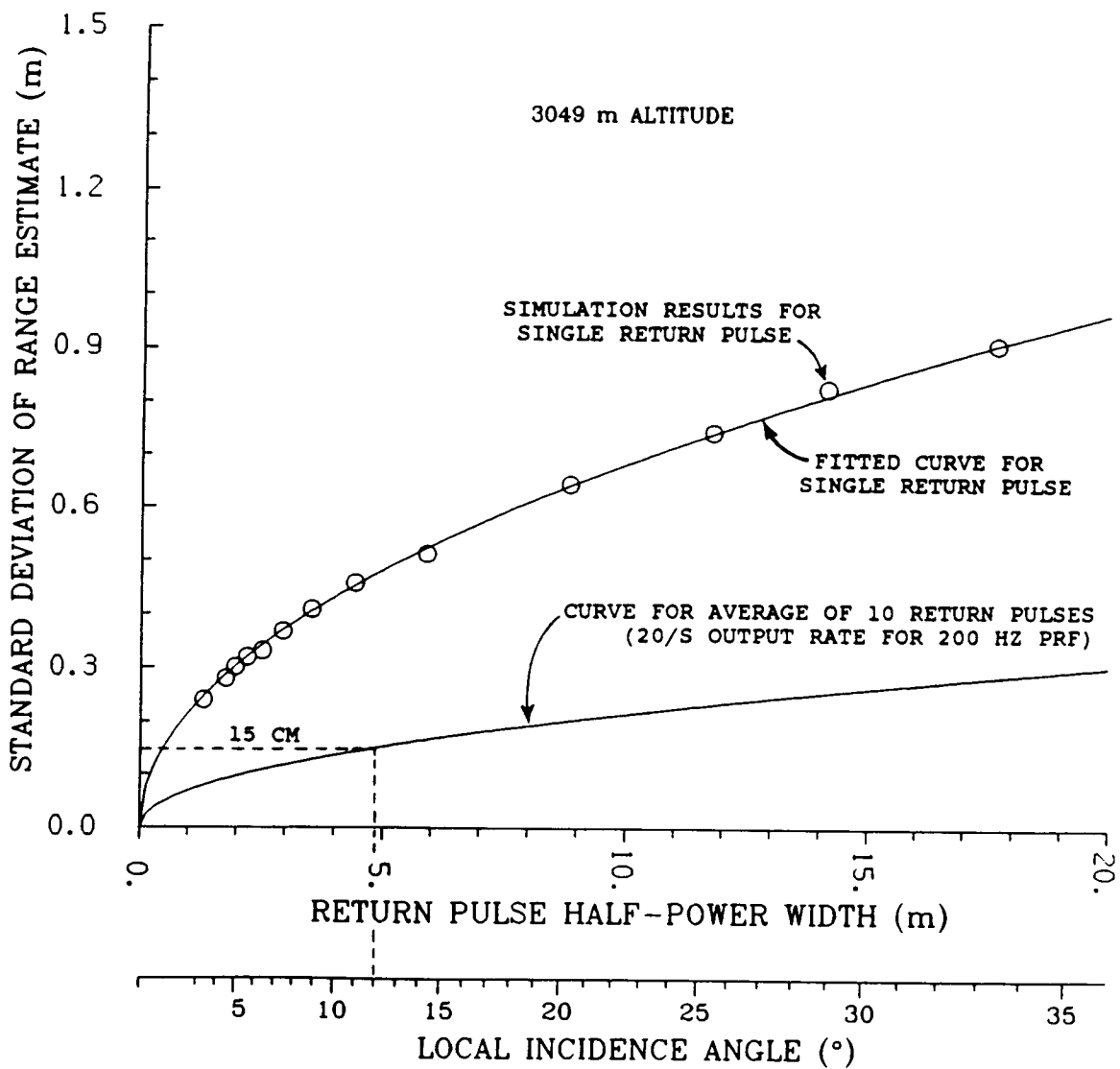


Figure 33. A simulated variation of the Multibeam Mode range tracking precision as a function of incidence angle and the return waveform half-power width.

The curve which passes through the circles assumes that the standard deviation of the range estimate increases as the square root of the half-power width of the mean return. The multiplicative constant for the curve was adjusted so it would pass directly through the circle at the far right. The agreement between this simple model and the simulation results is remarkably good. The bottom curve gives the noise level on the average of the range estimates from 10 return waveforms. It is the top curve divided by the square root of 10. The dashed lines point out that at the nominal incidence angle of 12 degrees, the noise level in the range estimate at a 20/s averaged waveform PRF would be about 15 cm. Since the two-way half-power footprint of the MARA is about 23 m at 3048 m altitude and the aircraft moves only about 5 m in .05 s, the radar should have no difficulty profiling a 120 m wavelength wave of 2 m amplitude.

The circles in Figure 34 show the standard deviation of the power estimate for the same groups of 2000 noisy waveforms from the Monte Carlo simulation. The reason that this standard

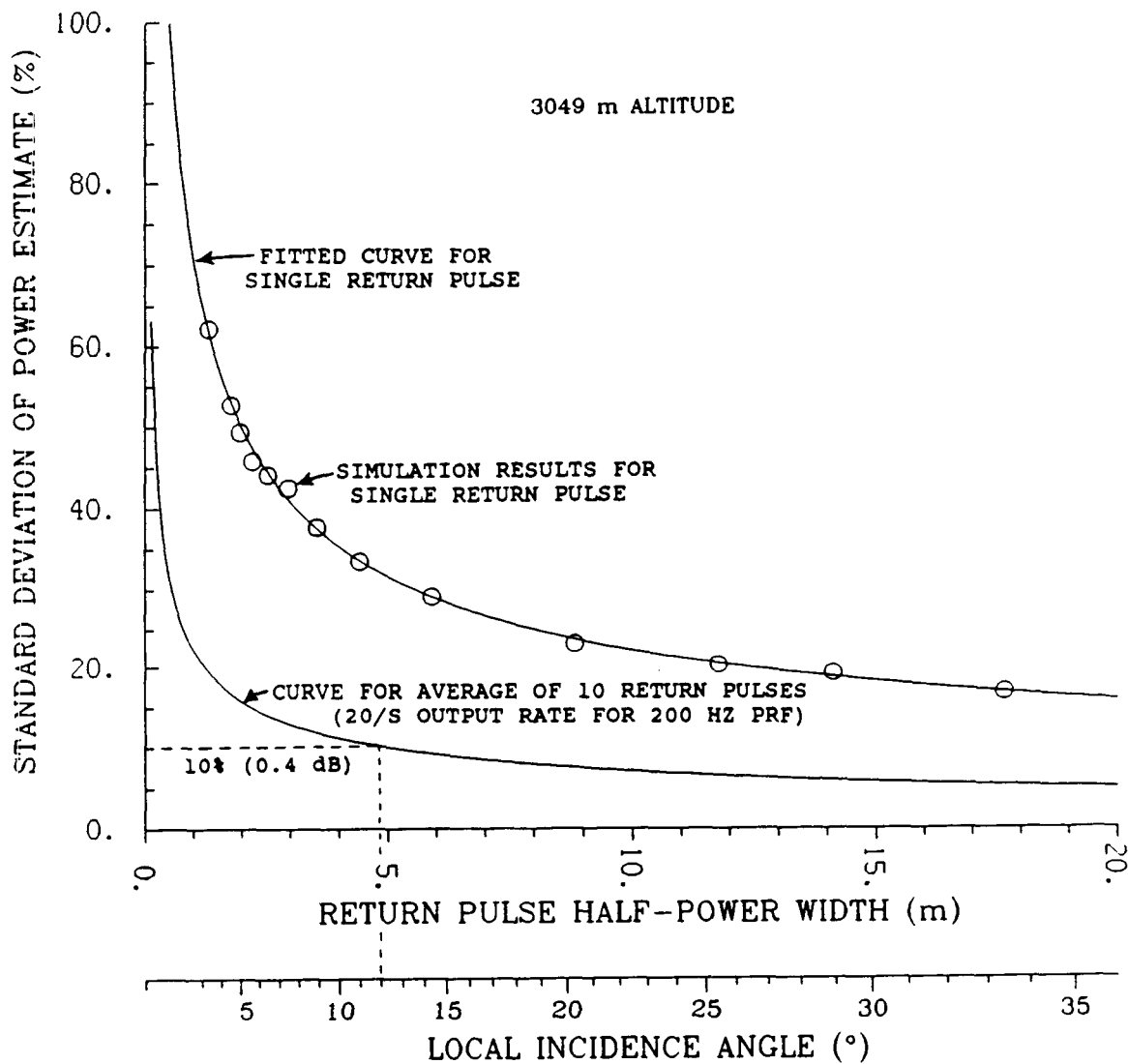


Figure 34. A simulated variation of the Multibeam Mode power measurement as a function of incidence angle and the return waveform half-power width.

deviation decreases with increasing mean return width is that the power is being distributed over more independent samples as the width grows and more power is lost out of the two-way antenna pattern. The curve passing through the points assumes that the standard deviation of the power estimate decreases as the square root of the width of the mean return. The multiplicative constant was again adjusted so that the curve would pass through the circle at the far right. Again, the match between this model and the simulation results is excellent. The lower curve is the estimated standard deviation of the power estimate for the average of 10 noisy returns. The dashed lines indicate that the nominal noise level in the power estimate at a 20/s output averaged waveform data rate would be only .4 dB.

Figure 35 shows the standard deviation of the estimated half-power width of the noisy return waveform. The solid curve through the circles indicates that the standard deviation increases as the square root of the width of the mean return. The second curve is again a factor of 3.16

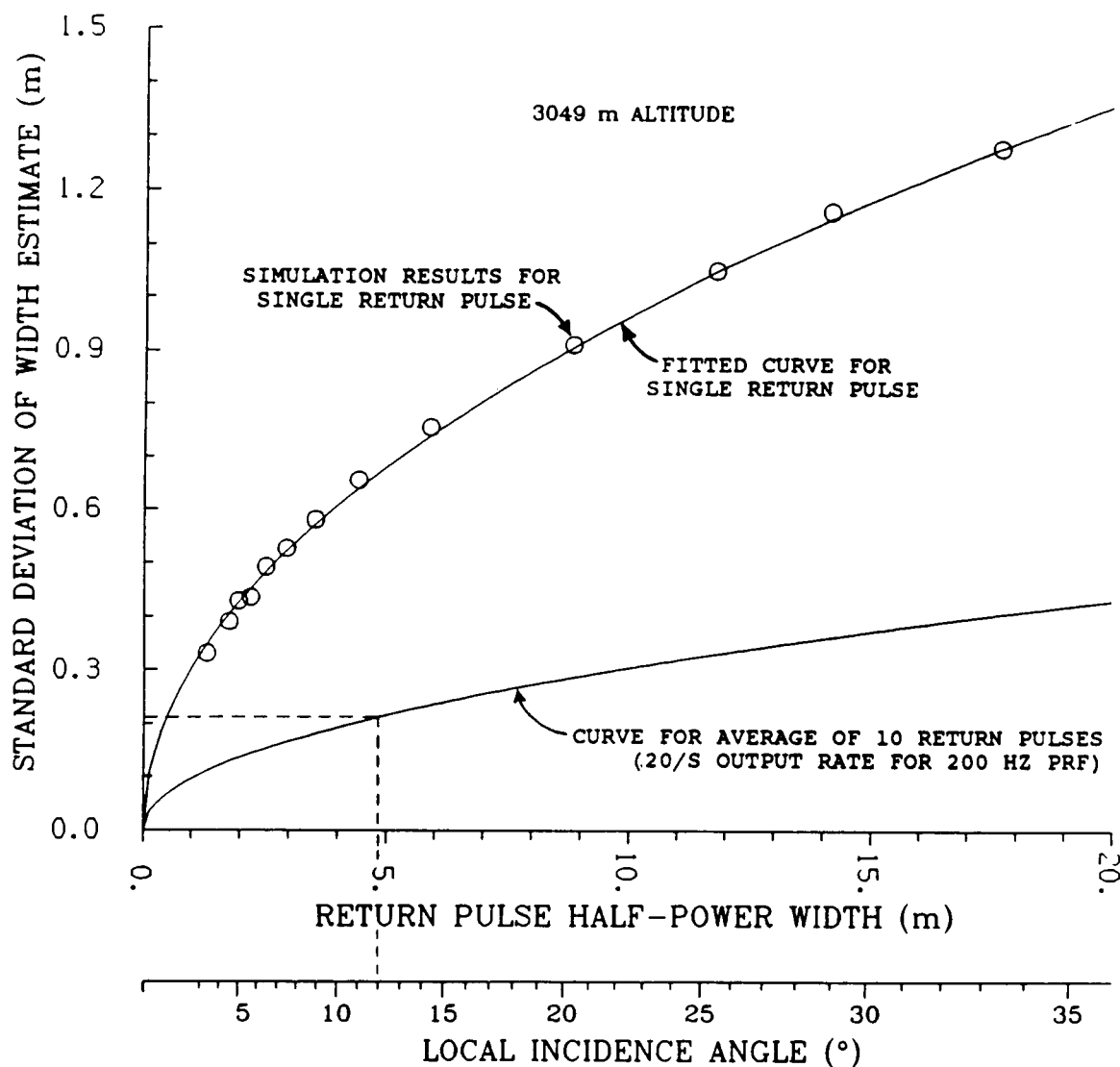


Figure 35. A simulated variation of the Multibeam Mode waveform width estimate as a function of incidence angle.

lower than the first. The dashed lines indicate that a 20/s output rate would have a standard deviation of about 21 cm for the averaged noisy waveform half-power width at 12 degrees incidence angle. The mean return width at that angle is 4.85 m. Therefore, the standard deviation of the estimate is 4.4% of the actual mean value. If we use the width of the mean return to infer the local incidence angle, then we can estimate its accuracy by using this simulation result. Assuming that the mean return width and the incidence angle are linearly related, then the standard deviation of the incidence angle estimate would be given approximately by  $.044 * 12 \text{ degrees} = 0.52 \text{ degrees}$ . Therefore, the local incidence angle can be estimated solely from the MARA's waveform data with an estimated precision of .52 degrees.

#### 4.8 Signal-to-Noise Calculations

In this section, we derive the appropriate forms of the radar range equation for the MARA nadir and off-nadir geometries. Given the antenna system's parameters, our operating frequency, and our pulse width design goal, we then use these equations to compute the amount of transmitted power necessary for operation over a variety of surfaces and at various altitudes. These results are needed in the specification of the power transmitter for the RF subsystem, which is described in detail in Volume II of the MARA System Documentation.

We begin our development at the most elementary level. For a radar with transmitted power,  $P_t$ , the power density spreading from an omnidirectional antenna would be

$$P_t / 4\pi R^2 \quad (31)$$

When transmitted by an antenna system of gain,  $G_t$ , the power density becomes

$$P_t G_t / 4\pi R^2 \quad (32)$$

The amount of power that is incident upon the illuminated surface is

$$( P_t G_t / 4\pi R^2 ) A_s \quad (33)$$

where  $A_s$  is the effective surface area illuminated by the beam.  $A_s$  depends upon the effectiveness of the scattering surface as a receiving antenna. To account for power absorption by the surface, introduce  $f_a$  as the fraction absorbed. Then, the power reradiated by the surface is

$$( P_t G_t / 4\pi R^2 ) A_s ( 1 - f_a ) \quad (34)$$

This reradiation has its own antenna pattern and gain,  $G_r$ , and spreading factor. The power received per unit area at the receiver is then given by

$$(P_t G_t / 4\pi R^2) A_s (1 - f_a) (G_s / 4\pi R_r^2) \quad (35)$$

The power entering the receiver is

$$(P_t G_t / 4\pi R^2) A_s (1 - f_a) (G_s / 4\pi R_r^2) A_r \quad (36)$$

where  $A_r$  is the effective aperture of the antenna receiving the signal.

Recombining terms, the received power can be expressed as

$$P_r = \frac{P_t G_t A_r}{(4\pi)^2 R^2 R_r^2} [A_s (1 - f_a) G_s] \quad (37)$$

The terms in brackets pertain to the scattering surface and are grouped together as the parameter  $\sigma$ , the radar scattering cross-section.

Thus,

$$P_r = \frac{P_t G_t A_r \sigma}{(4\pi)^2 R^2 R_r^2} \quad (38)$$

For a monostatic radar such as the MARA,  $R = R_r$ ,  $A_t = A_r = A$ , and  $G_t = G_r = G$ . Furthermore, using the definition

$$A = \lambda^2 G / 4\pi \quad (39)$$

where  $A$  is the effective area of an antenna,

$$P_r = \frac{P_t G_t \lambda^2 \sigma}{(4\pi)^3 R^4} \quad (40)$$

This is the basic formulation of the radar range equation that will be used throughout this documentation.  $P_r$  is the received, backscattered power. By comparing it to the amount of noise that is found in the receiver, then the signal-to-noise ratio (S/N) can be computed. The input noise to the receiver is

$$N = k T_o B_n \quad (41)$$

where  $k =$  Boltzmann's constant  $= 1.38 * 10^{-23}$  joules/deg K  
 $T_0 =$  ambient temperature in deg K  
 $B_n =$  noise bandwidth in Hz.

This represents the antenna's detected signal due solely to the movement of electrons under the influence of the ambient temperature. The noise introduced by the components of the receiver to the point of intermediate-frequency (IF) envelope detection is characterized by the receiver's noise figure, F. Finally, the total losses in the system and in the two-way propagation to the surface and back are represented by a loss parameter, L. Using these, the basic S/N equation becomes

$$\frac{S}{N} = \frac{P_t G^2 \lambda^2 \sigma}{(4\pi)^3 R^4 L k T_0 B_n F} \quad (42)$$

The backscattering cross-section equals  $\sigma_0 A$ , where A is the effective illuminated area and  $\sigma_0$  is the backscattering cross-section per unit area. To understand the contribution of the footprint geometry to the S/N calculations, see Figure 36. Assume for now that the transmitter is omnidirectional. Then, the beamwidth of the signal is not a factor in the next discussion. The transmitter emits a narrow pulse of width,  $\tau$ , in the nadir direction. If the leading edge of this pulse is denoted as a, then a is reflected by the surface at the nadir point and received back at the sensor at time  $t_0$  after transmission. The trailing edge of the pulse, denoted as b, is transmitted at time  $\tau$  after a, follows the same path as a and is received by the sensor at time  $t_0 + \tau$ . In the extra time,  $\tau$ , taken for the trailing edge to be transmitted, the leading edge has traveled an additional distance, d. Therefore, at time  $t_0 + \tau$  the leading edge is received by the sensor after a round-trip to point Q. Representing the altitude of the sensor as h, then

$$2h = ct_0$$

$$h = ct_0 / 2$$

$$2(h + d) = c(t_0 + \tau) \quad (43)$$

$$h + d = \frac{ct_0}{2} + \frac{c\tau}{2}$$

$$d = \frac{c\tau}{2}$$

The distance, d, is the path swept out by a pulse of width  $\tau/2$  travelling at the speed of light. The surface distance,  $r_0$ , defined as the length PQ can be found to be

$$r_0 = \sqrt{hc\tau} \quad (44)$$

using the Pythagorean Theorem. The circle defined by this radius,  $r_0$ , has an area equal to  $2\pi r_0$  and is defined to be the pulse-limited footprint. For MARA operating at an altitude of 10,000 ft.

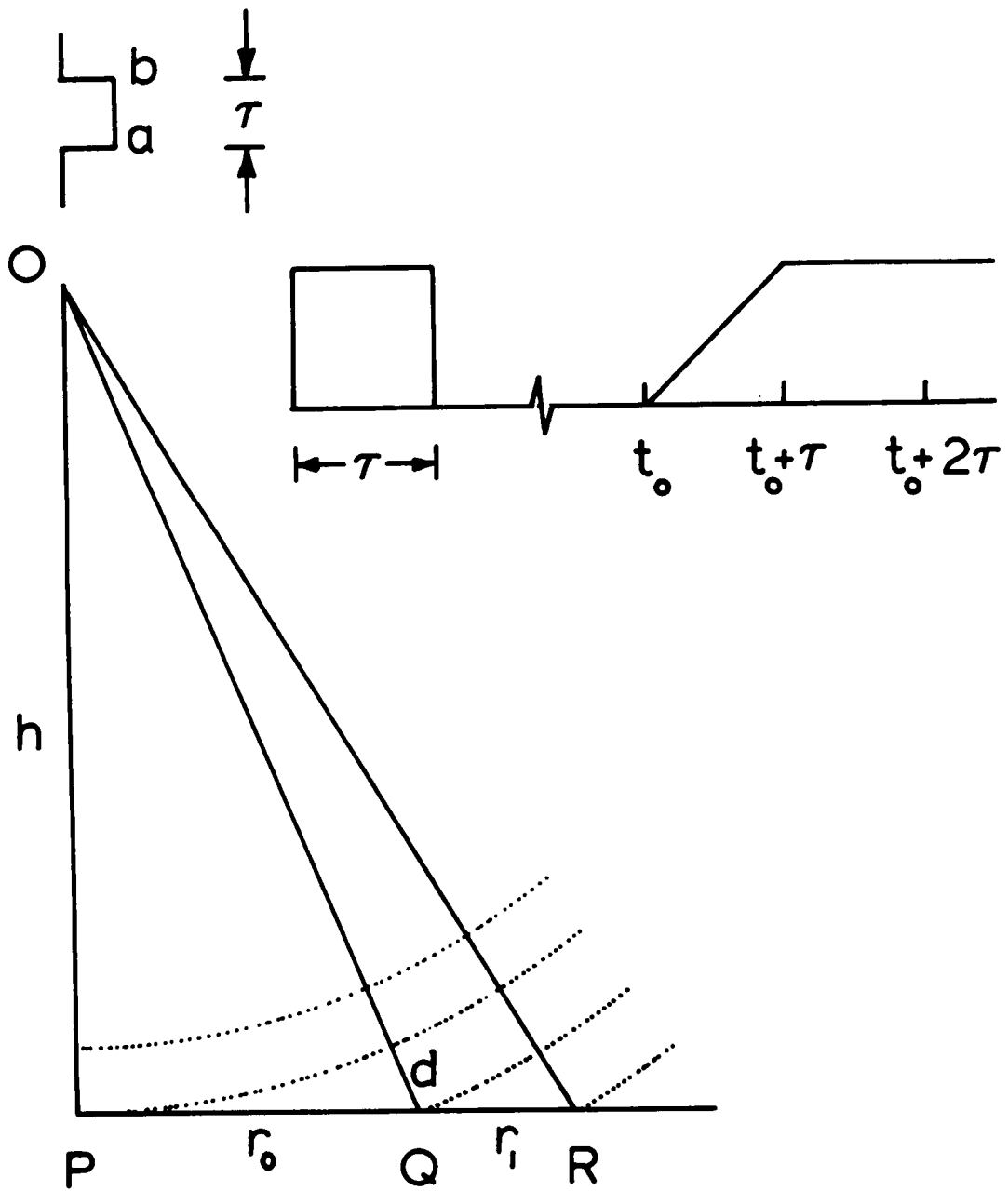


Figure 36. Pulse-limited altimetry timing schematic.

(3048 m), and for a 10 nsec pulsewidth, the radius of the pulse-limited footprint is 95.62 m. For a pulsewidth of 5 nsec, the radius is 67.62 m.

As the spherical wavefront continues its propagation, the illuminated area on the surface becomes an annulus. From Figure 36, the leading edge is received from point R at time  $t_0 + 2\tau$  in coincidence with the arrival of the trailing edge from point Q. The width of the annulus between Q and R is denoted as  $r_1$ . Using the Pythagorean Theorem again yields

$$r_1 = \sqrt{2hc\tau} - \sqrt{hc\tau} \quad (45)$$

By induction, the width,  $r_n$ , of the nth annulus is given by

$$r_n = \left\{ \left( 2n + 1 - 2\sqrt{n(n+1)} \right) hc\tau \right\}^{1/2} \quad (46)$$

Figure 37 shows the narrowing of the annuli as the distance off-nadir increases. At 12 degrees off-nadir, the chosen off-nadir angle for the MARA Multibeam Mode, (46) can be used to find that at 10,000 ft. operation with a 10 nsec pulsewidth, the MARA boresight will fall in the 45th annulus. Its width is 7.01 m. For a 5 nsec pulsewidth, the boresight is in the 91st annulus, which has a width of 3.53 m.

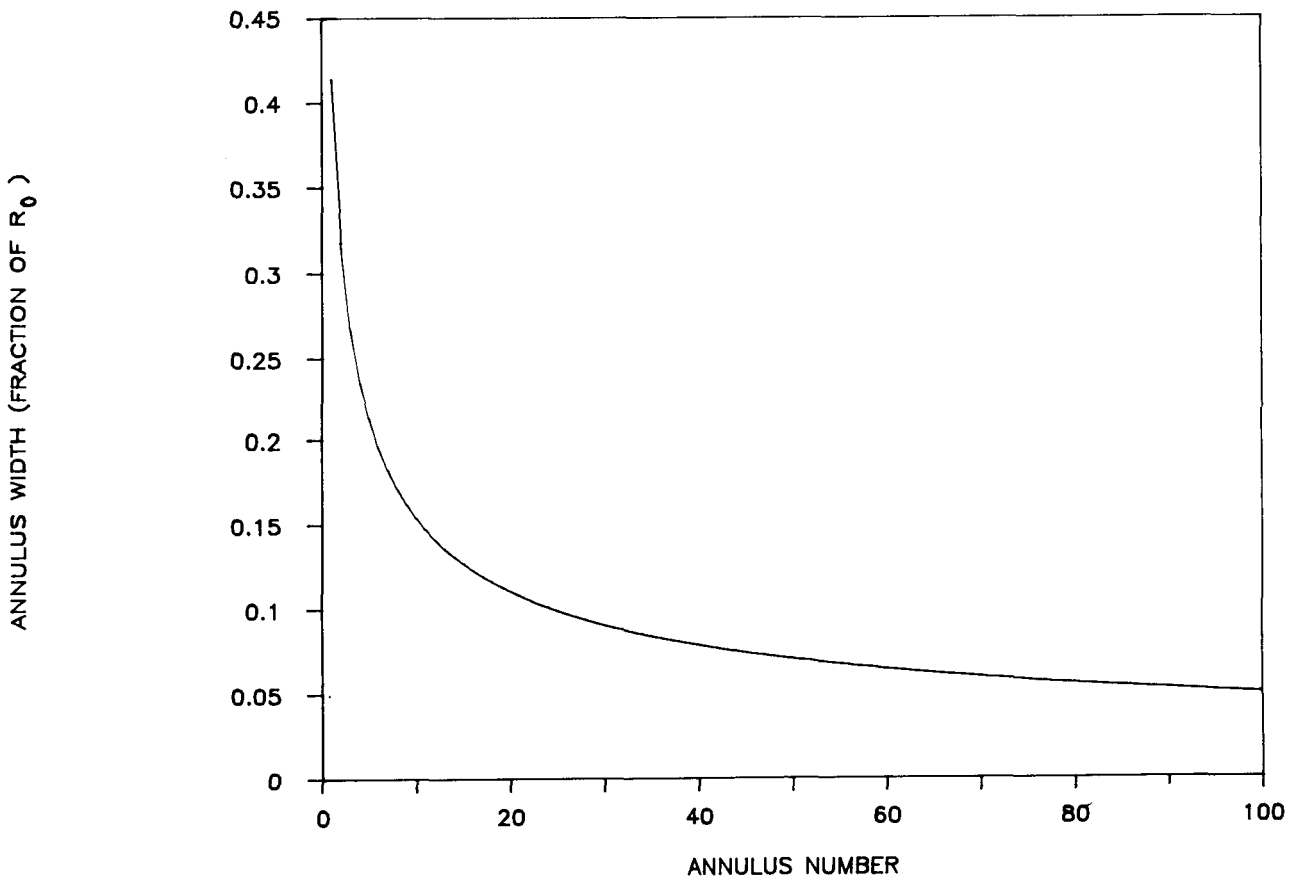


Figure 37. The width of a pulse-limited altimeter's annulus of illumination as a function of annulus number. The pulse-limited footprint has the index 0.

The preceding discussion characterizes pulse-limited altimetry - the beamwidth of the transmitting antenna is not a factor. For the MARA dielectric lens and its beamwidth of .6 degrees the beam can be modeled as a Gaussian shape with half-power width  $\theta_{1/2}$  with little error. The reradiated pattern from the surface then is the product of two Gaussians assuming that the surface is an isotropic scatterer. The effective width of the resultant beam pattern,  $\theta_e$ , is compared with the incident beamwidth,  $\theta_{1/2}$ , below.

$$g_{\text{inc}}(\theta) = e^{-\theta^2 \ln.5 / \theta_{1/2}^2}$$

$$g_{\text{scat}}(\theta) = g_{\text{inc}}^2(\theta) = e^{-2\theta^2 \ln.5 / \theta_{1/2}^2}$$

$$g_{\text{scat}}(\theta_e) = .5$$

$$\theta_e = \frac{1}{\sqrt{2}} \theta_{1/2}$$
(47)

The reradiated beamwidth is .707 of the incident beamwidth. Thus, the effective beam-limited footprint size is defined using the effects of the finite width of the antenna patterns. For our S/N calculations, this is the only occasion that the antenna pattern is involved at all. The gains in (42) are the maximum antenna gains in the direction of the antenna boresight. Using the two-way antenna beamwidth, the illuminated footprint diameter is

$$s = h \theta_e \quad (\theta_e \text{ in radians})$$
(48)

The radius of this beam-limited footprint from 3048 m altitude is 11.17 m. The beam-limited footprint is therefore only 11.7% of the 10 nsec pulse-limited footprint radius and 16.5% of the 5 nsec radius. Therefore, the MARA is beam-limited at nadir and the effective illuminated area is

$$A = \pi \left( \frac{s}{2} \right)^2$$
(49)

For off-nadir angle  $\psi$ , the illuminated footprint dimension in the plane containing the nadir and the off-nadir boresights is given by

$$R \theta_e / \cos \psi$$
(50)

In the other dimension, the footprint extent is defined solely by the beam width so that it is given by

$$R \theta_e$$
(51)

As shown in Figure 38, the off-nadir beam-limited footprint is an ellipse which has an area given by

$$\pi \left( \frac{R\theta_e}{2} \right) \left( \frac{R\theta_e}{2 \cos \psi} \right) = \frac{\pi R^2 \theta_e^2}{4 \cos \psi} \quad (52)$$

For MARA at an altitude of 3048 m and an off-nadir look angle of 12 degrees, this beam-limited footprint area is 418.9 sq. m. The extent in the plane of the boresight is 22.84 m which is much larger than the width of the pulse-limited annulus at that angle. Therefore, for off-nadir angles, the MARA is pulse-limited in this dimension and beam-limited in the orthogonal dimension. The illuminated area shown in Figure 38 is approximately a rectangular segment of the beam-limited footprint and its area is given by

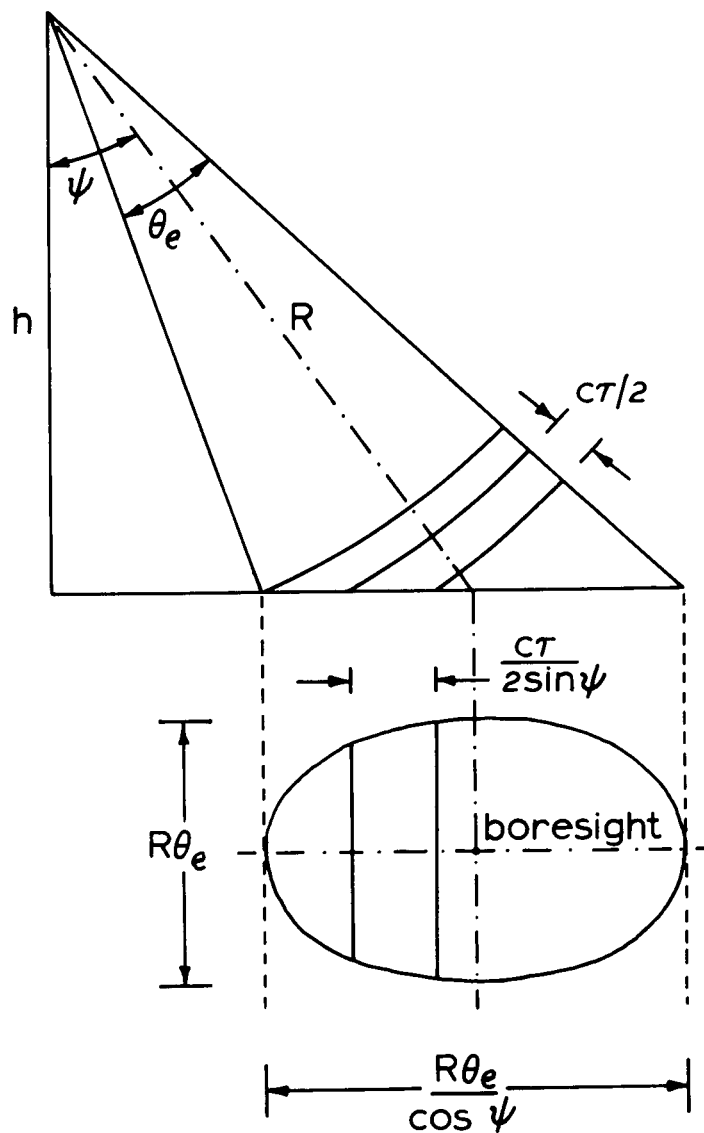


Figure 38. Beam-limited altimetry footprint.

$$\frac{c\tau}{2 \sin \psi} * R \theta_e = \frac{c\tau R \theta_e}{2 \sin \psi} \quad (53)$$

With this equation, we now have sufficient information to characterize the MARA S/N equation. The appropriate equations for nadir and off-nadir operation of the MARA are given below.

$$\left( \frac{S}{N} \right)_{\text{nadir}} = \frac{P_t G^2 \lambda^2 \sigma_o \theta_e^2}{256 \pi^2 h^2 L k T_o B_n F} \quad (54)$$

$$\left( \frac{S}{N} \right)_{\text{off-nadir}} = \frac{P_t G^2 \lambda^2 \sigma_o c \tau \theta_e}{128 \pi^3 R^3 L k T_o B_n F \sin \psi} \quad (55)$$

Before using these equations to establish our minimum transmitter power requirements, we must characterize the backscattering cross-sections per unit area of typical surfaces. A significant amount of information was received from the University of Massachusetts (C. Swift, personal communications). A database containing previously published  $\sigma_o$  values for different targets and as a function of frequency, incidence angle, and polarization is maintained by the University. A representative subset of the data available at 36 GHz can be found in Appendix B. The MARA 12 degree maximum off-nadir angle is indicated on each page. The cross-sections at 12 degrees incidence vary from a minimum of -23 dB for a smooth concrete road to a maximum of +8 dB for 27 cm deep snow. Further values for sea return were found in Grant and Yaplee (1957). They found that the cross-section per unit area for a windspeed of 15-20 mph was 7.2 dB and the value for a 5 mph wind was -6.3 dB. At nadir, the sea return  $\sigma_o$  value was 13 dB for the higher wind and 15.9 dB for the lower wind. These values are compared in Figure 39 with laboratory wavetank measurements of the backscattering cross section per unit area made at the Wallops Flight Facility Wind-Wave Tank Facility (Parsons and Norcross, unpublished manuscript). The agreement is excellent for the higher windspeed. The laboratory measurements at windspeeds lower than 4 m/s are difficult because the assumption of rough scattering is not valid (Miller and Parsons, unpublished manuscript). It is sufficient to note that the minimum expected  $\sigma_o$  value can be set at about -23 dB. This does not take into account any surface tilting. In the S/N equation for off-nadir operation, this effect would be handled by including the tilt angle in with the off-nadir incidence angle.

Table III summarizes the nadir and off-nadir S/N ratio computations assuming that a resultant value of 15 dB is needed for proper instrument operation. This is the level normally used in the design of spacecraft altimeters (C. Purdy, personal communications).

Using the conservative -23 dB  $\sigma_o$  value and conservative receiver noise figures, this analysis resulted in the conclusion that a 1 kW transmitter is capable of acceptable performance at the comfortable S/N ratio of 15 dB at nadir. Keeping this same transmitter power at the maximum off-nadir angle of 12 degrees necessitates dropping the operating S/N value to 7.9 dB, which still is a comfortable working level. The receiver noise figure may be too conservative while the instrument loss estimate may be too small. It is assumed that the atmospheric losses can be ignored because the MARA operation can be restricted to fair weather without sacrificing any mission objectives.

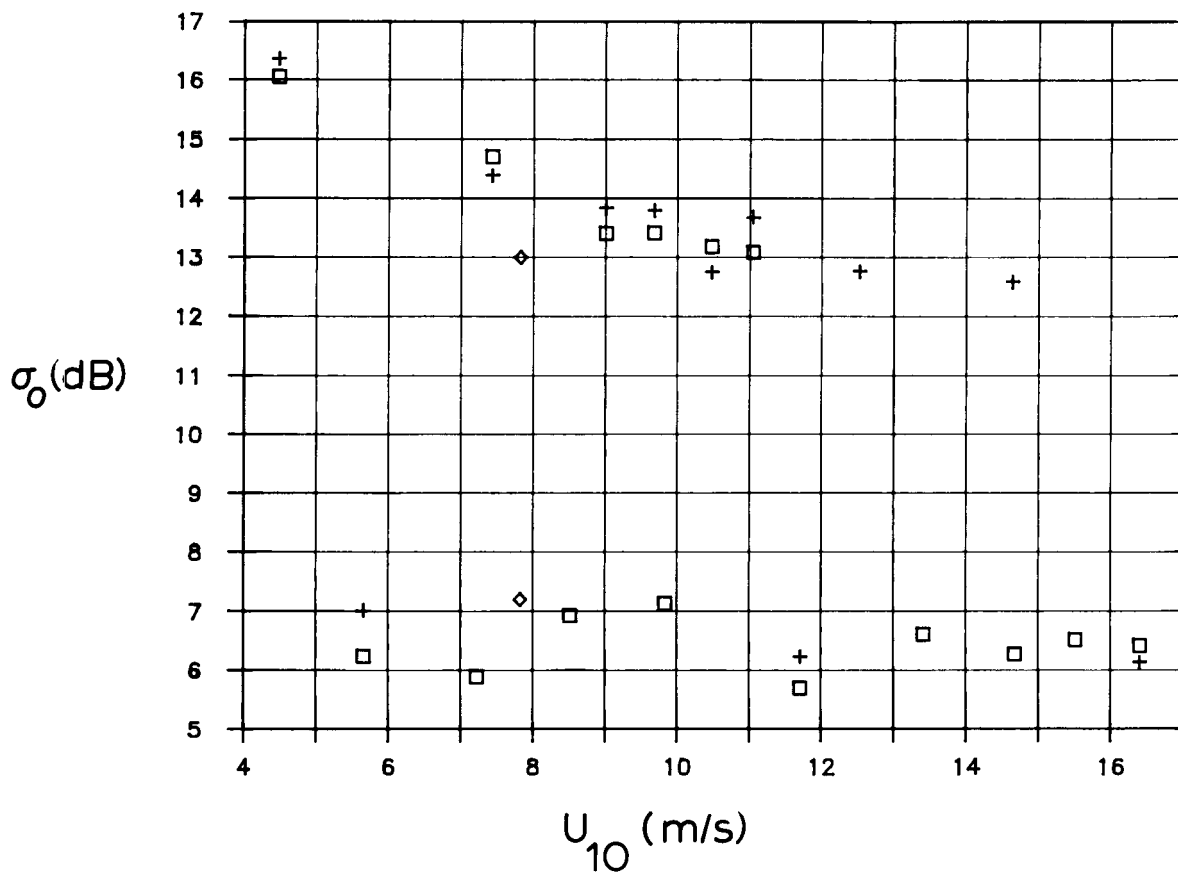


Figure 39. Measured variation of  $\sigma_0$  with wind speed. The squares and plus symbols are from Parsons and Norcross (unpublished manuscript) and the diamonds are from Grant and Yiplee (1957).

Table III. MARA S/N results

	NADIR	OFF-NADIR
Peak power (P)	30.0	30.0
Antenna gain ( $G^2$ )	95.0	95.0
Wavelength ( $\lambda^2$ )	-41.6	-41.6
Backscatter ( $\sigma_0$ )	-23.0	-23.0
Beamwidth ( $\theta_e^2$ )	-42.7	
( $\theta_e$ )		-21.3
Pulsewidth factor ( $c\tau$ )		1.8
Constant ( $1/(256*\pi^2)$ )	-34.0	
( $1/(128*\pi^3 * \sin \psi)$ )		-29.2
Range ( $1/h^2$ )	-69.7	
( $1/R^3$ )		-104.8
Noise ( $1/kT_0B_n$ )	121.0	121.0
Receiver noise figure (1/F)	-10.0	-10.0
Instrument losses ( $L_s$ )	-10.0	-10.0
Atmospheric losses ( $L_a$ )	0.0	0.0
S/N total	15.0 dB	7.9 dB

In summary, this preliminary S/N calculation indicates that a 1 kW transmitter will give the MARA the needed power to perform all of its mission objectives given the dielectric lens and a design goal pulsewidth of 5 nsec. This analysis is performed for an operating altitude of 10,000 ft., the cruising altitude for the P-3. If necessary, it is possible to decrease the operating altitude by half thereby increasing the S/N ratio by 6 dB.

#### 4.9 Coherent Processing

As mentioned in section 1.2, there has been a long-term interest in the coherent processing of microwave altimetry signals. No altimeter has utilized the phase information in its signal processing to date. The TOPEX altimeter will protect the phase information in its receiver but it will not be used in the on-board data processing and it will not be telemetered to earth so it will have no practical value.

For MARA, one facet of the design process will be to protect the capability of performing coherent detection. The selection of an RF transmitter will therefore include the requirement that the device chosen be capable of coherent operation. In general, this would limit the available devices to klystrons and traveling-wave-tubes at the MARA frequency and at the power levels that are required for adequate S/N ratios.

There are studies underway to investigate the optimum techniques for using the magnitude and phase information from a coherent receiver but they are not completed at this time.

#### 5.0 MARA DESIGN CHARACTERISTICS

Through the studies described in this report, the following characteristics have been adopted as design goals for the Multimode Airborne Radar Altimeter.

##### MARA SYSTEM CHARACTERISTICS

<u>Characteristic</u>	<u>Multibeam Mode</u>	<u>SCR Mode</u>
No. of beams	5	1 (scanning)
Frequency	36.0 GHz	36.0 GHz
Transmitted Power	1 kW	1 kW
Pulsewidth	5 ns	5 ns
PRF	200 Hz/channel	1280 Hz average 9600 Hz burst
Max. Off-Nadir Angle	12 degrees	12 degrees
Beamwidth	.6 degrees	.6 degrees
Nominal Altitude	3048 m	3048 m

This summary of the MARA design goals completes Volume I, entitled MARA System Requirements Document, of the MARA System Documentation series.

## 6.0 REFERENCES

Barrick, D. E., "Determination of mean surface position and sea state from the return of a short-pulse satellite altimeter," in Sea Surface Topography from Space, edited by J. R. Apel, NOAA TR ERL 228-AOML7, p. 16-1, U. S. Government Printing Office, 1972.

Barrick, D. E., and W. H. Peake, "A review of scattering from surfaces with different roughness scales," Radio Science, vol. 3, pp. 865-868, 1968.

Barrick, D. E., and C. T. Swift, "The SEASAT microwave instruments in historical perspective," IEEE J. Oceanic Eng., vol. OE-5, no. 2, pp. 74-79, 1980.

Berger, T., "Satellite altimetry using ocean backscatter," IEEE Trans. Antennas and Propagation, vol. AP-20, no.3, pp. 295-309, 1972.

Bernstein, R. L., R. H. Whritner, and G. Born, "Determination of ocean current variability using SEASAT altimeter data," Trans. Amer. Geophys. Union, vol. 60, p. 232, 1979.

Born, G. H., D. B. Lame, and J. L. Mitchell, "A survey of oceanographic satellite altimetric missions," Marine Geodesy, vol. 8, nos. 1-4, pp. 3-16, 1984.

Born, M., and E. Wolf, Principles of Optics, The MacMillan Company, New York, 1964.

Brekhovskikh, L. M., "The diffraction of waves by a rough surface, part I," Zh. Eksper. i Teor. Fiz., vol. 23, pp. 275-289, 1952.

Brenner, A. C., R. A. Bindschadler, R. H. Thomas, and H. J. Zwally, "Slope-induced errors in radar altimetry over continental ice sheets," J. Geophys. Res., vol. 88, no. C3, p. 1617, 1983.

Brooks, R. L., "Monitoring of thickness changes of the continental ice sheets by satellite altimetry," J. Geophys. Res., vol. 84, no. B8, pp. 3965-3968, 1979.

Brooks, R. L., and G. A. Norcross, SEASAT Radar Altimeter Measurements over the Florida Everglades, NASA CR-156889, 23 pp., 1983.

Brooks, R. L., H. R. Stanley, W. J. Campbell, H. J. Zwally, and R. O. Ramseier, "Ice sheet topography by satellite altimetry," Nature, vol. 27, pp. 539-543, 1978.

Brown, G. S., "Concept for research memorandum: multiple beam radar altimetry for oceanographic and terrain remote sensing," Applied Science Associates, Inc., 27 pp., 1972.

Brown, G. S., "The average impulse response of a rough surface and its applications," IEEE Trans. Antennas and Propagation, vol. AP-25, pp. 67-74, 1977.

Brown, G. S., "A useful approximation for the flat surface impulse response," Chapter 2, Research on Multibeam Altimetry and Electromagnetic Bias, final report, NASA Grant No. NAG5-636, Virginia Polytechnic Institute and State University, Blacksburg, VA, pp. 77-94, 1988.

Bush, G. B., E. B. Dobson, R. Matyskiela, E. Walsh, and C. C. Kilgus, "An analysis and simulation of the multibeam altimeter," JHU/Applied Physics Laboratory Report SDO 5559, 1980.

Bush, G. B., E. B. Dobson, R. Matyskiela, C. C. Kilgus, and E. J. Walsh, "An analysis of a satellite multibeam altimeter," Marine Geodesy, vol. 8, nos. 1-4, pp. 345-384, 1984.

EOS Altimetric System Panel, Altimetric System, vol. III, Earth Observing System Reports, NASA, 61 pp., 1987.

Grant, C. R., and B. S. Yaplee, "Backscattering from water and land at centimeter and millimeter wavelengths," Proc. I.R.E., vol. 45, pp. 976-982, 1957.

Hayne, G. S., "Radar altimeter mean return waveforms from near-normal-incidence ocean surface scattering," IEEE Trans. Antennas and Propagation, vol. AP-28, no. 5, pp. 687-692, 1980.

Hurlbert, H. E., "The potential for ocean prediction and the role of altimeter data," Marine Geodesy, vol. 8, nos. 1-4, pp. 17-66, 1984.

Jet Propulsion Laboratory, "Land and ocean radar altimeter (LORA)," a proposal to NASA for Announcement of Opportunity No. OSSA-1-88, 1988.

Johns Hopkins University Applied Physics Laboratory, Johns Hopkins APL Technical Digest, vol. 8, no. 2, 1987.

J. Geophys. Res., vol. 84, no. B8, 1979.

J. Geophys. Res., vol. 87, no. C5, 1982.

J. Geophys. Res., vol. 88, no. C3, 1983.

Kenney, J. E., E. A. Uliana, and E. J. Walsh, "The surface contour radar, a unique remote sensing instrument," IEEE Trans. Microwave Theory and Techniques, vol. MTT-27, no. 12, pp. 1080-1092, 1979.

Lee, H. S., and C. L. Parsons, "Mesoscale ocean eddy measurements by multibeam altimetry," J. Geophys. Res., vol. 91, no. C8, pp. 9693-9699, 1986.

Leitao, C. D., N. E. Huang, and C. G. Parra, Final Report of GEOS-3 Ocean Current Investigation Using Radar Altimeter Profiling, NASA TM 73280, 31 pp., 1978.

Martin, T. V., H. J. Zwally, A. C. Brenner, and R. A. Bindshadler, "Analysis and retracking of continental ice sheet radar altimeter waveforms," J. Geophys. Res., vol. 88, p. 1608, 1983.

McArthur, J. L., G. B. Bush, and C. C. Kilgus, "Multibeam altimeter definition study," a proposal to NASA for Applications Notice dated April 19, 1978, from The Johns Hopkins University Applied Physics Laboratory, July 1978.

McGoogan, J. T., C. D. Leita, W. T. Wells, L. S. Miller, and G. S. Brown, "SKYLAB altimeter applications and scientific results," Progress in Astronautics and Aeronautics, vol. 48, pp. 299-326, 1976.

McGoogan, J. T., C. L. Purdy, L. C. Rossi, E. J. Walsh, H. R. Stanley, and D. W. Hancock, Advanced Ocean Sensor Long Range Plan, Wallops Internal Publ. WFC-971.0-82-004, 103 pp., 1982.

McGoogan, J. T., and E. J. Walsh, "Real-time determination of geophysical parameters from a multibeam altimeter," Remote Sensing of Earth from Space: Role of "Smart Sensors", Roger A. Breckenridge, ed., vol. 67 of Progress in Astronautics and Aeronautics, pp. 110-133, 1978.

Miller, L. S., Investigation of the Applications of GEOS-3 Radar Altimeter Data in Remote Sensing of Land and Sea Features, NASA CR-141428, 93 pp., 1977.

Miller, L. S., and D. L. Hammond, "Objectives and capabilities of the SKYLAB S-193 altimeter experiment," IEEE Trans. Geoscience Electronics, vol. GE-10, no. 1, pp. 73-79, 1972.

Miller, L. S., and G. S. Hayne, "Characteristics of ocean-reflected short radar pulses with applications to altimetry and surface roughness determination," in Sea Surface Topography from Space, edited by J. R. Apel, NOAA TR ERL 228-AOML7, p. 12-1, U. S. Government Printing Office, 1972.

Mooers, C. N. K., D. E. Barrick, R. C. Cheney, D. B. Lame, and J. G. Marsh, "The potential of satellite-based radar altimeters," EOS, vol. 65, no. 10, pp. 81-83, 1984.

Munk, W., "Variable ocean structure," Advances in Oceanography, Plenum Press, New York, pp. 209-211, 1978.

Ousbourne, J. J., "Detectability of oceanographic features using satellite altimeters," APL Internal Memo STD-R-658, 1982.

Papoulis, A., Probability, Random Variables, and Stochastic Processes, McGraw-Hill Book Company, New York, 1965.

Parsons, C. L., and L. S. Miller, "Design of a large-aperture lens antenna usable over a +/- 15 scanning sector," IEEE Trans. Antennas and Propagation, vol. 36, no. 8, pp. 1162-1165, 1988.

Parsons, C. L., and E. J. Walsh, "Off-nadir radar altimetry," IEEE Trans. Geoscience and Remote Sensing, vol. 27, no. 2, pp. 215-224, 1989.

Pierson, W. J., and E. Mehr, "The effects of wind waves and swell on the ranging accuracy of a radar altimeter," report on contract no. N62306-70-A-0075, New York University, School of Engineering and Science, 1970.

Skolnik, M. I., Radar Handbook, McGraw-Hill, New York, 1970.

TOPEX Science Working Group, Satellite Altimetric Measurements of the Ocean, NASA, 78 pp., 1981.

Topographic Science Working Group, Topographic Science Working Group Report to the Land Processes Branch, Earth Science and Applications Division, NASA Headquarters, NASA, 64 pp., 1988.

Townsend, W. F., "An initial assessment of the performance achieved by the SEASAT-1 radar altimeter," IEEE J. Oceanic Eng., vol. OE-5, p. 82, 1980.

Walsh, E. J., "Analysis of experimental NRL radar altimeter data," Radio Science, vol. 9, nos. 8,9, pp. 711-722, 1974.

Walsh, E. J., D. W. Hancock III, D. E. Hines, R. N. Swift, and J. F. Scott, "Evolution of the directional wave spectrum from shoreline to fully developed," submitted for publication to J. Physical Oceanography, 1987.

Zwally, H. J., R. A. Bindschadler, A. C. Brenner, T. V. Martin, and R. H. Thomas, "Surface elevation contours of Greenland and Antarctic ice sheets," J. Geophys. Res., vol. 88, p. 1589, 1983.

## APPENDIX A

### INTERFEROMETRIC LOBE PATTERN EQUATION DERIVATION

Following the development in Born and Wolf (1964, pp. 256-259), it can be shown that the intensity pattern resulting from the interference of two monochromatic coherent radiation sources is given by

$$I = I_1 + I_2 + 2\sqrt{I_1 I_2} \cos \delta \quad (\text{A.1})$$

where  $\delta$  is the phase difference between the two radiant beams. This quantity is related to the difference in distance traveled by the two beams,  $\Delta R$ , by

$$\delta = k \Delta R \quad (\text{A.2})$$

where  $k$  is the electromagnetic wavenumber.

Electromagnetic intensity is defined as power per unit area, or power density. The power density in each beam striking the surface was derived in (32), Where the  $G$  terms represent now the beam antenna patterns. Equation (A.1) now becomes

$$I = \frac{P_t}{4\pi} \left( \frac{G_1}{R_1^2} + \frac{G_2}{R_2^2} + \frac{2}{R_1 R_2} \sqrt{G_1 G_2} \cos k \Delta R \right) \quad (\text{A.3})$$

The received power back at one of the antennas was found in (38) to be

$$P = I * \sigma * A / (4\pi R)^2 \quad (\text{A.4})$$

where  $A$  is the antenna aperture and  $R$  is the distance from the surface to the receiving aperture, assumed to be antenna 1 in this development. For a paraboloidal receiver and using (39) we find that

$$P = \frac{P_t \sigma}{(4\pi)^3} * \frac{G_1^2}{R^2} * \left( \frac{G_1}{R_1^2} + \frac{G_2}{R_2^2} + \frac{2}{R_1 R_2} \sqrt{G_1 G_2} \cos k \Delta R \right) \quad (\text{A.5})$$

Separating out the maximum antenna gain  $G_o$  from the directional characteristics of each antenna beam, it can be shown that

$$P = \frac{P_t \sigma}{(4\pi)^3} * \frac{G_1^2}{R^2} * G_o \left( \frac{\tilde{G}_1}{R_1^2} + \frac{\tilde{G}_2}{R_2^2} + \frac{2}{R_1 R_2} \sqrt{\tilde{G}_1 \tilde{G}_2} \cos k \Delta R \right) \quad (\text{A.6})$$

On a per unit area basis, the radiant intensity can now be found to be

$$I = \frac{P_t \sigma_o}{(4\pi)^3} \frac{G_1 G_o \lambda^2}{R^2} \left( \frac{\tilde{G}_1}{R_1^2} + \frac{\tilde{G}_2}{R_2^2} + \frac{2}{R_1 R_2} \sqrt{\tilde{G}_1 \tilde{G}_2} \cos k \Delta R \right) \quad (\text{A.7})$$

APPENDIX B  
PUBLISHED 36 GHz BACKSCATTERING CROSS-SECTION DATA

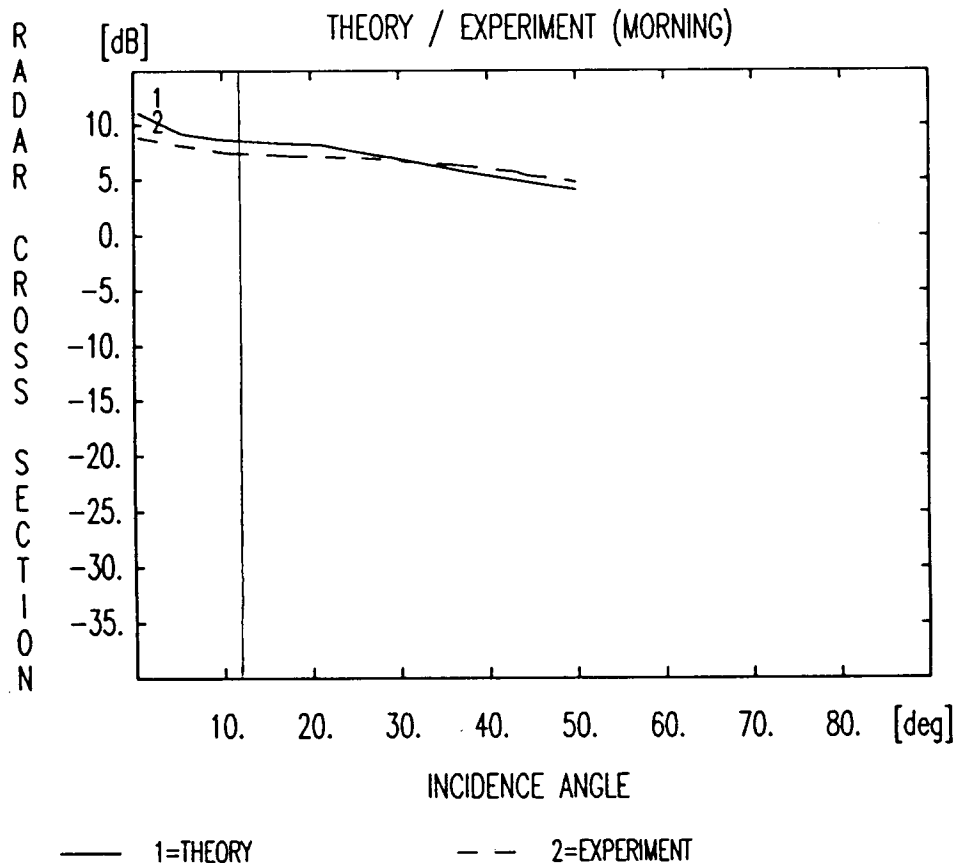
PRECEDING PAGE BLANK NOT FILMED

Author names ZUNIGA M.A., T.M. HABASHY AND J.A. KONG  
 Title "ACTIVE REMOTE SENSING OF LAYERED RANDOM MEDIA"  
 Publication IEEE TRANS. GEOSCI. ELEC., GE-17(4), OCT. 1979, PP.296-302

Frequency band Ka File name AB0067.RCS  
 Polarization HH Author code [1979. 4]  
 Terrain codes 8.

**SNOW FIELD (27 CM DEEP)**

35.6 GHZ, HH



MICROWAVE REMOTE SENSING LABORATORY - UNIVERSITY OF MASSACHUSETTS

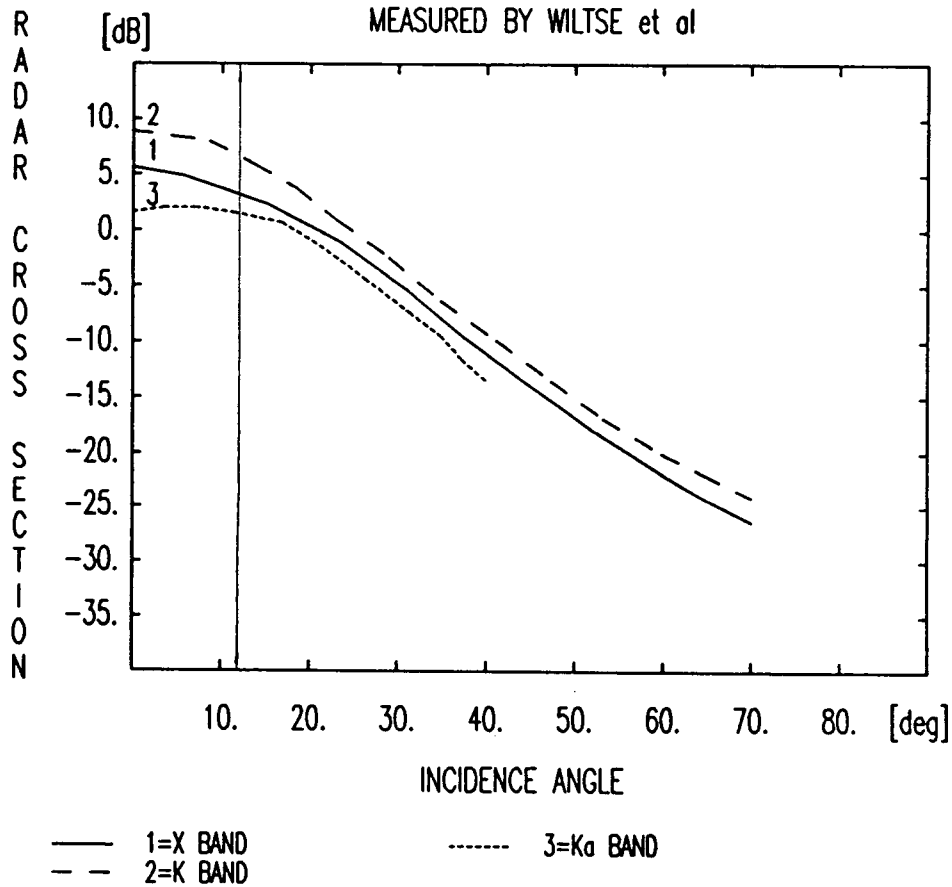
Author names COSGRIFF R.L., W.H. PEAKE AND R.C. TAYLOR  
Title TERRAIN SCATTERING PROPERTIES FOR SENSOR SYSTEM DESIGN (TERRAIN HANDBOOK II)  
Publication ENGG. EXPT. STN. BULL. 181, THE OHIO STATE UNIV., COLUMBUS, OHIO, MAY 1960

Frequency band X K Ka File name AB0231.RCS  
Polarization HH Author code [1960. 4]  
Terrain codes 2.3.

### SEA RETURN

X, K, Ka BAND, HH, 0-70 DEG

MEASURED BY WILTSE et al



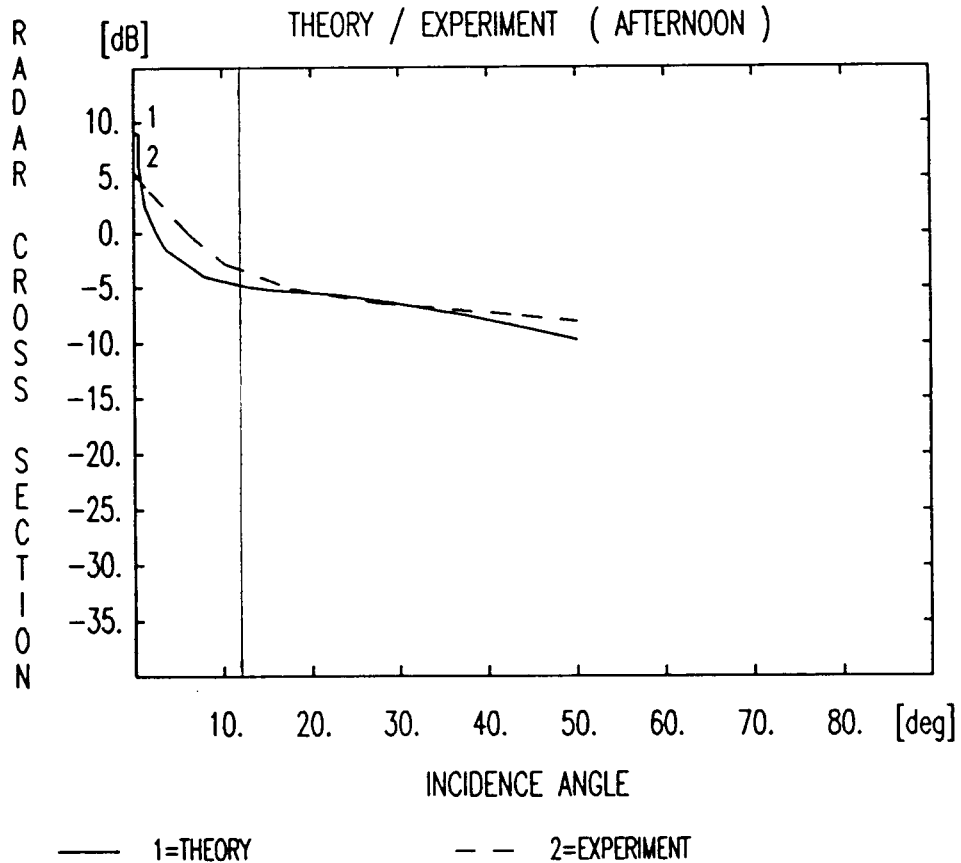
MICROWAVE REMOTE SENSING LABORATORY - UNIVERSITY OF MASSACHUSETTS

Author names ZUNIGA M.A., T.M. HABASHY AND J.A. KONG  
 Title "ACTIVE REMOTE SENSING OF LAYERED RANDOM MEDIA"  
 Publication IEEE TRANS. GEOSCI. ELEC., GE-17(4), OCT. 1979, PP.296-302

Frequency band Ka File name AB0101.RCS  
 Polarization HH Author code [1979. 4]  
 Terrain codes 8.

**SNOW FIELD (27 CM DEEP)**

35.6 GHZ, HH



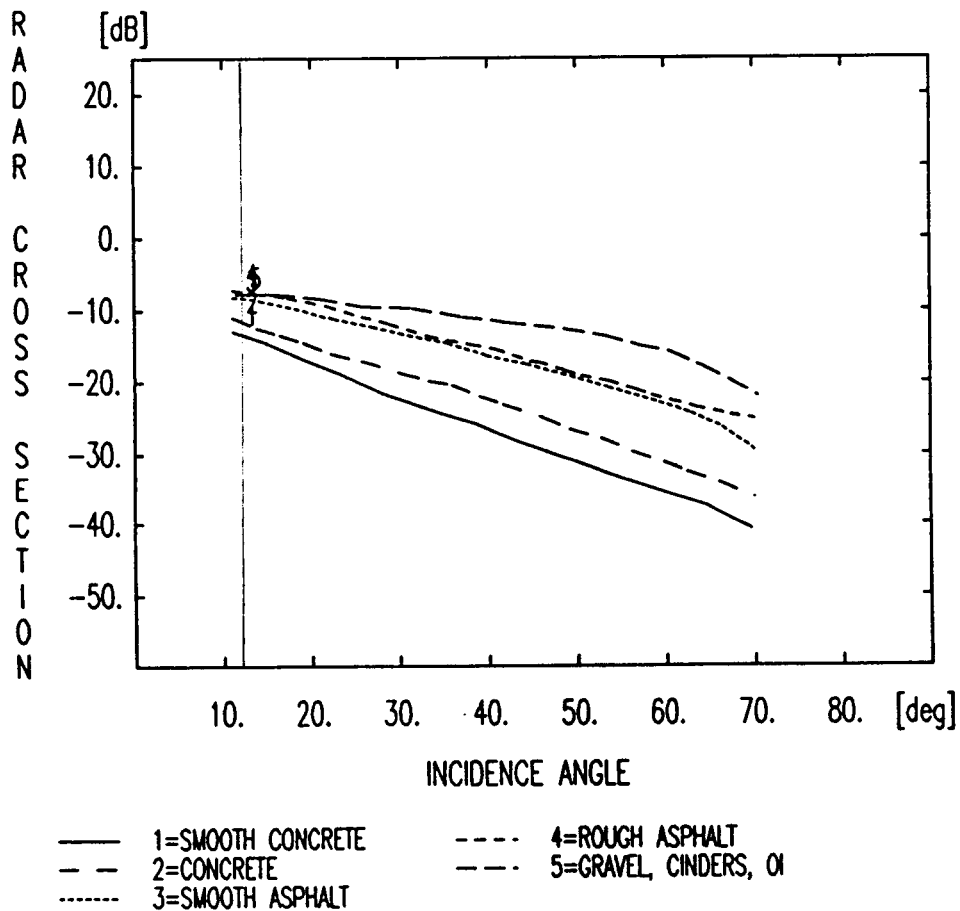
MICROWAVE REMOTE SENSING LABORATORY - UNIVERSITY OF MASSACHUSETTS

Author names COSGRIFF R.L., W.H. PEAKE AND R.C. TAYLOR  
 Title TERRAIN SCATTERING PROPERTIES FOR SENSOR SYSTEM DESIGN (TERRAIN HANDBOOK II)  
 Publication ENGG. EXPT. STN. BULL. 181, THE OHIO STATE UNIV., COLUMBUS, OHIO, MAY 1960

Frequency band Ka File name AB0148.RCS  
 Polarization HH Author code [1960. 4]  
 Terrain codes 5.1.2. + 5.1. + 5.2.3. + 5.2.4. + 5.3.1.

### SMOOTH SURFACES

35 GHZ, HH, 20-80 DEG



MICROWAVE REMOTE SENSING LABORATORY - UNIVERSITY OF MASSACHUSETTS

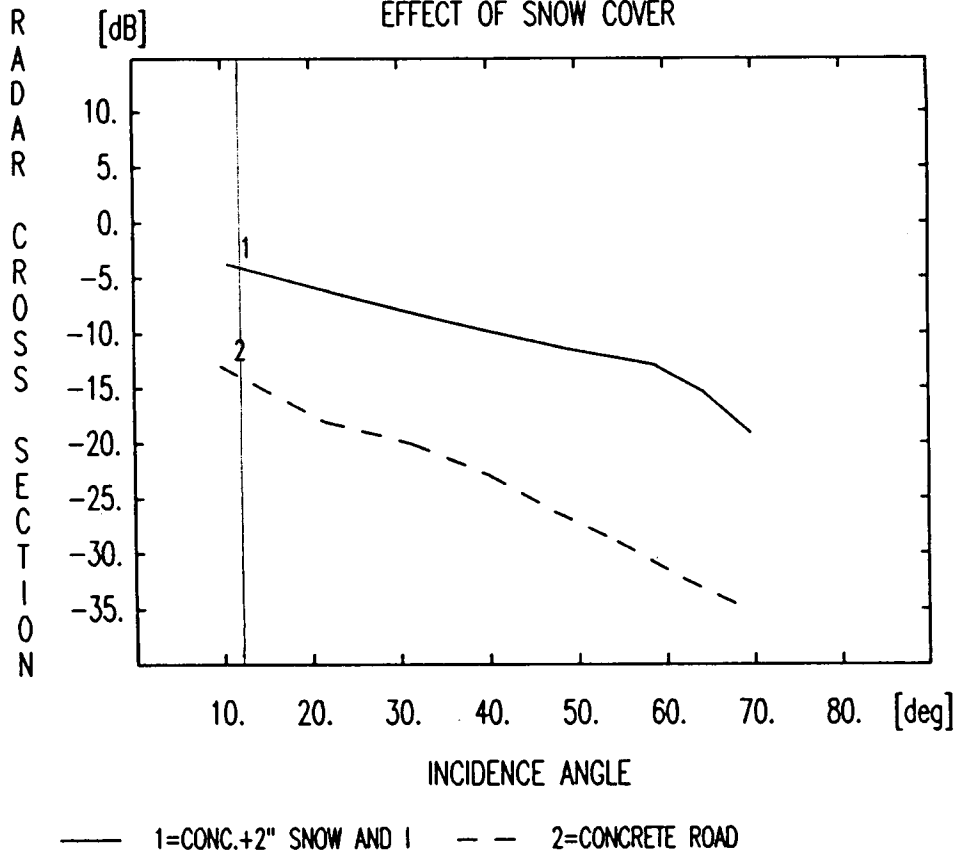
Author names COSGRIFF R.L., W.H. PEAKE AND R.C. TAYLOR  
 Title TERRAIN SCATTERING PROPERTIES FOR SENSOR SYSTEM DESIGN (TERRAIN HANDBOOK II)  
 Publication ENGG. EXPT. STN. BULL. 181, THE OHIO STATE UNIV., COLUMBUS, OHIO, MAY 1960

Frequency band Ka File name AB0179.RCS  
 Polarization HH Author code [1960. 4]  
 Terrain codes 8.5. + 5.1.1.

**CONCRETE WITH SNOW (2") AND ICE**

35 GHZ, HH, 10-70 DEG

EFFECT OF SNOW COVER



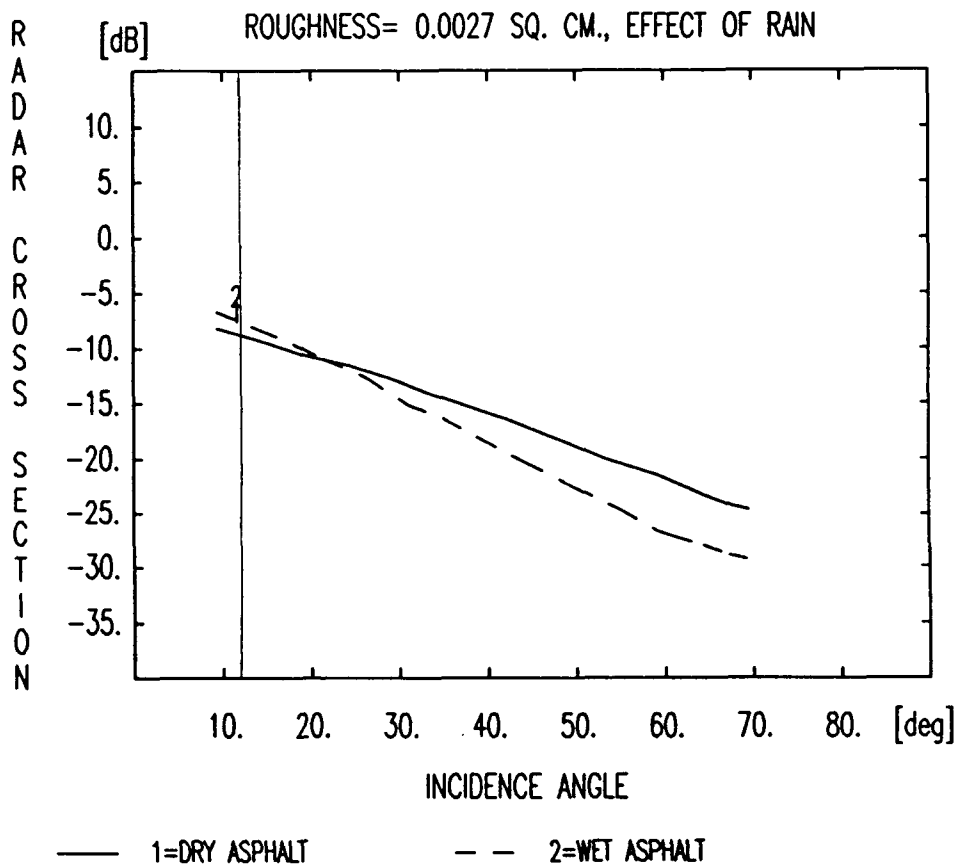
MICROWAVE REMOTE SENSING LABORATORY - UNIVERSITY OF MASSACHUSETTS

Author names COSGRIFF R.L., W.H. PEAKE AND R.C. TAYLOR  
Title TERRAIN SCATTERING PROPERTIES FOR SENSOR SYSTEM DESIGN (TERRAIN HANDBOOK II)  
Publication ENGG. EXPT. STN. BULL. 181, THE OHIO STATE UNIV., COLUMBUS, OHIO, MAY 1960

Frequency band Ka File name AB0203.RCS  
Polarization HH Author code [1960. 4]  
Terrain codes 5.2.3.

### ASPHALT ROAD (ROUGH)

35 GHZ, HH, 10-70 DEG



MICROWAVE REMOTE SENSING LABORATORY - UNIVERSITY OF MASSACHUSETTS

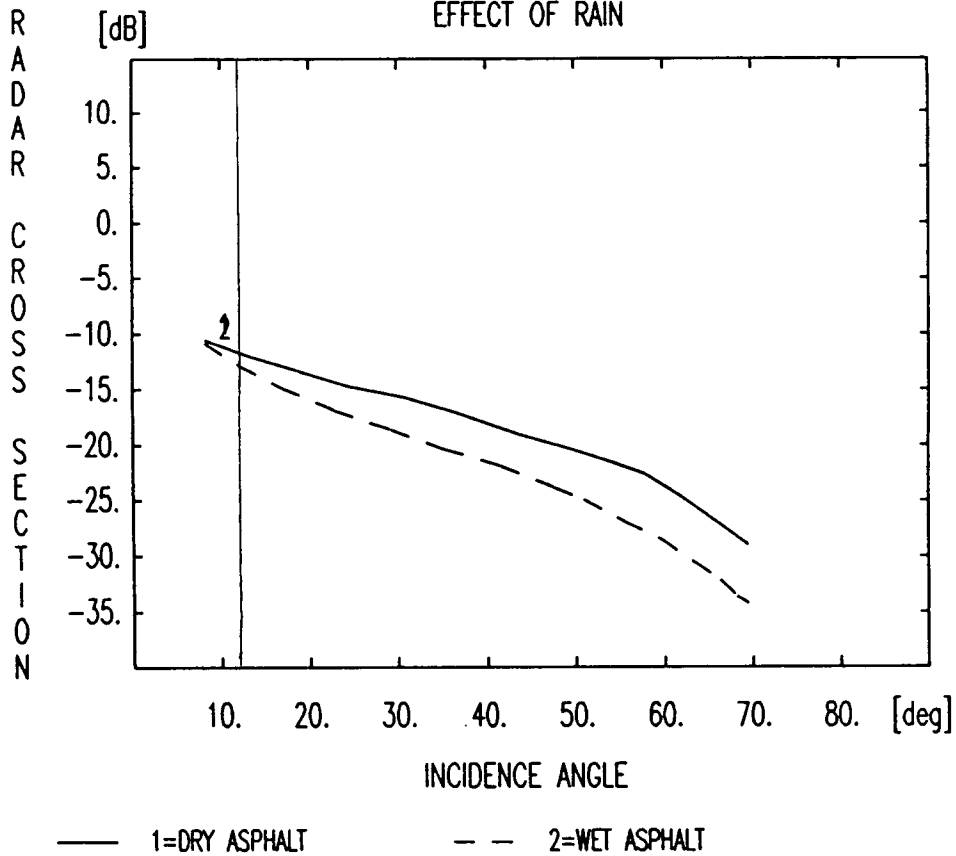
Author names COSGRIFF R.L., W.H. PEAKE AND R.C. TAYLOR  
 Title TERRAIN SCATTERING PROPERTIES FOR SENSOR SYSTEM DESIGN (TERRAIN HANDBOOK II)  
 Publication ENGG. EXPT. STN. BULL. 181, THE OHIO STATE UNIV., COLUMBUS, OHIO, MAY 1960

Frequency band Ka File name AB0202.RCS  
 Polarization HH Author code [1960. 4]  
 Terrain codes 5.2.4.

**ASPHALT ROAD (SMOOTH)**

35 GHZ, HH, 10-70 DEG

EFFECT OF RAIN



MICROWAVE REMOTE SENSING LABORATORY - UNIVERSITY OF MASSACHUSETTS

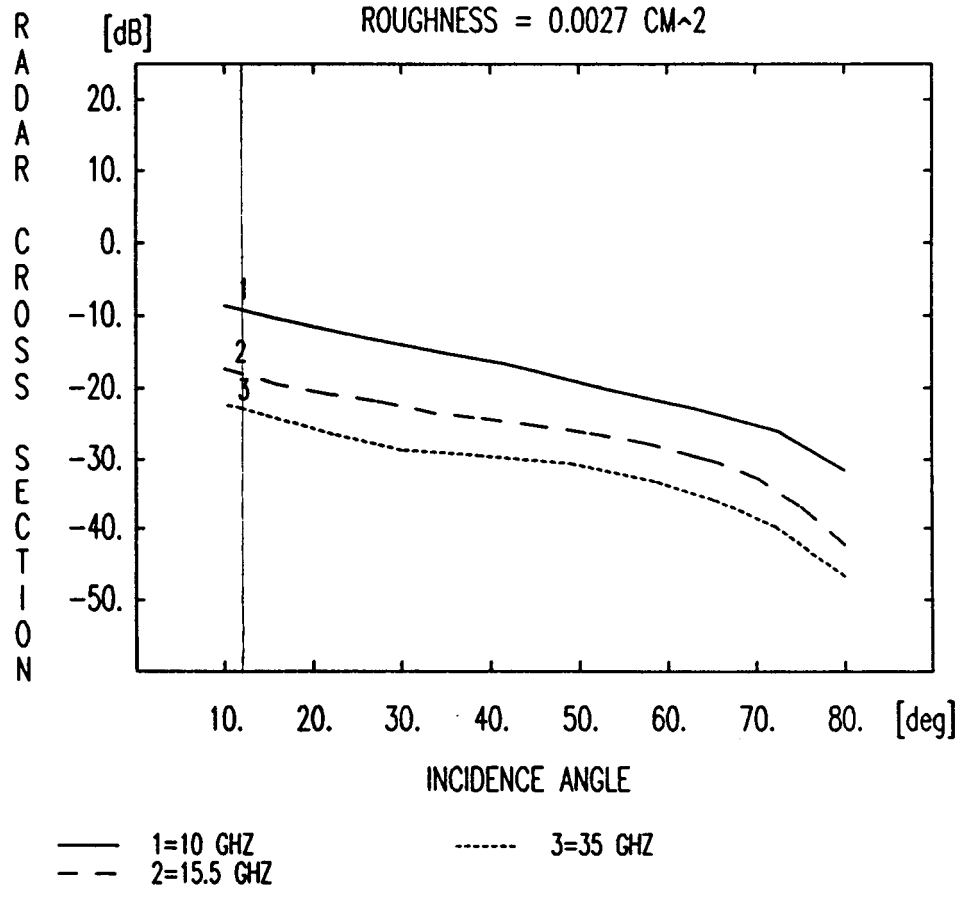
Author names COSGRIFF R.L., W.H. PEAKE AND R.C. TAYLOR  
 Title TERRAIN SCATTERING PROPERTIES FOR SENSOR SYSTEM DESIGN (TERRAIN HANDBOOK II)  
 Publication ENGG. EXPT. STN. BULL. 181, THE OHIO STATE UNIV., COLUMBUS, OHIO, MAY 1960

Frequency band X Ku Ka File name AB0124.RCS  
 Polarization HH Author code [1960. 4]  
 Terrain codes 5.2.3.

**ASPHALT ROAD (ROUGH)**

10, 15.5, 35 GHZ, HH, 10-80 DEG

ROUGHNESS = 0.0027 CM<sup>2</sup>



MICROWAVE REMOTE SENSING LABORATORY - UNIVERSITY OF MASSACHUSETTS

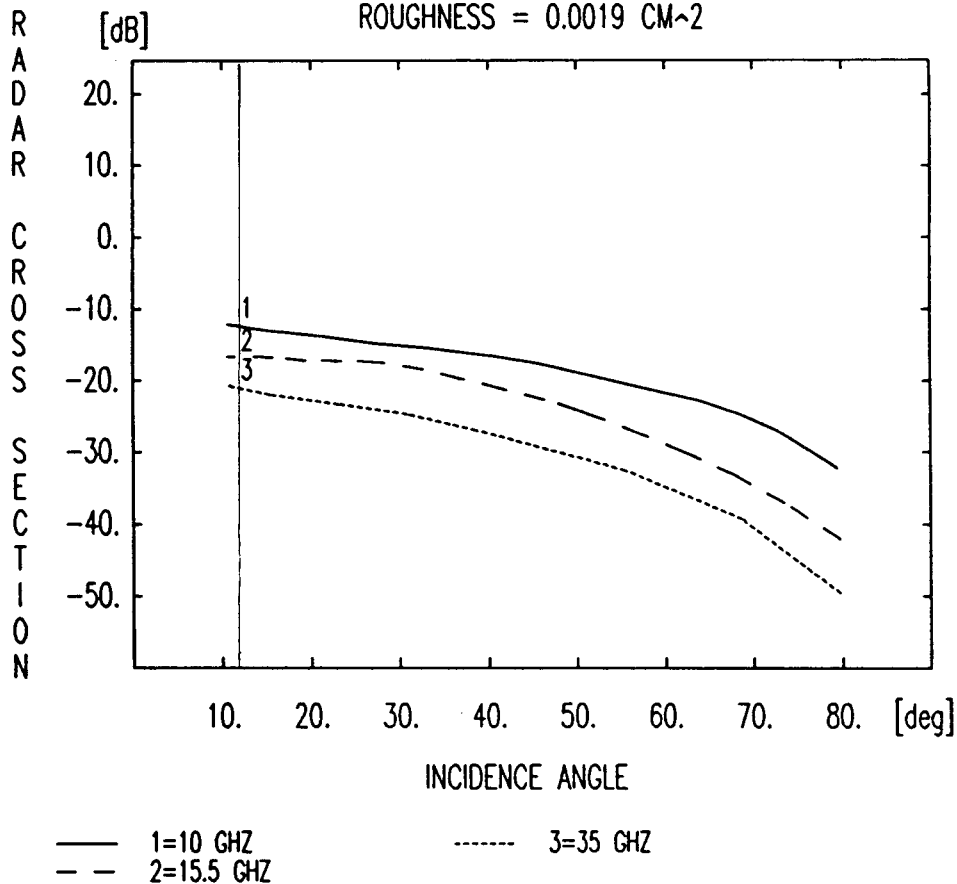
Author names COSGRIFF R.L., W.H. PEAKE AND R.C. TAYLOR  
 Title TERRAIN SCATTERING PROPERTIES FOR SENSOR SYSTEM DESIGN (TERRAIN HANDBOOK II)  
 Publication ENGG. EXPT. STN. BULL. 181, THE OHIO STATE UNIV., COLUMBUS, OHIO, MAY 1960

Frequency band X Ku Ka File name AB0126.RCS  
 Polarization HH Author code [1960. 4]  
 Terrain codes 5.2.3.

**ASPHALT ROAD (MEDIUM ROUGH)**

10, 15.5, 35 GHZ, HH, 10-80 DEG

ROUGHNESS = 0.0019 CM<sup>2</sup>



MICROWAVE REMOTE SENSING LABORATORY - UNIVERSITY OF MASSACHUSETTS

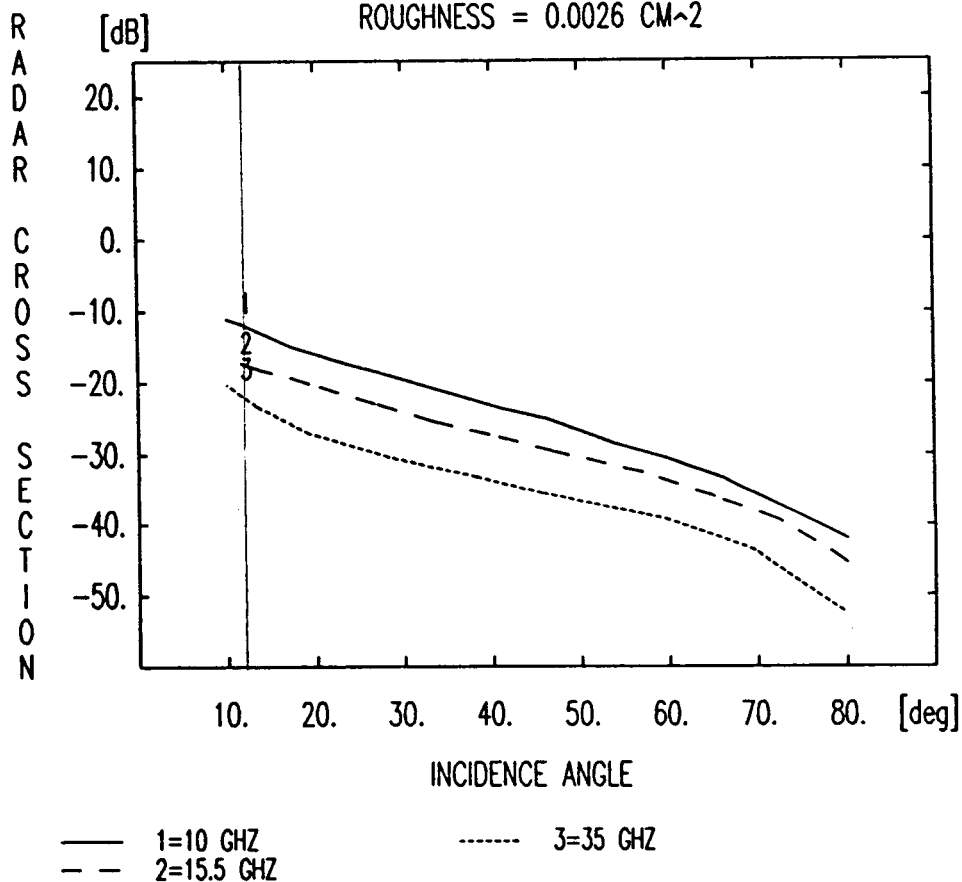
Author names COSGRIFF R.L., W.H. PEAKE AND R.C. TAYLOR  
 Title TERRAIN SCATTERING PROPERTIES FOR SENSOR SYSTEM DESIGN (TERRAIN HANDBOOK II)  
 Publication ENGG. EXPT. STN. BULL. 181, THE OHIO STATE UNIV., COLUMBUS, OHIO, MAY 1960

Frequency band X Ku Ka File name AB0134.RCS  
 Polarization HH Author code [1960. 4]  
 Terrain codes 5.1.1.

**CONCRETE ROAD (MEDIUM ROUGH)**

10, 15.5, 35 GHZ, HH, 10-80 DEG

ROUGHNESS = 0.0026 CM<sup>2</sup>



MICROWAVE REMOTE SENSING LABORATORY - UNIVERSITY OF MASSACHUSETTS

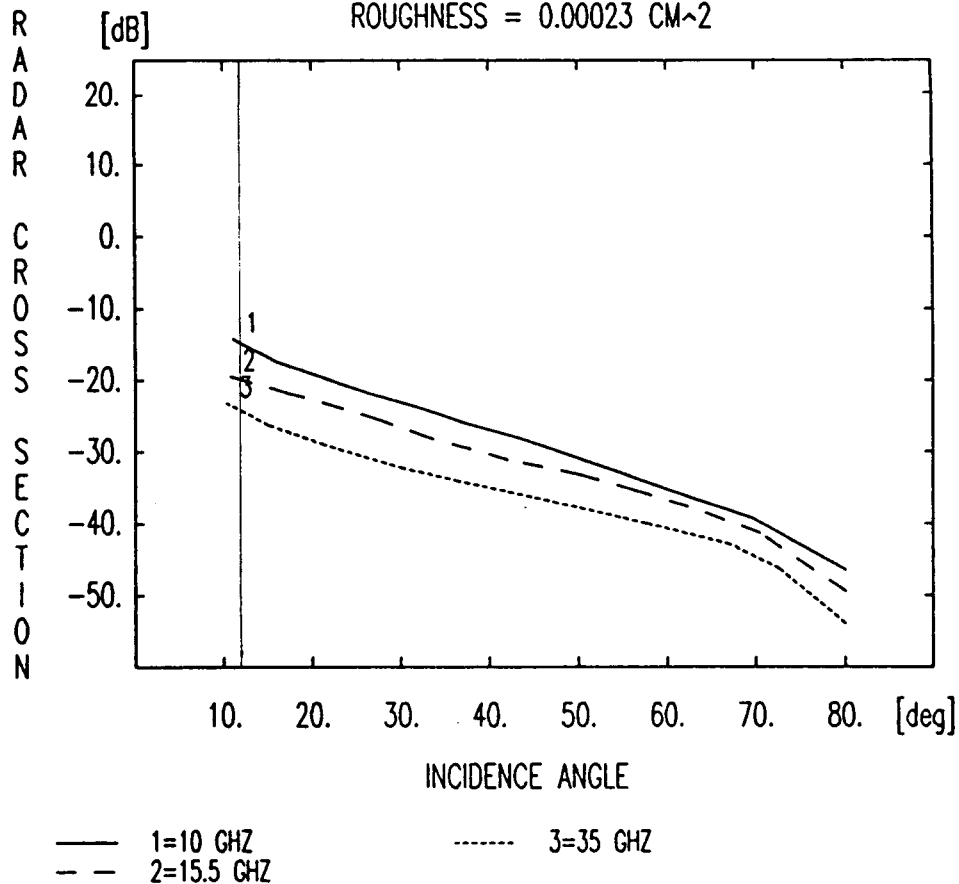
Author names COSGRIFF R.L., W.H. PEAKE AND R.C. TAYLOR  
Title TERRAIN SCATTERING PROPERTIES FOR SENSOR SYSTEM DESIGN (TERRAIN HANDBOOK II)  
Publication ENGG. EXPT. STN. BULL. 181, THE OHIO STATE UNIV., COLUMBUS, OHIO, MAY 1960

Frequency band X Ku Ka File name AB0136.RCS  
Polarization HH Author code [1960. 4]  
Terrain codes 5.1.2.

### CONCRETE ROAD (SMOOTH)

10, 15.5, 35 GHZ, HH, 10-80 DEG

ROUGHNESS = 0.00023 CM<sup>2</sup>

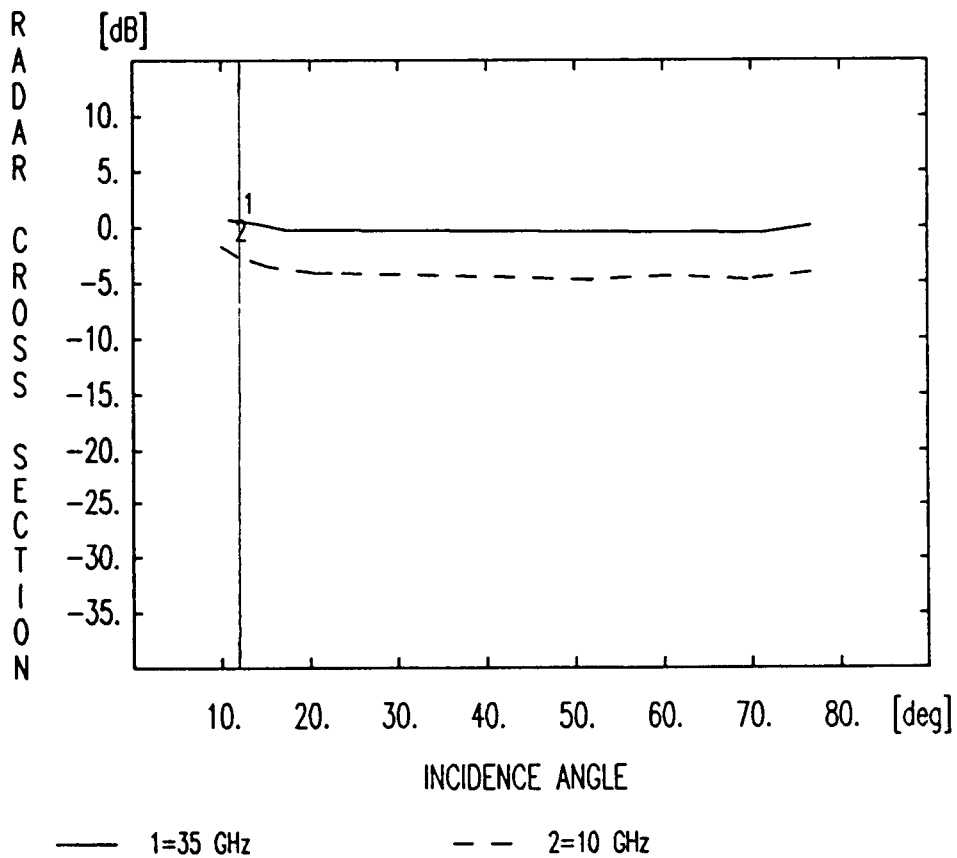


MICROWAVE REMOTE SENSING LABORATORY - UNIVERSITY OF MASSACHUSETTS

Author names DE LOOR G.P.,P.HOOGBOOM AND E.P.W.ATTEMA  
 Title "THE DUTCH ROVE PROGRAM"  
 Publication IEEE TRANS. GEOSCI. REM. SENS., GE-20(1), JAN. 1982, PP.3-10  
 Frequency band X Ka File name AB0018.RCS  
 Polarization HH Author code [1982. 1]  
 Terrain codes 6.3.20.

PEAS

35 GHz AND 10 GHz, HH



MICROWAVE REMOTE SENSING LABORATORY - UNIVERSITY OF MASSACHUSETTS

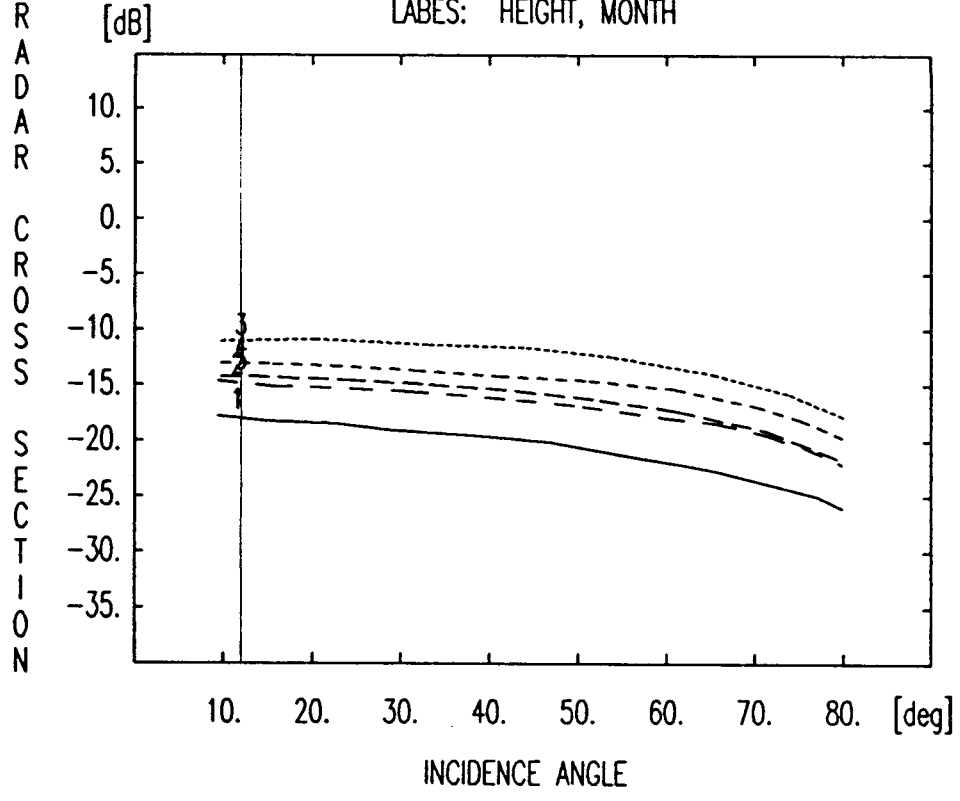
Author names COSGRIFF R.L., W.H. PEAKE AND R.C. TAYLOR  
 Title TERRAIN SCATTERING PROPERTIES FOR SENSOR SYSTEM DESIGN (TERRAIN HANDBOOK II)  
 Publication ENGG. EXPT. STN. BULL. 181, THE OHIO STATE UNIV., COLUMBUS, OHIO, MAY 1960

Frequency band Ka File name AB0213.RCS  
 Polarization HH Author code [1960. 4]  
 Terrain codes 6.3.19.

**GRASS (SEASONAL CHANGES)**

35 GHZ, HH, 10-80 DEG

LABES: HEIGHT, MONTH



— 1=1" MARCH                      -.-.- 4=2.75" SEPT.  
 - - 2=1" APRIL                     -.-.- 5=2" NOV.  
 ..... 3=1" MAY

MICROWAVE REMOTE SENSING LABORATORY - UNIVERSITY OF MASSACHUSETTS

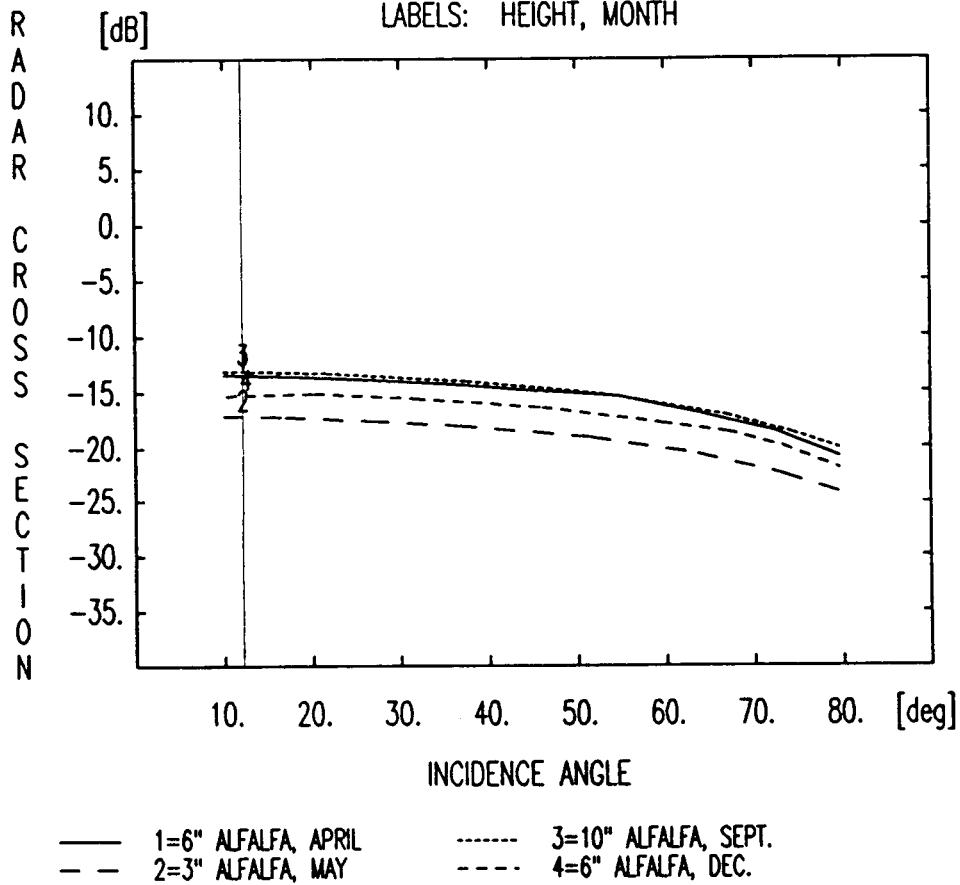
Author names COSGRIFF R.L., W.H. PEAKE AND R.C. TAYLOR  
 Title TERRAIN SCATTERING PROPERTIES FOR SENSOR SYSTEM DESIGN (TERRAIN HANDBOOK II)  
 Publication ENGG. EXPT. STN. BULL. 181, THE OHIO STATE UNIV., COLUMBUS, OHIO, MAY 1960

Frequency band Ka File name AB0215.RCS  
 Polarization HH Author code [1960. 4]  
 Terrain codes 6.3.14.

**ALFALFA (SEASONAL CHANGES)**

35 GHZ, HH, 10-80 DEG

LABELS: HEIGHT, MONTH



MICROWAVE REMOTE SENSING LABORATORY - UNIVERSITY OF MASSACHUSETTS

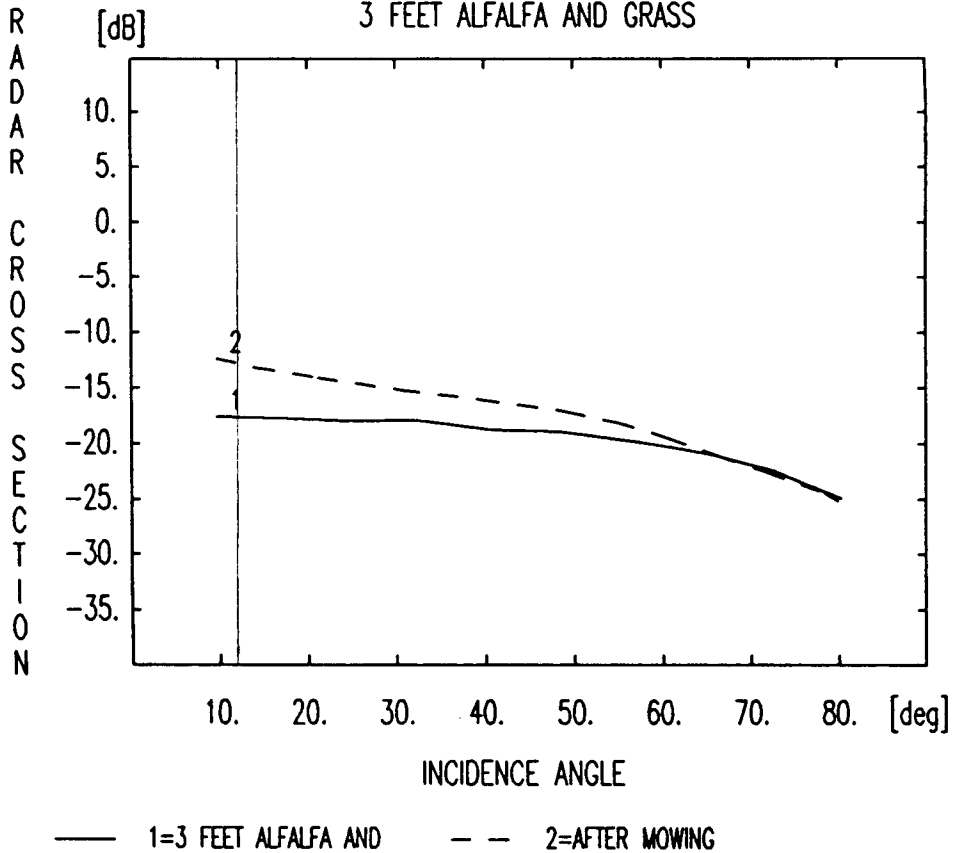
Author names COSGRIFF R.L., W.H. PEAKE AND R.C. TAYLOR  
 Title TERRAIN SCATTERING PROPERTIES FOR SENSOR SYSTEM DESIGN (TERRAIN HANDBOOK II)  
 Publication ENGG. EXPT. STN. BULL. 181, THE OHIO STATE UNIV., COLUMBUS, OHIO, MAY 1960

Frequency band Ka File name AB0221.RCS  
 Polarization HH Author code [1960. 4]  
 Terrain codes 6.3.14.

**EFFECTS OF MOWING ALFALFA**

35 GHZ, HH, 10-80 DEG

3 FEET ALFALFA AND GRASS

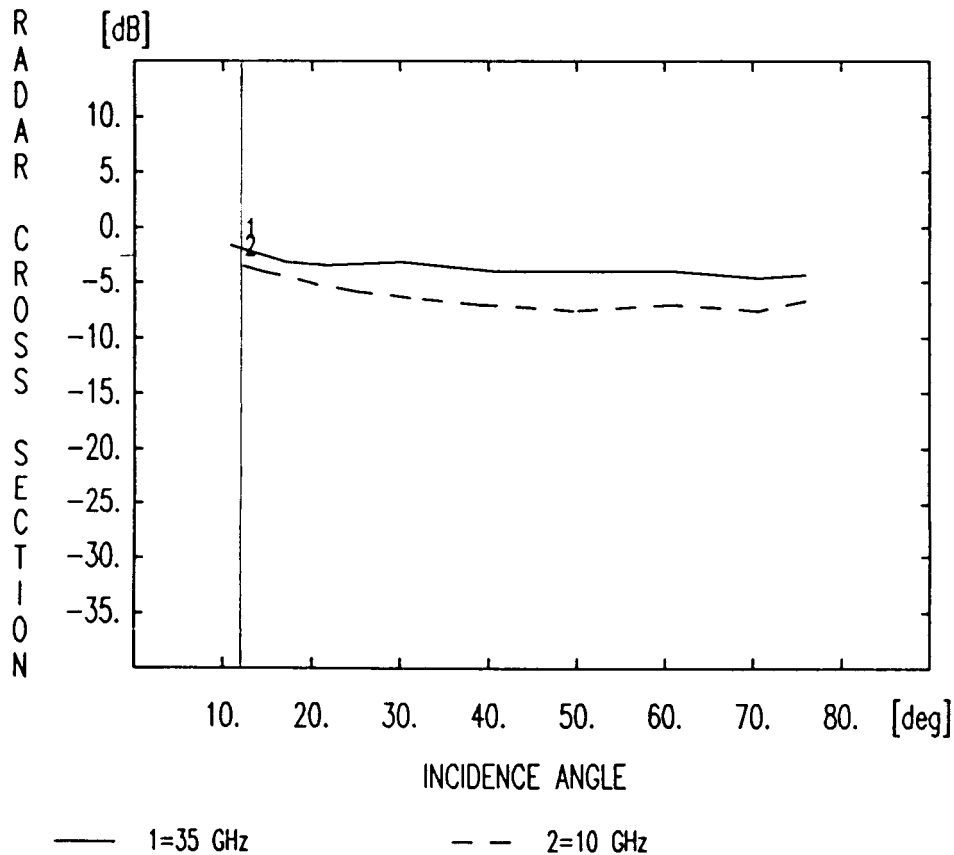


MICROWAVE REMOTE SENSING LABORATORY - UNIVERSITY OF MASSACHUSETTS

Author names DE LOOR G.P.,P.HOOGBOOM AND E.P.W.ATTEMA  
 Title "THE DUTCH ROVE PROGRAM"  
 Publication IEEE TRANS. GEOSCI. REM. SENS., GE-20(1), JAN. 1982, PP.3-10  
 Frequency band X Ka File name AB0017.RCS  
 Polarization HH Author code [1982. 1]  
 Terrain codes 6.3.19.

**GRASS**

35 GHz AND 10 GHz, HH



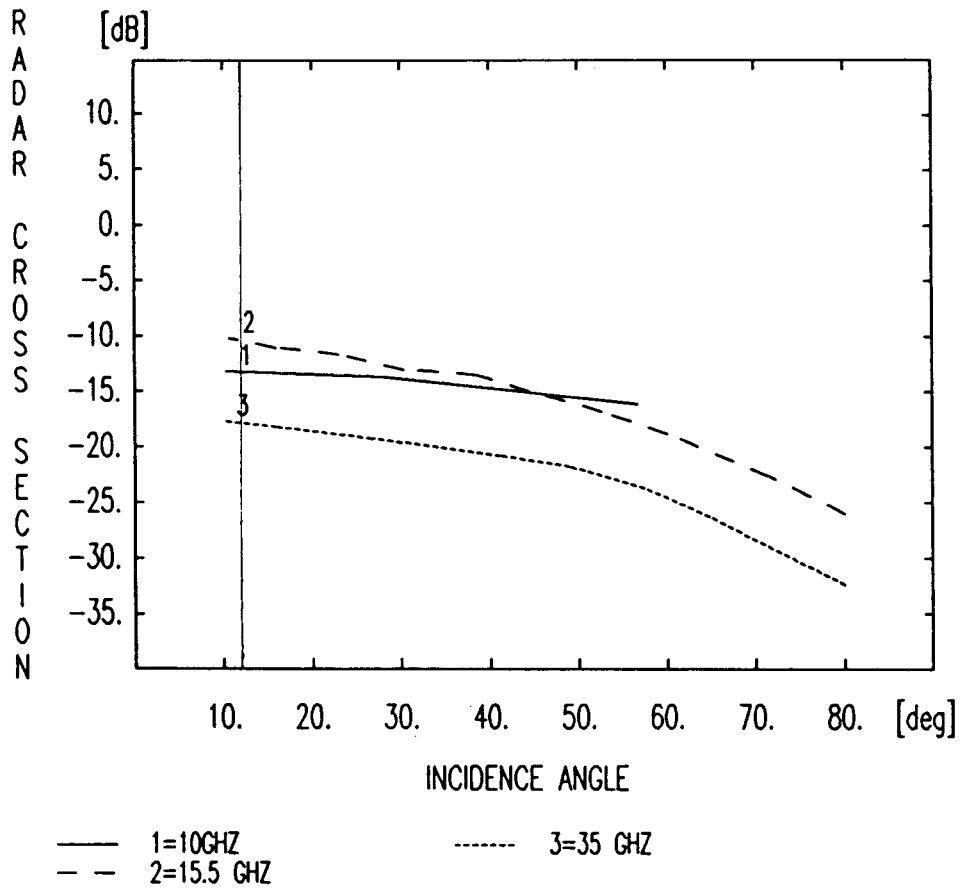
MICROWAVE REMOTE SENSING LABORATORY - UNIVERSITY OF MASSACHUSETTS

Author names COSGRIFF R.L., W.H. PEAKE AND R.C. TAYLOR  
 Title TERRAIN SCATTERING PROPERTIES FOR SENSOR SYSTEM DESIGN (TERRAIN HANDBOOK II)  
 Publication ENGG. EXPT. STN. BULL. 181, THE OHIO STATE UNIV., COLUMBUS, OHIO, MAY 1960

Frequency band X Ku Ka File name AB0140.RCS  
 Polarization HH Author code [1960. 4]  
 Terrain codes 12.1.

**DISKED GROUND**

10, 15.5, 35 GHZ, HH, 10-80 DEG



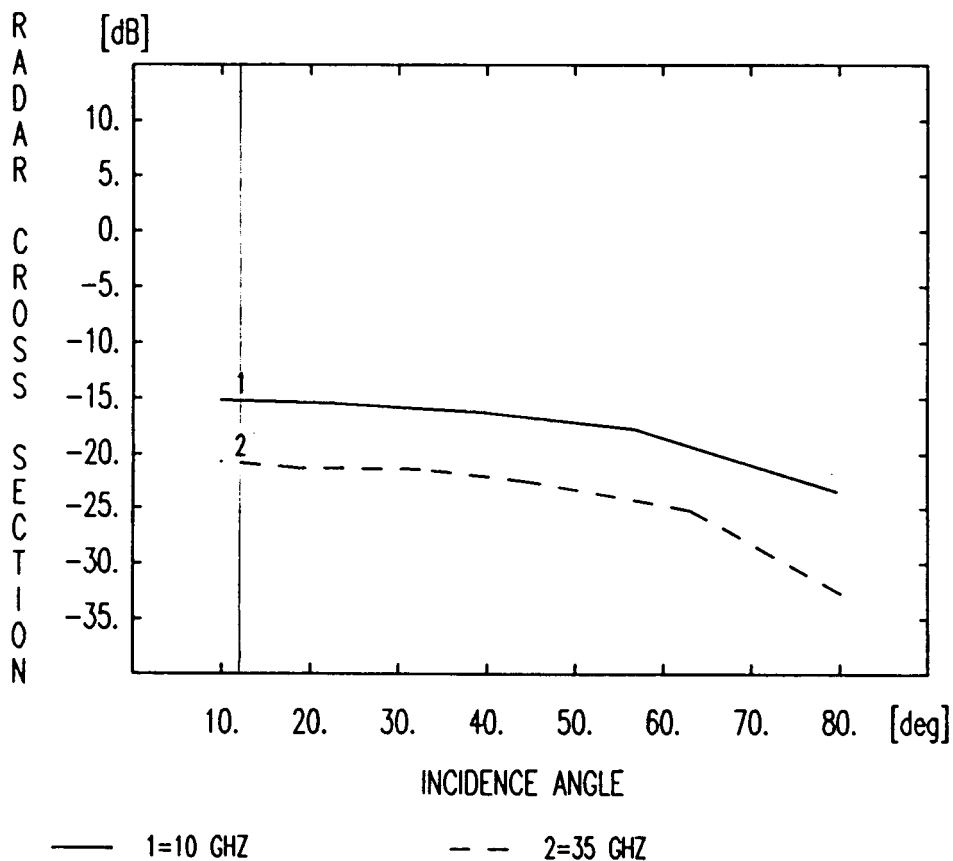
MICROWAVE REMOTE SENSING LABORATORY - UNIVERSITY OF MASSACHUSETTS

Author names COSGRIFF R.L., W.H. PEAKE AND R.C. TAYLOR  
Title TERRAIN SCATTERING PROPERTIES FOR SENSOR SYSTEM DESIGN (TERRAIN HANDBOOK II)  
Publication ENGG. EXPT. STN. BULL. 181, THE OHIO STATE UNIV., COLUMBUS, OHIO, MAY 1960

Frequency band X Ka File name AB0144.RCS  
Polarization HH Author code [1960. 4]  
Terrain codes 12.2.

**PLOWED FIELD**

10, 35 GHZ, HH, 10-80 DEG



MICROWAVE REMOTE SENSING LABORATORY - UNIVERSITY OF MASSACHUSETTS



## Report Documentation Page

1. Report No. NASA RP-1226		2. Government Accession No.		3. Recipient's Catalog No.	
4. Title and Subtitle MARA System Documentation Volume I - MARA System Requirements Document				5. Report Date July 1989	
				6. Performing Organization Code 672	
7. Author(s) C. L. Parsons, Editor				8. Performing Organization Report No. 89-143	
				10. Work Unit No. 161-10-06	
9. Performing Organization Name and Address Goddard Space Flight Center Wallops Flight Facility Wallops Island, VA 23337				11. Contract or Grant No.	
				13. Type of Report and Period Covered Reference Publication	
12. Sponsoring Agency Name and Address National Aeronautics and Space Administration Washington, D.C. 20546-0001				14. Sponsoring Agency Code	
				15. Supplementary Notes	
16. Abstract <p>The MARA System Requirements Document is Volume I of a set of documents that describe the design, construction, and performance of the Multimode Airborne Radar Altimeter (MARA), a flexible airborne radar remote sensing facility developed by NASA's Goddard Space Flight Center. This volume describes the scientific justification for the development of the instrument and the translation of these scientific requirements into instrument design goals. Values for key instrument parameters are derived to accommodate these goals, and simulations and analytical models are used to estimate the developed system's performance.</p>					
17. Key Words (Suggested by Author(s)) remote sensing, radar, sensors microwave sensors, radar altimeters radar tracking			18. Distribution Statement Unclassified - Unlimited  Subject category 35		
19. Security Classif. (of this report) Unclassified		20. Security Classif. (of this page) Unclassified		21. No. of pages 92	22. Price A05